Chapter 2
Wave Propagation Theory

2.1 The Wave Equation

The wave equation in an ideal fluid can be derived from hydrodynamics and the adiabatic relation between pressure and density. The equation for conservation of mass, Euler's equation (Newton's second law), and the adiabatic equation of state are respectively

$$\frac{\partial \rho}{\partial t} = -\nabla \cdot \rho \mathbf{v}, \tag{2.1}$$

$$\frac{\partial \mathbf{v}}{\partial t} + (\mathbf{v} \cdot \nabla)\, \mathbf{v} = -\frac{1}{\rho} \nabla p(\rho), \tag{2.2}$$

$$p = p_0 + \rho' \left[\frac{\partial p}{\partial \rho} \right]_S + \frac{1}{2} (\rho')^2 \left[\frac{\partial^2 p}{\partial \rho^2} \right]_S + \cdots \tag{2.3}$$

and for convenience we define the quantity

$$c^2 \equiv \left[\frac{\partial p}{\partial \rho} \right]_S, \tag{2.4}$$

where c will turn out to be the speed of sound in an ideal fluid. In the above equations, ρ is the density, $\mathbf{v}$ the particle velocity, p the pressure, and the subscript S denotes that the thermodynamic partial derivatives are taken at constant entropy. The ambient quantities of the quiescent (time independent) medium are identified by the subscript 0. We use small perturbations for the pressure and density, $p = p_0 + p'$, $\rho = \rho_0 + \rho'$, and note that $\mathbf{v}$ is also a small quantity; that is, the particle velocity which results from density and pressure perturbations is much smaller than the speed of sound.

F.B. Jensen et al., *Computational Ocean Acoustics*, Modern Acoustics and Signal Processing, DOI 10.1007/978-1-4419-8678-8_2,

2.1.1 The Nonlinear Wave Equation

Retaining higher-order terms in (2.1)–(2.3) yields a nonlinear wave equation. The nonlinear effects we include are contained in the quadratic density term in the equation of state, (2.3), and the quadratic velocity term (the convection term) in Euler's equation, (2.2). First multiply (2.2) by ρ and take its divergence; next, take the partial derivative of (2.1) with respect to time. Substituting one into the other yields

$$\frac{\partial^2 \rho}{\partial t^2} = \nabla^2 p + \partial_i \partial_j (\rho v_i v_j). \tag{2.5}$$

Here, the indices $i, j = 1, 2, 3$ indicate x, y, z-components, respectively. Tensor notation is used; repeated indices signify a summation (e.g., $\partial_i v_i = \nabla \cdot \mathbf{v}$).

The first term on the right-hand side of (2.5) can be rewritten using (2.3) and (2.4) as

$$\nabla^2 p = \nabla^2 c^2 \left[\rho' + \frac{1}{c} \frac{\partial c(\rho_0)}{\partial \rho} (\rho')^2 \right]. \tag{2.6}$$

The convection term on the right-hand side of (2.5) is more difficult to evaluate, but we can obtain an expression for it in the limit of small propagation angles θ with respect to the main direction of propagation, e.g., the x-direction. (This is the same as the paraxial approximation for the parabolic wave equation discussed in Chap. 6.) Then we may estimate v_i using the linear impedance relation – to be later derived as (2.20) – together with the equation of state (2.3),

$$v_i = \frac{\rho' c}{\rho_0} [\delta_{i,x} + O(\theta)] + O(\rho'^2), \tag{2.7}$$

where $\delta_{i,x}$ is the Kronecker delta symbol, so that

$$\partial_i \partial_j (\rho v_i v_j) \simeq \frac{1}{\rho_0} \nabla^2 c^2 (\rho')^2. \tag{2.8}$$

Substituting (2.6) and (2.8) into (2.5), we obtain the nonlinear wave equation

$$\frac{\partial^2 \chi}{\partial t^2} = \nabla^2 c^2 (\chi + \beta \chi^2) + O(\theta \chi^2, \chi^3) + \cdots, \tag{2.9}$$

where $\chi = \rho'/\rho_0$ is the density ratio and $\beta = 1 + (\rho/c)[\partial c(\rho_0)/\partial \rho)]$ the nonlinear parameter of the medium. We further discuss the nonlinear wave equation in Chap. 8, where we demonstrate its relationship to the parabolic equation and show how it can be used to solve problems directly in the time domain without resorting to Fourier synthesis.

2.1.2 The Linear Wave Equation

The linear approximations, which lead to the acoustic wave equation, involve retaining only first-order terms in the hydrodynamic equations [1, 2]. To lowest order, (2.1)–(2.4) become

$$\frac{\partial \rho'}{\partial t} = -\nabla \cdot (\rho_0 \mathbf{v}), \tag{2.10}$$

$$\frac{\partial \mathbf{v}}{\partial t} = -\frac{1}{\rho_0} \nabla p'(\rho), \tag{2.11}$$

$$\frac{\partial p'}{\partial t} = c^2 \left(\frac{\partial \rho'}{\partial t} + \mathbf{v} \cdot \nabla \rho_0 \right), \tag{2.12}$$

where we note that if ρ_0 is constant, the last equation can also be written as

$$p' = \rho' c^2. \tag{2.13}$$

2.1.2.1 Wave Equation for Pressure

Considering that the time scale of oceanographic changes is much longer than the time scale of acoustic propagation, we will assume that the material properties ρ_0 and c^2 are independent of time. Then, take the partial derivative of (2.10) with respect to time and the divergence of (2.11); next, interchange the derivative operations and use (2.12) to obtain a wave equation for pressure,

$$\rho \nabla \cdot \left(\frac{1}{\rho} \nabla p \right) - \frac{1}{c^2} \frac{\partial^2 p}{\partial t^2} = 0, \tag{2.14}$$

where we have omitted the primes for pressure and density perturbations. If the density is constant in space, (2.14) can be replaced by the standard form of the wave equation,

$$\nabla^2 p - \frac{1}{c^2} \frac{\partial^2 p}{\partial t^2} = 0. \tag{2.15}$$

Using (2.12), the exact same equations for the density perturbation are obtained. Note that the appearance of c in the wave equation identifies it as the speed of sound, i.e., the speed of the propagating wave.

2.1.2.2 Wave Equation for Particle Velocity

Alternatively, we can take the divergence of (2.10) and the time derivative of (2.11), and combine the two using (2.12) to arrive at the wave equation for the particle velocity

$$\frac{1}{\rho} \nabla \left(\rho c^2 \nabla \cdot \mathbf{v} \right) - \frac{\partial^2 \mathbf{v}}{\partial t^2} = \mathbf{0}. \tag{2.16}$$

This form of the wave equation is a vector equation coupling the three spatial components of the particle velocity. It involves spatial derivatives of both density and sound speed, and is therefore rarely used, except for uni-axial propagation problems.

2.1.2.3 Wave Equation for Velocity Potential

If the density is constant or slowly varying, the vector equation (2.16) can be transformed into a simple scalar wave equation by introducing the velocity potential ϕ, defined by

$$\mathbf{v} = \nabla\phi. \tag{2.17}$$

Substituting (2.17) together with the constant density condition $\nabla\rho = \mathbf{0}$, into (2.16), the latter takes the form

$$\nabla\left(c^2\,\nabla^2\phi - \frac{\partial^2\phi}{\partial t^2}\right) = \mathbf{0}. \tag{2.18}$$

This equation is clearly satisfied if ϕ satisfies the simple wave equation

$$\nabla^2\phi - \frac{1}{c^2}\,\frac{\partial^2\phi}{\partial t^2} = 0, \tag{2.19}$$

which is identical to the pressure wave equation, (2.15). Both equations are valid for varying sound speed, but for constant density only.

We note that there is a simple relationship between velocity and pressure for plane-wave solutions to the wave equation. This *impedance relation* is easily found using the velocity potential form of the wave equation with the solution $\phi = f(x - ct)$. From (2.17), $v_x = \partial\phi/\partial x = f'(x - ct)$, and from the linearized Euler equation (2.11), $p = -\rho\,\partial\phi/\partial t = \rho_0 c\,f'(x - ct)$, where f' denotes a derivative with respect to the argument of the function f. Comparing the pressure and velocity expressions yields the plane-wave impedance relation,

$$\frac{p}{v_x} = \rho_0 c. \tag{2.20}$$

2.1.2.4 Wave Equation for Displacement Potential

By using the kinematic relation between velocity and displacement $\mathbf{v} = \partial\mathbf{u}/\partial t$, it is easily shown that the displacement potential ψ, defined by

$$\mathbf{u} = \nabla\psi \tag{2.21}$$

is governed by a simple wave equation as well,

$$\nabla^2\psi - \frac{1}{c^2}\frac{\partial^2\psi}{\partial t^2} = 0. \tag{2.22}$$

As was the case for the other wave equations (2.15) and (2.19), also (2.22) is valid only for media with constant density. However, discrete changes in density can be handled through appropriate boundary conditions between regions of constant density. For such problems the boundary conditions require continuity of pressure and displacement (or velocity), and the potentials become discontinuous.

From the kinematic relations between displacements and velocities, (2.10), (2.12), and (2.21), we obtain the following expression for the acoustic pressure in terms of the displacement potential,

$$p = -K\,\nabla^2\psi \tag{2.23}$$

with K being the *bulk modulus*,

$$K = \rho c^2. \tag{2.24}$$

Equation (2.23) is the constitutive equation for an ideal, linearly elastic fluid (*Hooke's law*). Combination of (2.22)–(2.24), yields the alternative expression for the acoustic pressure,

$$p = -\rho\frac{\partial^2\psi}{\partial t^2}. \tag{2.25}$$

2.1.2.5 Source Representation

Underwater sound is produced by natural or artificial phenomena through forced mass injection. Such forcing terms were neglected in the mass conservation equation (2.10), and therefore also in the derived wave equations. However, such terms are easily included, leading to inhomogeneous wave equations, e.g., for the displacement potential

$$\nabla^2\psi - c^{-2}\frac{\partial^2\psi}{\partial t^2} = f(\mathbf{r}, t), \tag{2.26}$$

where $f(\mathbf{r}, t)$ represents the volume injection as a function of space and time. Similar inhomogeneous forms of the wave equations for pressure or velocity are easily derived. In Sect. 2.3.2, we derive the expression for the forcing term corresponding to a simple point source.

2.1.2.6 Solution of the Wave Equation

The numerical methods described in Chaps. 3–7 all attempt to solve (2.26), or the equivalent pressure or velocity potential equations, with associated boundary and

radiation conditions. The major difference between the various techniques is the mathematical manipulation of (2.26) being applied before actual implementation of the solution. Another difference is the form of the wave equation used. Density changes in the stratified ocean are primarily of discrete nature, e.g., at the seabed and between layers in the bottom, whereas the density in the water column is virtually constant. Therefore, the simpler equations are usually used in numerical solutions which easily handle internal boundary conditions. On the other hand, some numerical methods treat internal discontinuities as smooth transitions, and such methods should clearly be based on (2.14).

The most direct approach is the *Finite Difference Method* (FDM), which directly discretizes (2.26) in space and time though approximations of the differential operators. This solution technique is described in Sect. 7.3.

The *Finite Element Method* (FEM) instead discretizes the medium and time into small blocks within which (2.26) can be solved analytically in terms of a selected set of degrees-of-freedom. The connectivity between the elements then leads to a linear system of equations in the degrees-of-freedom to be solved. Details on the FEM solution technique is given in Sect. 7.4.

In spite of the generality of direct, discrete methods such as FDM and FEM, their importance in ocean acoustics is rather limited due to excessive computational requirement. Thus, the FDM/FEM methods all require discretization of the acoustic field to a small fraction of a wavelength, and realistic propagation problems involve distances of hundreds to thousands of wavelengths.

The alternative numerical approaches described in Chaps. 3–6 are much more tractable in terms of numerical requirements and are therefore in more widespread use in the ocean acoustics community. However, the improved efficiency is obtained at the cost of generality. Thus, all these approaches are based on assumptions allowing for simplifying mathematical manipulations of the wave equation. These assumptions are identical to the ones applied in theoretical acoustics to obtain analytical solutions in one or more of the 4 dimensions (3 in space and 1 in time) of the total problem. All of the widespread numerical techniques could therefore, in fact, be considered hybrid analytical–numerical approaches, in contrast to the traditional terminology, where the two approaches are considered distinctly different. As an example, the Wavenumber Integration (WI) technique described in Chap. 4 only differs from analytical integral representations for propagation in a plane-parallel waveguide through the approach used to solve the system of linear equations in the unknown amplitudes, linked via the boundary conditions. The first uses a numerical equation solver, the latter pen and paper. In both cases, the final integral must be evaluated numerically.

In general, the numerical approaches applied in ocean acoustics today are based on important theoretical developments within the field of wave propagation over the past five decades, starting with the pioneering work on ocean waveguide theory by Pekeris [3]. Of particular importance are the various assumptions and approximations made in order to solve realistic propagation problems with the computer hardware at hand. For acousticians who consider applying one of the available numerical techniques, it is important to understand the limitations of the different techniques.

In the rest of this chapter, we therefore describe ocean-acoustic waveguide theory as it relates to the derivation of the numerical solution techniques. For a detailed description of the underlying theories, reference is made to the journal literature as well as the many textbooks devoted to the area of theoretical acoustics [2, 4–11].

2.2 The Helmholtz Equation

Since the coefficients to the two differential operators in (2.26) are independent of time, the dimension of the wave equation can be reduced to three by use of the frequency–time Fourier transform pair,

$$f(t) = \frac{1}{2\pi} \int_{-\infty}^{\infty} f(\omega)\, \mathrm{e}^{-\mathrm{i}\omega t}\, \mathrm{d}\omega, \tag{2.27}$$

$$f(\omega) = \int_{-\infty}^{\infty} f(t)\, \mathrm{e}^{\mathrm{i}\omega t}\, \mathrm{d}t \tag{2.28}$$

leading to the frequency-domain wave equation, or *Helmholtz equation*,

$$\left[\nabla^2 + k^2(\mathbf{r})\right] \psi(\mathbf{r}, \omega) = f(\mathbf{r}, \omega), \tag{2.29}$$

where $k(\mathbf{r})$ is the medium wavenumber at radial frequency ω,

$$k(\mathbf{r}) = \frac{\omega}{c(\mathbf{r})}. \tag{2.30}$$

It should be pointed out that although the Helmholtz equation (2.29), due to the reduction in the dimension of this PDE, is simpler to solve than the full wave equation, (2.26), this simplification is achieved at the cost of having to evaluate the inverse Fourier transform, (2.27). However, many ocean acoustic applications are of narrow-band nature. The Helmholtz equation, rather than the wave equation, therefore forms the theoretical basis for the most important numerical methods, including the Wavenumber Integration (WI), Normal Mode (NM) and Parabolic Equation (PE) approaches, described in Chaps. 4, 5, and 6, respectively.

It is important to stress the difference between narrow-band processing in ocean acoustics and wide-band processing in seismics. The latter approach is viable because the length scale of the environmental features addressed in seismic experiments is of the same order of magnitude as the seismic wavelengths, and the time scales of the experiments are such that cross-spectral coherence can be assumed. In other words, seismic experiments are characterized by very few interactions with any single boundary, whereas a typical ocean acoustic experiment can have hundreds or thousands of interactions. This is basically the reason why time-domain approaches such as FDM and FEM have never gained widespread

popularity in ocean acoustics, whereas they are very important numerical analysis tools in the seismic community. There is, however, much virtue to time-domain solutions in terms of physical understanding, and time-domain solutions are produced routinely for exactly that purpose, both by Fourier synthesis and by direct time-domain solutions of the wave equation (see Chap. 8).

The environmental body forces such as gravity and magnetism are of no significance to acoustic propagation except for the effect of gravity on the sound speed variation in depth. The only body forces of importance are the acoustic sources, which include artificial sound generators as well as natural ones, e.g., noise generation at the sea surface and by marine animals. Since these sources are local in nature, most of the ocean environment is sourceless, with the wave field satisfying the homogeneous Helmholtz equation,

$$\left[\nabla^2 + k^2(\mathbf{r})\right]\psi(\mathbf{r},\omega) = 0. \tag{2.31}$$

In spite of the relative simplicity of (2.31), there is no universal solution technique available. The actual solution technique that can be applied depends on the following factors:

- Dimensionality of the problem.
- Medium wavenumber variation $k(\mathbf{r})$, i.e., the sound speed variation $c(\mathbf{r})$.
- Boundary conditions.
- Source–receiver geometry.
- Frequency and bandwidth.

The Helmholtz equation (2.31) is a three-dimensional, elliptic partial differential equation, which can be solved either by analytical or numerical methods or by a combination of the two. The most convenient method is determined by the complexity of the *medium properties* and of the *boundary conditions* for the actual problem. Thus, for some problems the environment is so complex that only direct discrete methods such as FDM and FEM are applicable, whereas typical canonical problems are characterized by simple environmental models for which analytical methods are applicable. However, in general an optimum approach is a hybridization of analytical and numerical methods, and all the computational methods described in the following are of this category. Although these methods all have the Helmholtz equation as the starting point, they differ in the degree to which the analytical and numerical components are utilized in the solution scheme. Since the analytical methods are restricted to canonical problems with simple geometries, the computational methods with a large analytical component are therefore also restricted to problems where the actual environment is well represented by an idealized environmental model.

We here review the analytical approaches to the solution of the Helmholtz equation which, to various degrees, form the mathematical basis for the computational methods described in the next chapters. Further, we use these analytical methods to address the basic physics associated with propagation in the ocean waveguide.

2.3 Homogeneous Media

A very simple acoustic environment is that of a homogeneous medium with wavenumber $k(\mathbf{r}) = k$, occupying the volume V bounded by the surface S, shown in Fig. 2.1. In spite of the simplicity, this problem is well-suited to illustrate the basic principles of the solution of the Helmholtz equation.

2.3.1 Coordinate Systems

In a homogeneous medium, the homogeneous Helmholtz equation, (2.31), is easily solved, with a choice of coordinate system being imposed by the source and boundary geometry. Thus, if plane wave propagation is considered, a *Cartesian coordinate system* $\mathbf{r} = (x, y, z)$ is the natural choice, with the Laplace operator,

$$\nabla^2 = \frac{\partial^2}{\partial x^2} + \frac{\partial^2}{\partial y^2} + \frac{\partial^2}{\partial z^2} \tag{2.32}$$

yielding plane wave solutions of the form

$$\psi(x, y, z) = \begin{cases} A\, \mathrm{e}^{\mathrm{i}\mathbf{k}\cdot\mathbf{r}} \\ B\, \mathrm{e}^{-\mathrm{i}\mathbf{k}\cdot\mathbf{r}}, \end{cases} \tag{2.33}$$

where $\mathbf{k} = (k_x, k_y, k_z)$ is the wave vector and A and B are arbitrary amplitudes.

For a single plane-wave component, the coordinate system can be aligned with the propagation direction, e.g., with $k_y, k_z = 0$, yielding the simple solution

$$\psi(x) = \begin{cases} A\, \mathrm{e}^{\mathrm{i}kx} \\ B\, \mathrm{e}^{-\mathrm{i}kx}, \end{cases} \tag{2.34}$$

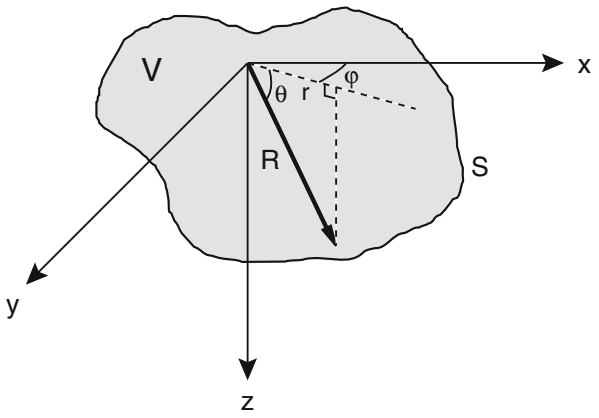

Fig. 2.1 Homogeneous medium occupying the volume V bounded by the surface S

which corresponds to a forward- and a backward-propagating plane wave solution with time dependence $\exp(-\mathrm{i}\omega t)$.

Similarly, the field produced by an infinite, homogeneous line source is conveniently described in a *cylindrical coordinate system* $\mathbf{r} = (r, \varphi, z)$, with the z-axis coinciding with the source. Then, the field satisfies the homogeneous Helmholtz equation for $r > 0$ with the Laplace operator,

$$\nabla^2 = \frac{1}{r}\frac{\partial}{\partial r} r \frac{\partial}{\partial r} + \frac{1}{r^2}\frac{\partial^2}{\partial \varphi^2} + \frac{\partial^2}{\partial z^2}. \tag{2.35}$$

For a uniform line source, the field only varies with range r, reducing the Helmholtz equation to the Bessel equation,

$$\left[\frac{1}{r}\frac{\partial}{\partial r} r \frac{\partial}{\partial r} + k^2\right] \psi(r) = 0 \tag{2.36}$$

with the solution

$$\psi(r) = \begin{cases} A\, J_0(kr) \\ B\, Y_0(kr) \end{cases} \tag{2.37}$$

or, in terms of Hankel functions,

$$\psi(r) = \begin{cases} C H_0^{(1)}(kr) = C\,[J_0(kr) + \mathrm{i} Y_0(kr)] \\ D H_0^{(2)}(kr) = D\,[J_0(kr) - \mathrm{i} Y_0(kr)]\,. \end{cases} \tag{2.38}$$

The latter form represents diverging and converging cylindrical waves for $r \to \infty$, as is clear from the asymptotic form of the Hankel functions for $kr \to \infty$,

$$H_0^{(1)}(kr) \simeq \sqrt{\frac{2}{\pi kr}}\, \mathrm{e}^{\mathrm{i}(kr - \pi/4)}, \tag{2.39}$$

$$H_0^{(2)}(kr) \simeq \sqrt{\frac{2}{\pi kr}}\, \mathrm{e}^{-\mathrm{i}(kr - \pi/4)}. \tag{2.40}$$

These asymptotics also show that the cylindrically symmetric field produced by a line source decays in amplitude proportionally to $r^{-1/2}$. Approaching the source, the line source field exhibits a *logarithmic singularity*.

In the case of an omni-directional point source, the field only depends on the range from the source, and the solution is conveniently described in a *spherical coordinate system*, with the reduced Helmholtz equation being

$$\left[\frac{1}{r^2}\frac{\partial}{\partial r} r^2 \frac{\partial}{\partial r} + k^2\right] \psi(r) = 0, \tag{2.41}$$

which has the solutions

$$\psi(r) = \begin{cases} (A/r)\,\mathrm{e}^{\mathrm{i}kr} \\ (B/r)\,\mathrm{e}^{-\mathrm{i}kr}. \end{cases} \tag{2.42}$$

Again, these solutions correspond to diverging and converging spherical waves with the amplitude decaying proportional to r^{-1} in range.

The term *geometrical spreading loss* refers to these geometries. Thus, *cylindrical spreading loss* is proportional to $r^{-1/2}$ and *spherical spreading loss* is proportional to r^{-1}.

2.3.2 Source in Unbounded Medium

The derivation of the field expression for an acoustic source in an unbounded medium is a simple example of how the solution of the homogeneous wave equation described above is combined with the boundary conditions to yield the solution to a particular problem.

Assume an acoustic field is produced in an infinite, homogeneous fluid by a small sphere of radius a (Fig. 2.2), with the surface displacement given as

$$u_r(t, a) = U(t). \tag{2.43}$$

In the homogeneous fluid, the field will be omni-directional, with the radial displacement

$$u_r = \frac{\partial \psi(r, t)}{\partial r}, \tag{2.44}$$

where the displacement potential ψ satisfies a homogeneous wave equation. By applying the Fourier transform to both the wave equation and the boundary condition at $r = a$, we obtain the Helmholtz equation (2.41) and the boundary condition,

$$u_r(a) = U(\omega). \tag{2.45}$$

The solution to the Helmholtz equation is a linear combination of the two independent solutions in (2.42), but since we assume the sphere is the only source in

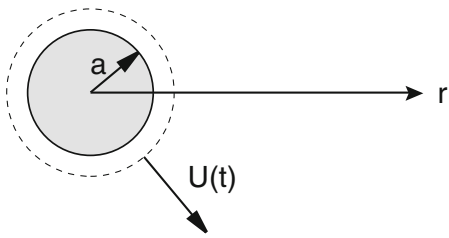

Fig. 2.2 Vibrating sphere in an infinite fluid medium

the infinite medium, we can apply the *radiation condition* of no incoming waves at infinity to require that $B = 0$, i.e.,

$$\psi(r) = A\,\frac{\mathrm{e}^{\mathrm{i}kr}}{r} \tag{2.46}$$

with the corresponding displacement field given by (2.44) as

$$u_r(r) = A\,\mathrm{e}^{\mathrm{i}kr}\left(\frac{\mathrm{i}k}{r} - \frac{1}{r^2}\right). \tag{2.47}$$

The amplitude A is now easily found from (2.45).

The *simple point source* corresponds to the case where the radius of the sphere is small compared to the acoustic wavelength, i.e., $ka \ll 1$, in which case the expression for the surface displacement takes the form

$$u_r(\omega, a) = A\,\mathrm{e}^{\mathrm{i}ka}\,\frac{\mathrm{i}ka - 1}{a^2} \simeq -\frac{A}{a^2} \tag{2.48}$$

yielding

$$A = -a^2\,U(\omega). \tag{2.49}$$

Defining the *source strength* $S_\omega = 4\pi a^2\,U(\omega)$ as the volume-injection amplitude produced by the source at frequency ω, we then obtain the solution for the field in the fluid,

$$\psi(r) = -S_\omega\,\frac{\mathrm{e}^{\mathrm{i}kr}}{4\pi r}. \tag{2.50}$$

The source strength S_ω is of unit m^3, or volume. If we had based the derivation on velocity potentials, the source strength would be of unit m^3/s, representing volume rate.

The fraction in (2.50) is called the *Green's function*,

$$g_\omega(r, 0) = \frac{\mathrm{e}^{\mathrm{i}kr}}{4\pi r} \tag{2.51}$$

or, in general, for a source at $\mathbf{r} = \mathbf{r}_0$,

$$g_\omega(\mathbf{r}, \mathbf{r}_0) = \frac{\mathrm{e}^{\mathrm{i}kR}}{4\pi R}, \quad R = |\mathbf{r} - \mathbf{r}_0|. \tag{2.52}$$

The Green's function satisfies the inhomogeneous Helmholtz equation,

$$\left[\nabla^2 + k^2\right] g_\omega(\mathbf{r}, \mathbf{r}_0) = -\delta(\mathbf{r} - \mathbf{r}_0), \tag{2.53}$$

which is easily verified by integrating (2.53) over a small volume containing the source point $\mathbf{r_0}$. The inhomogeneous Helmholtz equation for a simple point source of strength S_ω at point $\mathbf{r_0}$ is therefore,

$$\left[\nabla^2 + k^2\right] \psi(\omega, \mathbf{r}) = S_\omega \, \delta(\mathbf{r} - \mathbf{r_0}). \tag{2.54}$$

The Green's function of the time-domain wave equation is obtained by the Fourier transform of g_ω as specified by (2.27),

$$g_t(\mathbf{r}, \mathbf{r_0}) = \frac{\delta\,(R/c - t)}{4\pi R} \tag{2.55}$$

and can be thought of as the impulse response in an unbounded medium. Note that the Green's function is symmetric in $\mathbf{r}$ and $\mathbf{r_0}$,

$$g_\omega(\mathbf{r}, \mathbf{r_0}) = g_\omega(\mathbf{r_0}, \mathbf{r}) \tag{2.56}$$

in accordance with the *principle of reciprocity* for the Green's function described in Appendix 1.

2.3.3 Source in Bounded Medium

Extending the analysis to a more realistic acoustic environment we next consider the problem illustrated in Fig. 2.3, where the medium occupies the volume V bounded by the surface S, with prescribed boundary conditions. An acoustic field is produced by a distribution of body forces $f(\mathbf{r})$ within the volume V, and the displacement potential $\psi(\mathbf{r})$ must, therefore, satisfy the inhomogeneous Helmholtz equation,

$$\left[\nabla^2 + k^2\right] \psi(\mathbf{r}) = f(\mathbf{r}). \tag{2.57}$$

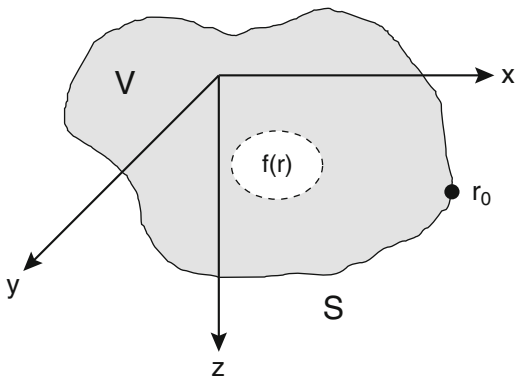

Fig. 2.3 Sources in a volume V bounded by the surface S

In the preceding section, we introduced the free-field Green's function $g_\omega(\mathbf{r}, \mathbf{r}_0)$ satisfying (2.53). This was just a particular solution to (2.53) satisfying the radiation condition. In the case of a *boundary value problem*, we need the general solution of (2.53) which is a sum of a particular solution such as $g_\omega(\mathbf{r}, \mathbf{r}_0)$ and a homogeneous solution $H_\omega(\mathbf{r})$, with the superposition of the two solutions satisfying the boundary conditions as well as the radiation conditions (for semi-infinite media).

We, therefore, introduce the *general Green's function* as

$$G_\omega(\mathbf{r}, \mathbf{r}_0) = g_\omega(\mathbf{r}, \mathbf{r}_0) + H_\omega(\mathbf{r}), \tag{2.58}$$

where $H_\omega(\mathbf{r})$ is any function satisfying the homogeneous Helmholtz equation,

$$\left[\nabla^2 + k^2\right] H_\omega(\mathbf{r}) = 0. \tag{2.59}$$

The general Green's function then satisfies the same Helmholtz equation as $g_\omega(\mathbf{r}, \mathbf{r}_0)$,

$$\left[\nabla^2 + k^2\right] G_\omega(\mathbf{r}, \mathbf{r}_0) = -\delta(\mathbf{r} - \mathbf{r}_0). \tag{2.60}$$

By multiplying (2.57) by $G_\omega(\mathbf{r}, \mathbf{r}_0)$ and (2.60) by $\psi(\mathbf{r})$ and subtracting the two, we obtain

$$G_\omega(\mathbf{r}, \mathbf{r}_0)\, \nabla^2 \psi(\mathbf{r}) - \psi(\mathbf{r})\, \nabla^2 G_\omega(\mathbf{r}, \mathbf{r}_0) = \psi(\mathbf{r})\, \delta(\mathbf{r} - \mathbf{r}_0) + G_\omega(\mathbf{r}, \mathbf{r}_0)\, f(\mathbf{r}). \tag{2.61}$$

Interchange of $\mathbf{r}$ and $\mathbf{r}_0$ followed by integration over the volume with respect to $\mathbf{r}_0$ then yields

$$\begin{aligned} &\int_{\mathrm{V}} \left[G_\omega(\mathbf{r}, \mathbf{r}_0)\, \nabla_0^2\, \psi(\mathbf{r}_0) - \psi(\mathbf{r}_0)\, \nabla_0^2\, G_\omega(\mathbf{r}, \mathbf{r}_0)\right] \mathrm{d}V_0 \\ &\quad = \int_{\mathrm{V}} \psi(\mathbf{r}_0)\, \delta(\mathbf{r} - \mathbf{r}_0)\, \mathrm{d}V_0 + \int_{\mathrm{V}} f(\mathbf{r}_0)\, G_\omega(\mathbf{r}, \mathbf{r}_0)\, \mathrm{d}V_0, \end{aligned} \tag{2.62}$$

where it has been assumed that the Green's function is symmetric, i.e., $G_\omega(\mathbf{r}, \mathbf{r}_0) = G_\omega(\mathbf{r}_0, \mathbf{r})$. We will discuss this property in detail in Appendix 1. Using integration by parts (see Appendix 1), we now change the integration on the left-hand side to a surface integral and obtain,

$$\psi(\mathbf{r}) = \int_{\mathrm{S}} \left[G_\omega(\mathbf{r}, \mathbf{r}_0)\, \frac{\partial \psi(\mathbf{r}_0)}{\partial \mathbf{n}_0} - \psi(\mathbf{r}_0)\, \frac{\partial G_\omega(\mathbf{r}, \mathbf{r}_0)}{\partial \mathbf{n}_0} \right] \mathrm{d}S_0 - \int_{\mathrm{V}} f(\mathbf{r}_0)\, G_\omega(\mathbf{r}, \mathbf{r}_0)\, \mathrm{d}V_0, \tag{2.63}$$

where $\mathbf{n}_0$ is the outward-pointing normal on the surface. Equation (2.63) is *Green's theorem* for sources in a bounded medium. By letting the field points $\mathbf{r}$ be on the boundary, (2.63) provides an integral equation, which should be solved for the field and its normal derivative at the boundary. Then (2.63) can be applied to provide the field at any point $\mathbf{r}$ inside the volume V.

Green's theorem provides the most general formulation for acoustic boundary-value problems, but its use is highly dependent on the ability to solve the integral equation. Numerical solution can always be applied, but for some types of canonical problems, closed form analytical solutions are also possible. This is due to the fact that the general Green's function is arbitrary in the sense that the only requirements are that it must be symmetric and satisfy (2.60) everywhere within the volume V; otherwise there are no requirements to the particular choice of the homogeneous solution $H_\omega(\mathbf{r})$. We can, therefore, choose a homogeneous solution which simplifies the solution of the integral equation. For example, choosing the homogeneous solution such that the Green's function vanishes on the boundary will remove half of the kernel of the surface integral in (2.63). For some problems, a Green's function can be found which satisfies the same boundary conditions as the field on parts of the boundary. In that case the two terms in the kernel of the surface integral are identical, eliminating the integral on that part of the boundary. Finally, it should be noted that the surface S does not have to coincide with the physical boundary; Green's theorem is valid for any volume containing the sources.

Green's theorem will be applied in Sect. 2.3.4 to solve a simple boundary value problem for which a well-known solution exists. However, we first apply it to derive a formal representation of the radiation condition which any field in an infinite medium must satisfy.

Let the surface S be a sphere centered at the receiver point $\mathbf{r}$ and containing all areas of the medium where sources are present. Since the medium is infinite, the total field is obtained as an integral over all sources of the free-field Green's function, (2.52), times the source strengths, i.e., for general volume source distributions,

$$\psi(\mathbf{r}) = -\int_V f(\mathbf{r}_0)\, g_\omega(\mathbf{r}, \mathbf{r}_0)\, \mathrm{d}V_0. \tag{2.64}$$

By comparing this expression with Green's theorem, (2.63), we find that the surface integral over the sphere must vanish,

$$\int_S \left[g_\omega(\mathbf{r}, \mathbf{r}_0)\, \frac{\partial \psi(\mathbf{r}_0)}{\partial \mathbf{n}_0} - \psi(\mathbf{r}_0)\, \frac{\partial g_\omega(\mathbf{r}, \mathbf{r}_0)}{\partial \mathbf{n}_0} \right] \mathrm{d}S_0 = 0. \tag{2.65}$$

With the radius of the sphere being R, we can then insert the free-field Green's function from (2.52) to yield for $R \to \infty$

$$\int_S \frac{\mathrm{e}^{\mathrm{i}kR}}{4\pi R} \left[\frac{\partial \psi(\mathbf{r}_0)}{\partial R} - \mathrm{i}k\, \psi(\mathbf{r}_0) \right] \mathrm{d}S_0 = 0. \tag{2.66}$$

Since the radius R of the circle is large but arbitrary, the integrand in (2.66) must decay more rapidly than R^{-2} to have the surface integral properly converge, which leads to the *radiation condition*,

$$R \left[\frac{\partial}{\partial R} - \mathrm{i}k \right] \psi(\mathbf{r}_0) \to 0, \quad R = |\mathbf{r} - \mathbf{r}_0| \to \infty. \tag{2.67}$$

2.3.4 Point Source in Fluid Halfspace

As an example of the use of Green's theorem to boundary value problems, we apply it to the simplest possible example of a bounded acoustic medium, which is the fluid halfspace shown in Fig. 2.4. The upper halfspace is assumed to be a vacuum, and the boundary condition to be satisfied by the field in the fluid halfspace therefore simply is that the pressure must vanish at the free surface ($z = 0$). We have here introduced a Cartesian coordinate system with the origin on the surface and with the z-axis perpendicular to the surface. A simple point source is assumed to be placed at $\mathbf{r}_s = (x_s, y_s, z_s)$.

The pressure is derived from the displacement potential as

$$p(\mathbf{r}) = \rho\omega^2\,\psi(\mathbf{r}) \tag{2.68}$$

and we can therefore replace the pressure-release boundary condition by the condition

$$\psi(\mathbf{r}_0) \equiv 0, \quad \mathbf{r}_0 = (x, y, 0). \tag{2.69}$$

The field in the fluid halfspace is determined by Green's theorem, (2.63), which upon insertion of the boundary conditions, (2.69), takes the form

$$\psi(\mathbf{r}) = \int_S G_\omega(\mathbf{r}, \mathbf{r}_0)\,\frac{\partial\psi(\mathbf{r}_0)}{\partial\mathbf{n}_0}\,\mathrm{d}S_0 - \int_V f(\mathbf{r}_0)\,G_\omega(\mathbf{r}, \mathbf{r}_0)\,\mathrm{d}V_0. \tag{2.70}$$

For a simple point source, (2.54) shows that the volume force term takes the form

$$f(\mathbf{r}_0) = S_\omega\,\delta(\mathbf{r}_0 - \mathbf{r}_s). \tag{2.71}$$

If, furthermore, we choose the general Green's function such that $G_\omega(\mathbf{r}, \mathbf{r}_0) \equiv 0$ for $\mathbf{r}_0 = (x, y, 0)$, then (2.70) simply becomes

$$\psi(\mathbf{r}) = -S_\omega\,G_\omega(\mathbf{r}, \mathbf{r}_s). \tag{2.72}$$

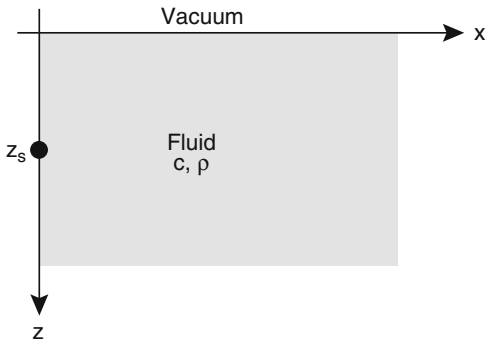

Fig. 2.4 Point source in a fluid halfspace

For this simple case it is straightforward to choose a Green's function which vanishes on the free surface $z = 0$,

$$\begin{aligned} G_\omega(\mathbf{r}, \mathbf{r}_0) &= g_\omega(\mathbf{r}, \mathbf{r}_0) + H_\omega(\mathbf{r}) \\ &= \frac{e^{ikR}}{4\pi R} - \frac{e^{ikR'}}{4\pi R'} \end{aligned} \tag{2.73}$$

with

$$R = \sqrt{(x - x_s)^2 + (y - y_s)^2 + (z - z_s)^2}, \tag{2.74}$$

$$R' = \sqrt{(x - x_s)^2 + (y - y_s)^2 + (z + z_s)^2}. \tag{2.75}$$

The solution for the displacement potential now takes the form

$$\psi(\mathbf{r}) = -S_\omega \left[\frac{e^{ikR}}{4\pi R} - \frac{e^{ikR'}}{4\pi R'} \right], \tag{2.76}$$

which corresponds to the superposition of the free-space solutions for the source at depth $z = z_s$ and an image source at $z = -z_s$ in the vacuum halfspace. Thus, the solution obtained by Green's theorem is identical to the so-called *mirror* or *image method*, and the constructive and destructive interference of these two fields give rise to the well-known Lloyd-mirror pattern described in Sect. 1.4.2.

In general, an analytical solution is not easily obtained by Green's theorem. The critical issue is the determination of a Green's function which satisfies the same boundary conditions as the displacement potential on the boundary, thus eliminating the surface integral entirely. This is straightforward for problems with simple boundary geometry and homogeneous boundary conditions, as was the case in the halfspace problem. For heterogeneous media with simple boundary geometry but inhomogeneous boundary conditions, other approaches such as those described in the following sections are more feasible.

The generality of Green's theorem, on the other hand, makes it applicable to problems with complex boundary geometry, where it can be used to formulate an integral equation which can be solved numerically. Here, the numerical implementation via the Boundary Element Method (BEM) is extremely powerful for radiation and scattering problems, and it has become an increasingly popular numerical approach in structural acoustics, seismology, and recently, to some degree, also in ocean acoustics (Sect. 7.5).

2.3.5 Transmission Loss

In underwater acoustics, the field is traditionally expressed in terms of *transmission loss*, defined as

$$\mathrm{TL}(\mathbf{r}, \mathbf{r}_s) = -10 \log \frac{I(\mathbf{r}, \mathbf{r}_s)}{I_0(\mathbf{r}_s)} = -10 \log \left(\frac{Z_0(\mathbf{r}_s)}{Z(\mathbf{r}, \mathbf{r}_s)} \left| \frac{p(\mathbf{r}, \mathbf{r}_s)}{p_0(\mathbf{r}_s)} \right|^2 \right), \tag{2.77}$$

where $Z_0(\mathbf{r}_s)$, $Z(\mathbf{r}, \mathbf{r}_s)$ are the acoustic impedances at the source and the field point, respectively, and $p(\mathbf{r}, \mathbf{r}_s)$ is the acoustic pressure at point $\mathbf{r}$ for a simple point source at point $\mathbf{r}_s$, and $p_0(\mathbf{r}_s)$ is the pressure produced at a distance of 1 m from the same source in an *infinite, homogeneous medium* with impedance $Z_0(\mathbf{r}_s)$. For a bounded medium, p_0 is generally different from the actual pressure due to the presence of the reverberant field from the boundaries. This particular normalization should be kept in mind when developing or comparing numerical algorithms. In what follows, we take the impedance at the source and field points to be the same.

With the pressure at range r from the source given in terms of the displacement potential as

$$p(r) = \rho\omega^2 \, \psi(\omega, r) \tag{2.78}$$

together with the expression for $\psi(\omega, r)$ in (2.50), we can normalize the source to yield a pressure amplitude of unity for $r = 1$, by assuming the source strength,

$$S_\omega = -\frac{4\pi}{\rho\omega^2}. \tag{2.79}$$

This particular source strength is of unit $\mathrm{m^3 s^2/kg}$, or $\mathrm{m^2/Pa}$, and represents the volume injection amplitude necessary to produce a pressure amplitude of 1 Pa at 1 m distance from the source, at the radial frequency ω. It is clear from this expression that a high-frequency source needs much less volume injection to produce a certain pressure than does a low-frequency source.

Using this source normalization, and defining the *transmission loss pressure* as the ratio,

$$P(\mathbf{r}, \mathbf{r}_s) = \frac{p(\mathbf{r}, \mathbf{r}_s)}{p_0(\mathbf{r}_s)} \tag{2.80}$$

the associated displacement potential $\Psi = P/(\rho\omega^2)$, is found by solving the inhomogeneous wave equation,

$$\left[\nabla^2 + k^2\right] \Psi(\mathbf{r}, \mathbf{r}_s) = -\frac{4\pi}{\rho\omega^2} \, \delta(\mathbf{r} - \mathbf{r}_s). \tag{2.81}$$

Alternatively, by inserting the relation between pressure and potential, we can formulate the wave equation directly for the transmission loss pressure,

$$\left[\nabla^2 + k^2\right] P(\mathbf{r}, \mathbf{r}_s) = -4\pi \, \delta(\mathbf{r} - \mathbf{r}_s). \tag{2.82}$$

Since the transmission loss definition refers to the field in an infinite medium, the same forcing term must be used in the inhomogeneous form of the wave equation (2.14) for media with density variation,

$$\rho\nabla \cdot \left[\rho^{-1} \, \nabla P(\mathbf{r}, \mathbf{r}_s)\right] + k^2 P(\mathbf{r}, \mathbf{r}_s) = -4\pi \, \delta(\mathbf{r} - \mathbf{r}_s). \tag{2.83}$$

In the following chapters, these equations will be used variably, with the actual choice being dependent on the nature of the numerical solution technique. However, in the remainder of this chapter we concentrate on the simple wave equation as applied to cases that allow for analytical solutions.

2.4 Layered Media and Waveguides

In heterogeneous media, the sound speed and density varies in one or more space coordinates. In cases where the variation occurs as discrete discontinuities in the medium properties, the derivation of the linear wave equation, (2.15), is not valid at the discontinuity itself, and the problem therefore has to be formulated as a boundary value problem. For continuously varying media, the space dependency is directly included in the wave equation.

In reality, the ocean environment is a combination of the two, with the medium properties changing abruptly at the seabed and at subbottom interfaces between different geological strata, but with the sound speed varying more or less continuously in the water column. However, since the analytical approach is different in the two cases, we will describe the solution of the wave equation in discretely and continuously varying media separately. The numerical approaches, in general, have to combine the treatment of these two types of medium heterogeneity.

A simple discrete model of the ocean environment is shown in Fig. 2.5. It consists of a layered waveguide with plane, parallel interfaces and with each layer assumed to be homogeneous. Although simplified, such a model is reasonable for modeling propagation in many ocean-acoustic scenarios. Further, the fact that solutions can be obtained in terms of basic physical components makes the horizontally stratified ocean model attractive in terms of physical understanding of the underlying propagation mechanisms.

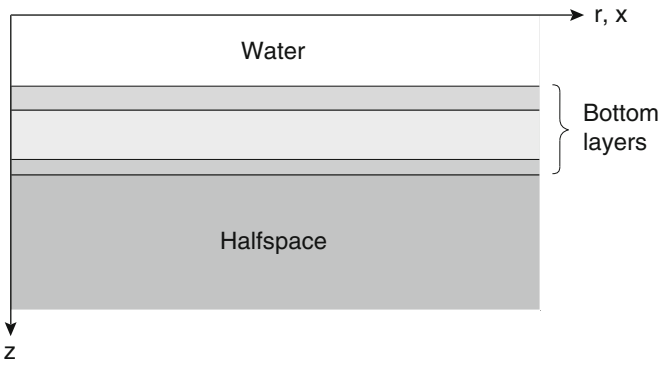

Fig. 2.5 Horizontally stratified environment

2.4.1 Integral Transform Techniques

The *integral transform technique* is a classical approach to boundary value problems for environments where both the coefficients of the *Helmholtz equation* and the *boundary conditions* are independent of one or more space coordinates. In such cases, the dimension of the wave equation and the boundary conditions can be reduced through the use of integral transforms, which is equivalent to the technique of *separation of variables*.

There are several classes of canonical problems for which separation of variables can be applied, including spherically stratified Earth models, and laminated spherical and cylindrical shells. However, in underwater acoustics the most important canonical geometry for which this powerful analytical technique can be applied is the *horizontally stratified* or *range-independent* waveguide shown in Fig. 2.5.

The properties of the horizontally stratified waveguide only depend on the depth z; all interfaces between the various media are plane and parallel. For this range-independent problem, the Helmholtz equation takes the form,

$$\left[\nabla^2 + k^2(z)\right]\psi(\mathbf{r}) = f(\mathbf{r}) \tag{2.84}$$

with the boundary conditions expressed in a general operator form as,

$$B\left[\psi(\mathbf{r})\right]|_{z=z_n} = 0, \quad n = 1 \cdots N \tag{2.85}$$

with z_n being the depth of interface number n.

Before proceeding we have to choose a convenient coordinate system. The half-space problem treated in Sect. 2.3.4 is a very simple example of a range-independent problem. However, there the boundary conditions were homogeneous and simple, and we chose a spherical coordinate system for solving the Helmholtz equation because the source was a simple point source. In general, the boundary conditions are the complicating factor, and they therefore control the choice of coordinate system. Thus, to apply separation of variables to the range-independent problem, we must choose a coordinate system for which one of the axes is normal to the horizontal interface.

2.4.1.1 Plane Propagation Problems

For plane problems such as those involving an infinite line source parallel to the stratification it is natural to choose a Cartesian coordinate system (x, y, z) with the z-axis perpendicular to the stratification and the y-axis parallel to the line source. The field then becomes independent of the y-coordinate, reducing the dimension of the Helmholtz equation to 2, the range x and the depth z, i.e., for a line source at $(x, z) = (0, z_s)$,

$$\left[\frac{\partial^2}{\partial x^2} + \frac{\partial^2}{\partial z^2} + k^2(z)\right]\psi(x, z) = S_\omega\, \delta(x)\, \delta(z - z_s). \tag{2.86}$$

We can now apply the Fourier transform pair,

$$f(x,z) = \int_{-\infty}^{\infty} f(k_x,z)\, \mathrm{e}^{\mathrm{i}k_x x}\, \mathrm{d}k_x, \tag{2.87}$$

$$f(k_x,z) = \frac{1}{2\pi}\int_{-\infty}^{\infty} f(x,z)\, \mathrm{e}^{-\mathrm{i}k_x x}\, \mathrm{d}x \tag{2.88}$$

to (2.86) to obtain the *depth-separated wave equation*,

$$\left[\frac{\mathrm{d}^2}{\mathrm{d}z^2} + (k^2 - k_x^2)\right]\psi(k_x,z) = S_\omega\, \frac{\delta(z-z_s)}{2\pi}. \tag{2.89}$$

We next use the Fourier transform of Green's theorem in the form of (2.72) to obtain,

$$\psi(k_x,z) = -S_\omega\, G_\omega(k_x,z,z_s), \tag{2.90}$$

where $G_\omega(k_x,z,z_s)$ is called the *depth-dependent Green's function*, which clearly must satisfy the same boundary conditions as $\psi(k_x,z)$ for (2.90) to be valid.

Since the depth-dependent Green's function $G_\omega(k_x,z,z_s)$ is the Fourier transform of the general Green's function, (2.58), it has the form,

$$G_\omega(k_x,z,z_s) = g_\omega(k_x,z,z_s) + H_\omega(k_x,z), \tag{2.91}$$

where $g_\omega(k_x,z,z_s)$ is the Fourier transform of the free-field Green's function satisfying the equation,

$$\left[\frac{\mathrm{d}^2}{\mathrm{d}z^2} + (k^2 - k_x^2)\right] g_\omega(k_x,z,z_s) = -\frac{\delta(z-z_s)}{2\pi}\,; \tag{2.92}$$

$H_\omega(k_x,x)$ satisfies the corresponding homogeneous differential equation.

Through (2.90) and (2.91), we have expressed the total solution as a *superposition* of the field produced by the source in an infinite medium and a homogeneous solution. The total field, of course, must satisfy the boundary conditions. Since the boundary conditions, (2.85), are independent of the horizontal coordinates, they can be Fourier transformed as well. The differential operators $B[\psi(\mathbf{r})]$ now become algebraic operations, yielding the boundary conditions for the depth-separated wave equation in the form

$$B\left[\psi(k_x,z_n)\right] = 0. \tag{2.93}$$

The solution is now obtained by determining the homogeneous solution $H_\omega(k_x,z)$ which, superimposed on the free-field Green's function $g_\omega(k_x,z,z_s)$, satisfies the boundary conditions in (2.93). The total spatial solution then follows by evaluating the inverse Fourier transform, (2.87).

2.4.1.2 Axisymmetric Propagation Problems

The more usual problem of a *simple point source* in a range-independent environment is treated in a similar way. Since the simple point source is omni-directional, the field only varies with depth and the horizontal range from the source. It is, therefore, natural to choose a *cylindrical coordinate system* for this problem, with the vertical z-axis passing through the source and the r-axis being parallel to the interfaces.

We can then integrate the Helmholtz equation, (2.84), with the Laplace operator given in (2.35), with respect to the azimuthal coordinate φ and apply the *Hankel transform* pair,

$$f(r,z) = \int_0^\infty f(k_r,z)\, J_0(k_r r)\, k_r \, \mathrm{d}k_r, \tag{2.94}$$

$$f(k_r,z) = \int_0^\infty f(r,z)\, J_0(k_r r)\, r \, \mathrm{d}r \tag{2.95}$$

to obtain the *depth-separated wave equation* for the cylindrical coordinate system,

$$\left[\frac{\mathrm{d}^2}{\mathrm{d}z^2} + (k^2 - k_r^2)\right] \psi(k_r,z) = S_\omega \frac{\delta(z-z_s)}{2\pi}. \tag{2.96}$$

Equation (2.96) is identical to the depth-separated wave equation for the Cartesian coordinate system. The solution of the depth-separated wave equation, therefore, proceeds identically in the two cases. Further, the transforms of the boundary conditions are identical in the two cases, and we can therefore use the solution of (2.96) as the kernel for both of the inverse transforms, (2.87) and (2.94), for the line source and point source fields, respectively.

As was the case for the reduction of the wave equation to the frequency domain Helmholtz equation, the reduction of the three-dimensional Helmholtz equation to the one-dimensional, depth-separated wave equation is obtained at the cost of having to evaluate the infinite integrals of the inverse transforms. However, the asymptotic behavior of the integration kernels makes truncation of the integration interval possible, with small or insignificant error as a result, and numerical quadrature schemes are available for accurate evaluation of the truncated inverse transforms. This is described in detail in Chap. 4, where we discuss *wavenumber integration* methods. These methods directly implement the integral transform approach described here and therefore compute the "exact" solution for the range-independent problem. Alternative approximate methods are also available, including the *method of stationary phase* and the *normal mode* expansion. The basic principles of these techniques are described in this chapter, but much more detail on normal modes is given in Chap. 5.

Finally, there is much virtue to the integral transform solution in terms of physical interpretation. As is clear from the form of the inverse transform, (2.87), the integral transform represents a decomposition of the total field into plane waves propagating

with horizontal wavenumber k_x. Similarly, the Hankel transform, (2.94), represents a decomposition into conical waves as is clear from the relation

$$J_0(k_r r) = \frac{1}{2}\left[H_0^{(1)}(k_r r) + H_0^{(2)}(k_r r)\right] \tag{2.97}$$

together with the asymptotic form of the Hankel functions, (2.39) and (2.40).

The solution of the depth-separated wave equation therefore directly yields important interpretational results such as plane-wave reflection and transmission coefficients, with the wavenumber kernels providing information on the relative significance of the various plane-wave components in the total field. This will be illustrated both in this chapter and in Chap. 4 for increasingly complex range-independent environments.

2.4.2 Source in Fluid Halfspace

We will illustrate the basic principles of the integral transform solution by applying it to the case of a point source in a fluid halfspace, treated in Sect. 2.3.4 by means of Green's theorem. The environment, shown in Fig. 2.4, can be considered range-independent or horizontally stratified with just a single interface.

To apply the integral transform, we introduce a cylindrical coordinate system with the z-axis perpendicular to the surface and passing through the source. For the line-source problem, a Cartesian coordinate system should be used, yielding the exact same solution in the wavenumber domain. The field then only depends on the horizontal range and depth. The depth-separated wave equation for this case is, therefore, (2.96) with the medium wavenumber being constant, $k(z) = k$. The solution is given in terms of the depth-dependent Green's function in (2.90), where the Green's function, (2.91), is found as a superposition of the free-field solution to (2.92) and the two independent solutions to the corresponding homogeneous equation.

For a homogeneous medium, the solution to the homogeneous equation is of the form

$$H_\omega(k_r, z) = A^+(k_r)\,\mathrm{e}^{\mathrm{i}k_z z} + A^-(k_r)\,\mathrm{e}^{-\mathrm{i}k_z z} \tag{2.98}$$

with k_z being the vertical wavenumber,

$$k_z = \sqrt{k^2 - k_r^2}. \tag{2.99}$$

Since the inverse Hankel transform must be evaluated over a semi-infinite wavenumber domain, we have to choose a definition for the square root for $k_r > k$. We choose the definition

$$k_z = \begin{cases} \sqrt{k^2 - k_r^2}, & k_r \le k \\ \mathrm{i}\sqrt{k_r^2 - k^2}, & k_r > k. \end{cases} \tag{2.100}$$

With this definition, for $z \to \infty$, the first term in (2.98) corresponds to downward propagating waves for $k_r < k$, and exponentially decaying waves for $k_r > k$. Thus, this term can be eliminated for $z \to -\infty$ due to the radiation condition for all values of k_r. Similarly, the second term can be eliminated for $z \to +\infty$. The radiation conditions at $z \to \pm\infty$ therefore require the homogeneous solutions to be of the form

$$H_\omega(k_r, z) = \begin{cases} A^+(k_r)\, \mathrm{e}^{\mathrm{i}k_z z}, & z \to +\infty \\ A^-(k_r)\, \mathrm{e}^{-\mathrm{i}k_z z}, & z \to -\infty. \end{cases} \tag{2.101}$$

If we had defined the square root in (2.100) using $-\mathrm{i}$ for $k_r > k$, we would have to switch the terms when passing $k_r = k$. Although the present definition is chosen merely for convenience, it is absolutely essential to use the proper definition when we later introduce attenuation.

We next solve the inhomogeneous depth-separated wave equation for the free-field Green's function, (2.92). Except for the source depth $z = z_s$, the Green's function satisfies the homogeneous equation, with solutions of the form given in (2.101). Applying symmetry considerations for the field with respect to the plane $z = z_s$, we therefore have

$$\begin{aligned} g_\omega(k_r, z, z_s) &= A(k_r) \begin{cases} \mathrm{e}^{\mathrm{i}k_z(z-z_s)}, & z \geq z_s \\ \mathrm{e}^{-\mathrm{i}k_z(z-z_s)}, & z \leq z_s \end{cases} \\ &= A(k_r)\, \mathrm{e}^{\mathrm{i}k_z|z-z_s|}. \end{aligned} \tag{2.102}$$

We now integrate (2.96) from $z_s - \epsilon$ to $z_s + \epsilon$ to obtain

$$\left[\frac{dg_\omega(k_r, z)}{\mathrm{d}z}\right]_{z_s-\epsilon}^{z_s+\epsilon} + O(\epsilon) = -\frac{1}{2\pi}. \tag{2.103}$$

Inserting the derivative of (2.102) into (2.103) and letting $\epsilon \to 0$, we get,

$$A(k_r) = -\frac{1}{4\pi \mathrm{i} k_z} \tag{2.104}$$

with the free-field depth-dependent Green's function following as

$$g_\omega(k_r, z, z_s) = -\frac{\mathrm{e}^{\mathrm{i}k_z|z-z_s|}}{4\pi \mathrm{i} k_z}. \tag{2.105}$$

The point-source Green's function in an infinite medium is now obtained as the inverse Hankel transform of (2.105),

$$g_\omega(r, z, z_s) = \frac{i}{4\pi} \int_0^\infty \frac{\mathrm{e}^{\mathrm{i}k_z|z-z_s|}}{k_z}\, J_0(k_r r)\, k_r\, \mathrm{d}k_r, \tag{2.106}$$

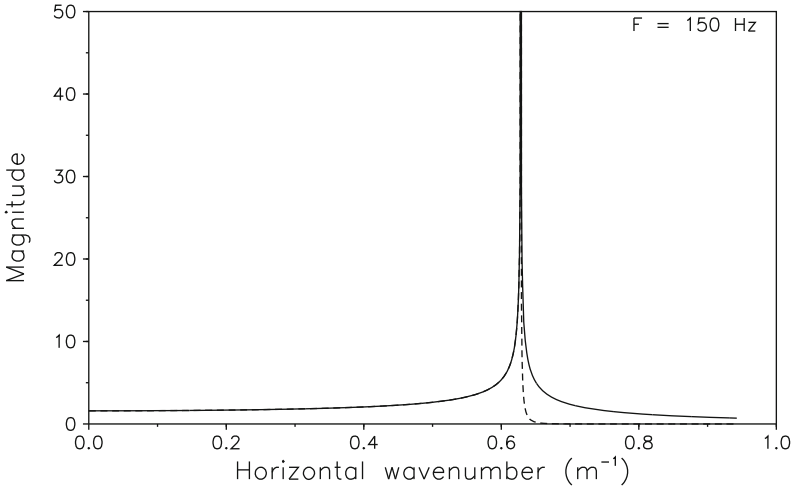

Fig. 2.6 Magnitude of the depth-dependent Green's function for point source in an infinite medium, computed along a complex contour, offset from the real axis by the amount given in (4.115). *Solid curve*: $z - z_s = \lambda/10$. *Dashed curve*: $z - z_s = 2\lambda$

which is the *Sommerfeld–Weyl integral*. This integral decomposes the point-source field into conical waves, propagating cylindrically in the horizontal direction, and propagating like plane waves in the vertical direction for $k_r < k$, and decaying exponentially in the vertical for $k_r > k$.

Before proceeding with the solution of the halfspace problem, we first discuss the basic physical significance of the depth-dependent Green's function for the point source in (2.105). Thus, Fig. 2.6 shows the magnitude of $g_\omega(k_r, z, z_s)$ for receiver depths $0.1\,\lambda$ and $2.0\,\lambda$ below the source. At the medium wavenumber, $k_r = k$, the Green's function has a square root singularity, with the magnitude being independent of the receiver depth for $k_r \leq k$. To avoid this singularity, the kernel is computed along a contour displaced into the complex plane by an amount given by (4.115), usually applied to obtain a numerically stable integration, as will be discussed later in Sect. 4.5.5. This part of the wavenumber spectrum corresponds to waves propagating in the vertical direction due to the purely imaginary argument of the exponential function in (2.105); it is referred to as the *radiating spectrum*. However, for $k_r > k$ the vertical wavenumber k_z is imaginary and the magnitude therefore becomes exponentially decaying with depth. This part of the wavenumber spectrum is called the *evanescent spectrum*.

It is important to stress that the representation of the depth-dependent Green's function in the wavenumber domain is a result of the rather arbitrary mathematical manipulation we have performed through the integral transformation of the Helmholtz equation. We can, therefore, not straightforwardly associate the features of Fig. 2.6 with specific physical wave phenomena. This is particularly evident for this simple problem of a point source in an infinite, homogeneous medium where the field is known to be a spherical wave propagating with the medium wavenumber.

This simple feature is not evident from the form of the depth-dependent Green's function in Fig. 2.6. However, after applying the inverse transform of (2.105) the resulting field will exhibit this behavior.

We can, however, analyze the significance of the two spectral domains by changing the integration variable for the radiating spectrum, which will dominate the solution for $|z - z_s| \to \infty$. As described above, the depth-dependent Green's functions for the point and line sources are identical, and for simplicity we will therefore do this for the line-source case. Introducing the *grazing angle* θ, we have

$$k_x = k \cos\theta, \tag{2.107}$$

$$k_z = k \sin\theta, \tag{2.108}$$

$$\frac{\mathrm{d}k_x}{\mathrm{d}\theta} = -k_z. \tag{2.109}$$

The expression for the frequency-domain Green's function is obtained by applying the inverse Fourier transform, (2.87), to the depth-dependent Green's function. Assuming large depth separation of source and receiver, we include only the radiating spectrum in the integration, i.e.,

$$\begin{aligned} g_\omega(\mathbf{r}, \mathbf{r}') &\simeq \frac{i}{4\pi} \int_{-k}^{k} \frac{\mathrm{e}^{\mathrm{i}k_z|z-z_s|}}{k_z} \mathrm{e}^{\mathrm{i}k_x x} \, \mathrm{d}k_x \\ &= \frac{i}{4\pi} \int_0^{\pi} \mathrm{e}^{\mathrm{i}k\,|z-z_s|\sin\theta + \mathrm{i}kx\cos\theta} \, \mathrm{d}\theta. \end{aligned} \tag{2.110}$$

In this form, the integral clearly represents the field as an integral of equal amplitude *plane waves* propagating at an angle θ relative to the horizontal x-axis. Similarly, for the point source, the inverse Hankel transform represents the field as a superposition of *conical waves*. For small depth separations, the curvature of the cylindrically symmetric field produced by the line source cannot be represented by a superposition of plane waves alone. This curvature is therefore accounted for by the evanescent spectrum $k_x > k$, which is consistent with the exponential decay of this spectrum for increasing receiver depth as indicated in Fig. 2.6.

The evanescent spectrum is, in this case, a mathematical abstraction introduced by the choice of coordinate system, and it does not represent waves that can exist isolated in an infinite medium (for the radiating spectrum, the plane-wave components are real waves). However, this does not imply that the evanescent spectrum can be ignored, and the inverse transform must incorporate this spectrum to correctly represent the curvature of the wavefronts, in particular for small depth separations. Furthermore, for stratifications of media with different wave speeds, a certain value of the horizontal wavenumber k_x may be in the evanescent spectrum in one medium, but in the radiating spectrum in another. In this case, the evanescent spectrum gains physical significance and must be included in the analysis. Finally, for normal modes to exist in an ocean waveguide, the field must be evanescent in the lower halfspace representing the subbottom; otherwise energy would propagate

away from the waveguide. The same is the case for the seismic interface waves described in Chap. 4; they are evanescent both in the water and in the bottom. In conclusion, the *evanescent spectrum* is just as important for a correct representation of the field in stratified media as is the *radiating spectrum*.

Returning to the halfspace problem, we now seek the homogeneous solution, (2.98), which superimposed with the source Green's function, (2.105), satisfies the Fourier transform of the free-surface boundary condition, (2.69), i.e.,

$$\psi(k_r, 0) \equiv 0 \tag{2.111}$$

as well as the radiation condition for $z \to \infty$. The latter immediately removes the second term in (2.98), and we therefore have

$$\begin{aligned} \psi(k_r, 0) &= -S_\omega \left[g_\omega(k_r, 0, z_s) + H_\omega(k_r, 0) \right] \\ &= S_\omega \left[\frac{\mathrm{e}^{\mathrm{i}k_z z_s}}{4\pi \mathrm{i} k_z} - A^+(k_r) \right] = 0, \end{aligned} \tag{2.112}$$

which yields the solution for $A^+(k_r)$. The total field solution now becomes

$$\psi(k_r, z) = S_\omega \left[\frac{\mathrm{e}^{\mathrm{i}k_z |z - z_s|}}{4\pi \mathrm{i} k_z} - \frac{\mathrm{e}^{\mathrm{i}k_z (z + z_s)}}{4\pi \mathrm{i} k_z} \right]. \tag{2.113}$$

The term in the bracket is the depth-dependent Green's function for the halfspace. Since it is a superposition of two free-field depth-dependent Green's functions, see (2.52), it is clear that its inverse transform is a superposition of two spherical wavefields produced by the real source at $z = z_s$ and a virtual source at $z = -z_s$, as obtained earlier in Sect. 2.3.4. The result is a Lloyd-mirror pattern in the field for $z > z_s$ due to the interference of the two fields, and it is very illustrative of the versatility of the wavenumber representation to relate this physical behavior of the total field to the behavior of the depth-dependent Green's function. Thus, Fig. 2.7a shows the magnitude of the halfspace Green's function as a function of the horizontal wavenumber k_r (or k_x for the line source) for a source at depth $z_s = 2.5\,\lambda = 5\pi/k$. The result for receiver depths $z = z_s + 0.1\,\lambda$ and $z = z_s + 2\,\lambda$ are indicated by a solid and a dashed line, respectively. Again the depth-dependence of the *evanescent spectrum* is evident, but the more interesting feature is the oscillating magnitude in the *radiating spectrum*. From (2.113) it is clear that the Green's function vanishes for

$$k_z = \frac{(m-1)\,\pi}{z_s}, \qquad m = 1, 2, \cdots \tag{2.114}$$

and has *maxima* for

$$k_z = \frac{(2m-1)\,\pi}{2 z_s}. \qquad m = 1, 2, \cdots \tag{2.115}$$

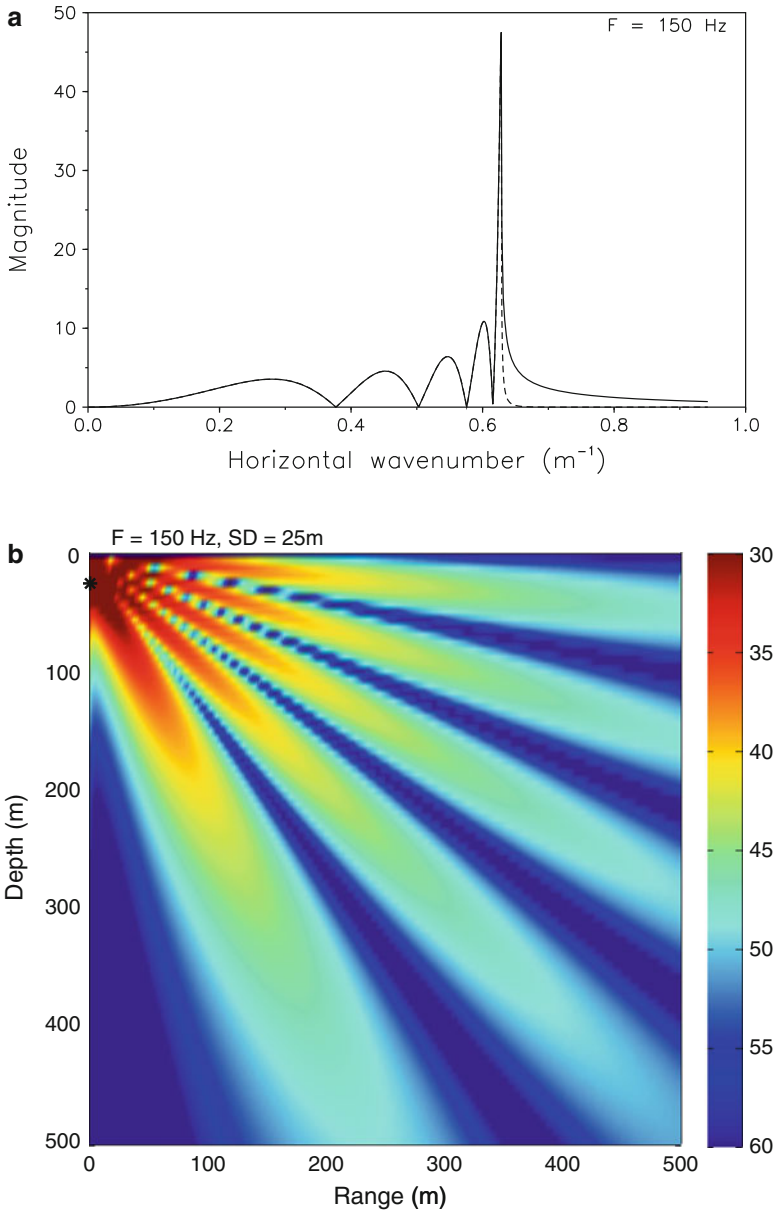

Fig. 2.7 Source in a fluid halfspace. (**a**) Magnitude of the depth-dependent Green's function, computed along a complex contour, offset from the real axis by the amount given in (4.115). *Solid curve*: $z - z_s = \lambda/10$. *Dashed curve*: $z - z_s = 2\lambda$. (**b**) Pressure field contours

Introducing the relation between the wavenumbers and the grazing angle, $k_z = k \sin\theta$, these vertical wavenumbers correspond to the angles $\theta_{\max}$ for the maxima and $\theta_{\min}$ for the minima, where

$$\sin\theta_{\max} = \frac{(2m-1)\,\pi}{2kz_s}, \tag{2.116}$$

$$\sin\theta_{\min} = \frac{(m-1)\,\pi}{kz_s}. \tag{2.117}$$

These angles correspond to the angles for which the Lloyd-mirror pattern has respective maxima and minima, as is evident from Fig. 2.7b, which displays the transmission loss computed from the inverse Fourier transform, (2.87), of the Green's function in Fig. 2.7a. This feature of the field can be directly deduced from the wavenumber spectrum for the Green's function. Note that the amplitudes of the lobes in the Green's functions are inversely proportional to k_z. However, this is again a result of the transform, and if we change the integration variable to grazing angle in the radiating spectrum, the lobes will have equal amplitude – in agreement with the property of the Lloyd-mirror pattern that all lobes are of equal amplitude in the farfield, as can be seen in Fig. 2.7b.

Defining the *reflection coefficient* as the complex ratio between the reflected plane-wave amplitude and the incoming plane-wave amplitude at the surface $z = 0$, it is clear from the form of the solution, (2.113), together with the plane wave decomposition, (2.110), that for all wavenumbers or angles of incidence, the free-surface reflection coefficient is

$$\mathcal{R} = -1. \tag{2.118}$$

2.4.3 Reflection and Transmission

The Lloyd-mirror effect described above is a characteristic feature of the interaction of an acoustic field with a smooth sea surface. However, the interaction with the bottom can be just as important, in particular in shallow water environments. Whereas the atmosphere is well represented by a vacuum, the seabed is an acoustic medium, and the bottom interaction problem has to be treated as a propagation problem in a heterogeneous medium.

The simplest bottom model consists of a fluid halfspace, and we will here analyze the isolated interaction with the bottom by assuming the upper halfspace to be a homogeneous fluid medium representing the water column, Fig. 2.8.

A simple point source of strength S_ω is present in the upper halfspace at depth $z = z_s$. We have here introduced a cylindrical coordinate system with the r-axis along the interface and the z-axis passing through the source. Following the same procedure as in the preceding section, we express the wavenumber kernel for the field in terms of the Green's function satisfying the boundary conditions, (2.90), with $G_\omega(k_r, z, z_s)$ given by (2.91) as a superposition of the free-field Green's function for the source and a homogeneous solution.

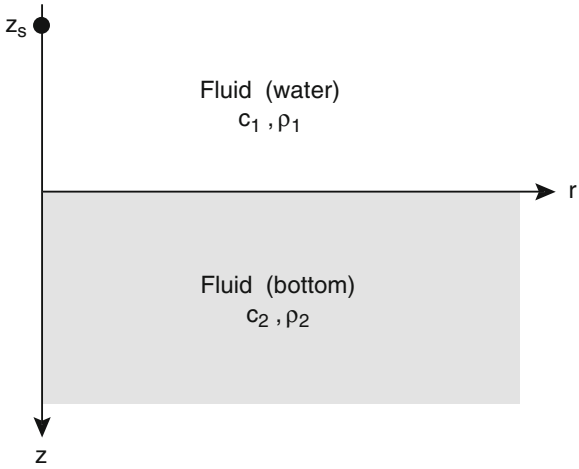

Fig. 2.8 Two fluid halfspaces

Using the radiation condition, the homogeneous solution in the upper halfspace with wavenumber $k_1 = \omega/c_1$ and density ρ_1, is

$$H_{\omega,1}(k_r, z) = A_1^-(k_r)\, \mathrm{e}^{-\mathrm{i}k_{z,1}z} \tag{2.119}$$

and similarly in the lower halfspace with wavenumber $k_2 = \omega/c_2$ and density ρ_2,

$$H_{\omega,2}(k_r, z) = A_2^+(k_r)\, \mathrm{e}^{\mathrm{i}k_{z,2}z}, \tag{2.120}$$

where $k_{z,i}$, $i = 1, 2$, are the vertical wavenumbers for the two media. In the upper halfspace, the free-field Green's function, (2.52), must be added to yield the total Green's function.

The two unknown amplitudes for the homogeneous solutions are now determined from the boundary conditions. The first boundary condition expresses *continuity of vertical displacements*, i.e., in wavenumber space,

$$\frac{\partial \psi_1(k_r, z)}{\partial z} = \frac{\partial \psi_2(k_r, z)}{\partial z}, \qquad z = 0. \tag{2.121}$$

Replacing $\psi(k_r, z)$ by the Green's functions and inserting the two homogeneous solutions and the source Green's function from (2.105), we obtain for $z = 0$,

$$k_{z,2}\, A_2^+(k_r) + k_{z,1}\, A_1^-(k_r) = k_{z,1}\, g_{\omega,1}(k_r, 0, z_s). \tag{2.122}$$

The second boundary condition expresses *continuity of pressure*,

$$\rho_1\, \psi_1(k_r, z) = \rho_2\, \psi_2(k_r, z), \qquad z = 0. \tag{2.123}$$

Again, insertion of the Green's functions in the two media yields for $z = 0$,

$$\rho_2 \, A_2^+ - \rho_1 \, A_1^- = \rho_1 \, g_{\omega,1}(k_r, 0, z_s). \tag{2.124}$$

The solution of (2.122) and (2.124) then leads to,

$$A_1^- = \frac{\rho_2 k_{z,1} - \rho_1 k_{z,2}}{\rho_2 k_{z,1} + \rho_1 k_{z,2}} \, g_{\omega,1}(k_r, 0, z_s), \tag{2.125}$$

$$A_2^+ = \frac{2\rho_1 k_{z,1}}{\rho_2 k_{z,1} + \rho_1 k_{z,2}} \, g_{\omega,1}(k_r, 0, z_s). \tag{2.126}$$

Since the wavenumber representation in a Cartesian coordinate system represents a decomposition into plane-wave solutions, $g_\omega(k_r, 0, z)$ represents the complex amplitude at $z = 0$ of plane waves incident from above, and A_1^- and A_2^+ represent the amplitudes of the reflected and transmitted plane waves, respectively. Therefore, the fractions in (2.125) and (2.126) are directly the *reflection coefficient* $\mathcal{R}$ and *transmission coefficient* $\mathcal{T}$ for the displacement potential,

$$\mathcal{R} = \frac{\rho_2 k_{z,1} - \rho_1 k_{z,2}}{\rho_2 k_{z,1} + \rho_1 k_{z,2}}, \tag{2.127}$$

$$\mathcal{T} = \frac{2\rho_1 k_{z,1}}{\rho_2 k_{z,1} + \rho_1 k_{z,2}}. \tag{2.128}$$

By using (2.108), it is easily verified that these expressions are identical to those derived in Chap. 1 as (1.56) and (1.57).

We here briefly discuss the properties of the reflection and transmission coefficients. The trivial case of identical media, i.e., $k_1 = k_2$, $\rho_1 = \rho_2$, as expected yields $\mathcal{R} \equiv 0$, $\mathcal{T} \equiv 1$. The case of the lower medium being vacuum should obviously yield the free surface reflection coefficient, which is easily verified by letting $k_2 = \omega/c_2 \to \infty$ and $\rho_2 = 0$, yielding $\mathcal{R} \equiv -1$ and $\mathcal{T} \equiv 0$. For other media we distinguish between a *hard bottom*, $c_2 > c_1$ and a *soft bottom*, $c_2 < c_1$. Since the reflection and transmission properties are distinctly different in the two cases, we discuss them separately.

2.4.3.1 Hard Bottom

For the hard bottom, the medium wavenumber in the bottom is smaller than the wavenumber in the water, $k_2 < k_1$. We, therefore, have three different spectral regimes to consider in the horizontal wavenumber space, as shown in Fig. 2.9.

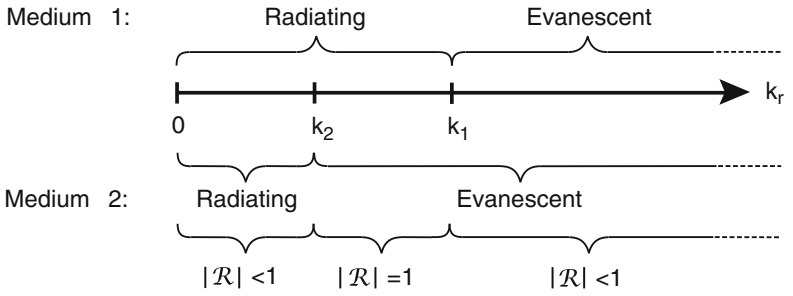

Fig. 2.9 Spectral domains for a hard bottom, $k_2 < k_1$

1. $k_r < k_2$: Waves are *propagating* vertically in both media and energy will be transmitted into the bottom: $|\mathcal{R}| < 1$.
2. $k_2 < k_r < k_1$: Waves are *propagating* in the upper halfspace (water) but are *evanescent* in the lower halfspace (bottom): $|\mathcal{R}| = 1$.
3. $k_1 < k_r$: Waves are *evanescent* in depth in both media: $|\mathcal{R}| < 1$.

This behavior of the reflection coefficient is easily verified by inserting the expressions for the vertical wavenumbers, (2.100), into (2.127). Note that in all three regimes the transmission coefficient will always be non-vanishing, $\mathcal{T} > 0$. This is due to the fact that even in the case of perfect reflection, $k_2 < k_r < k_1$, there will exist a non-vanishing evanescent field in the bottom, a feature which becomes significant for multilayered bottoms as described in Chap. 4. Note that for the simple halfspace problem, the reflection and transmission coefficients are independent of the frequency ω.

The reflection coefficient is often represented in terms of a magnitude and phase as,

$$\mathcal{R}(\theta) = |\mathcal{R}(\theta)|\, \mathrm{e}^{-\mathrm{i}\phi(\theta)}, \tag{2.129}$$

where ϕ is a phase angle and θ is the *grazing angle of incidence*, defined by $\theta = \arccos(k_r/k_1)$. This formulation, of course, only makes sense in the spectral regimes where the field is propagating vertically in the water, i.e., for $k_{z,1}$ real.

Figure 2.10 shows the magnitude and phase of the plane-wave reflection coefficient for the following halfspace parameters: $c_1 = 1500\,\mathrm{m/s}$, $\rho_1 = 1000\,\mathrm{kg/m^3}$ in the water, and $c_2 = 1800\,\mathrm{m/s}$, $\rho_2 = 1800\,\mathrm{kg/m^3}$ in the bottom.

The *critical angle* $\theta_\mathrm{c} = \arccos(k_2/k_1) = 33.5°$ is evident in both the magnitude and the phase, verifying the description of the behavior of the reflection coefficient given above, with perfect reflection ($|\mathcal{R}| = 1$) for $\theta < \theta_\mathrm{c}$ and reflection loss ($|\mathcal{R}| < 1$) for larger grazing angles. Note that in the region of perfect reflection, the phase angle changes from a 180° shift, i.e., $\mathcal{R} = -1$, for $\theta = 0°$ to no phase shift at the critical angle. Above the critical angle there is no phase shift. In other words, for small grazing angles the reflection from a fluid–fluid interface is very similar to the reflection off a free surface, whereas for large grazing angles the reflection is more like the reflection from a rigid halfspace in terms of phase shift, but with reduced magnitude. We discuss these features further in relation to the determination of the acoustic field produced by the point source.

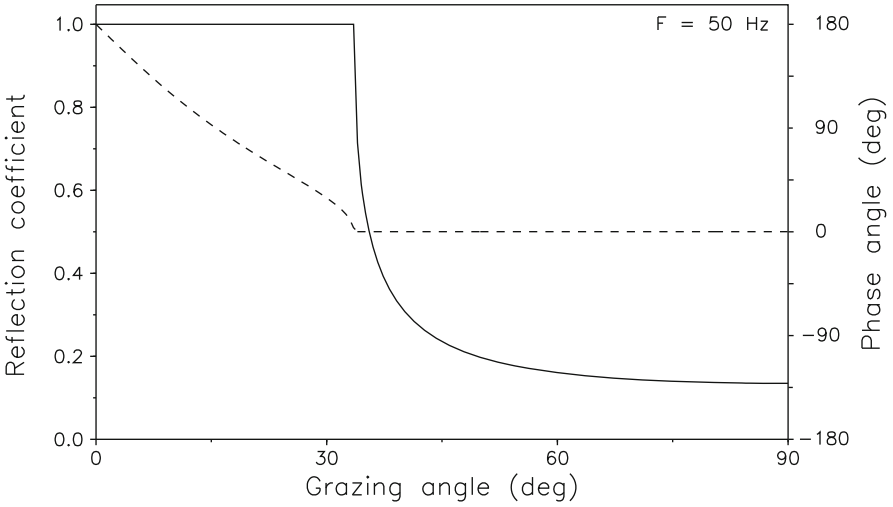

Fig. 2.10 Reflection coefficient as a function of grazing angle for a hard-bottom halfspace. *Solid curve*: Magnitude. *Dashed curve*: Phase

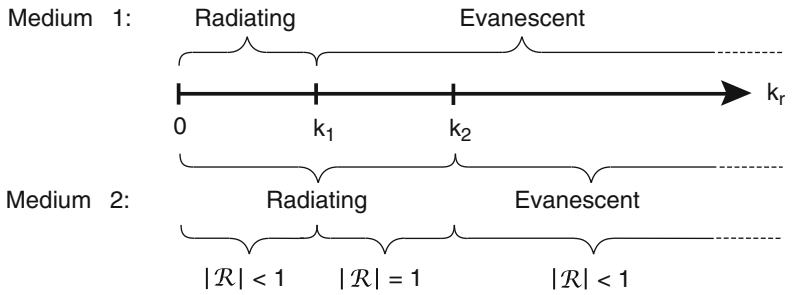

Fig. 2.11 Spectral domains for a soft bottom, $k_1 < k_2$

2.4.3.2 Soft Bottom

A soft bottom is characterized by a speed of sound less than that of water, i.e., $c_2 < c_1$ or $k_2 > k_1$. Again, the wavenumber spectrum is divided into three different regimes, as shown in Fig. 2.11.

1. $k_r < k_1$: Waves are *propagating* vertically in both media and energy will be transmitted into the bottom: $|\mathcal{R}| < 1$.
2. $k_1 < k_r < k_2$: Waves are *evanescent* in the upper halfspace (water) but *propagating* in the lower halfspace (bottom): $|\mathcal{R}| = 1$.
3. $k_2 < k_r$: Waves are *evanescent* in depth in both media: $|\mathcal{R}| < 1$.

Since plane waves propagating in the water have horizontal wavenumbers that satisfy the relation $k_r \leq k_1$, only the first of the above spectral regimes is relevant for plane-wave reflection coefficients.

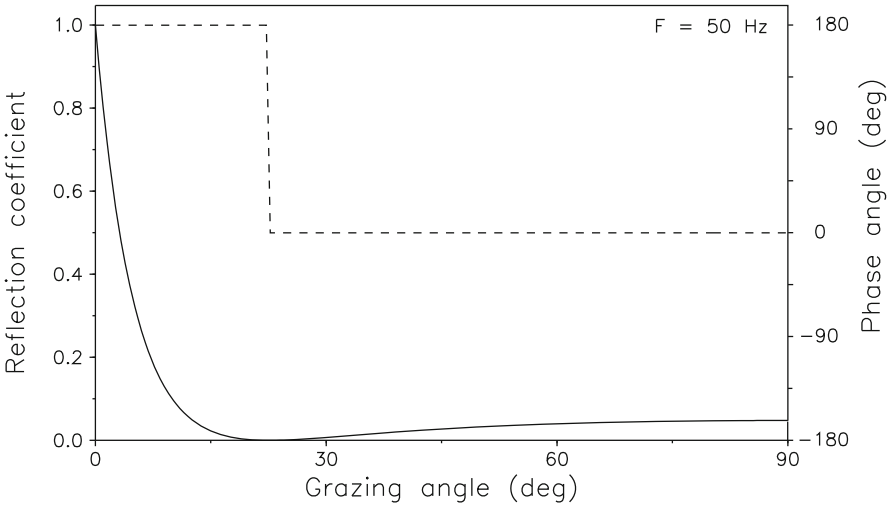

Fig. 2.12 Reflection coefficient as a function of grazing angle for a soft-bottom halfspace. *Solid curve*: Magnitude. *Dashed curve*: Phase

Figure 2.12 shows the magnitude and phase of the plane-wave reflection coefficient for the following halfspace parameters: $c_1 = 1500\,\text{m/s}$, $\rho_1 = 1000\,\text{kg/m}^3$ in the water, and $c_2 = 1300\,\text{m/s}$, $\rho_2 = 1800\,\text{kg/m}^3$ in the bottom. In this case, there is no critical angle and perfect reflection only occurs in the trivial case of zero grazing angle. However, for the above set of parameters there exists an *intromission angle* θ_0 at which the reflection coefficient is zero and all energy is transmitted into the bottom. From (1.60) we find $\theta_0 = 22.6°$, which is seen to coincide with the phase-angle shift of 180° in Fig. 2.12.

The practical application of plane-wave reflection coefficients is rather limited due to the fact that pure plane waves cannot be generated in reality. However, the concept of reflection coefficients is important for a physical understanding of the energy transport in and out of the ocean waveguide, and its application in numerical modeling of ocean acoustics is important for approaches based on plane-wave representations such as the ray approaches described in Chap. 3 and the wavenumber-integration approaches described in Chap. 4. In fact, for classical ray approaches the reflection and transmission coefficients provide the only means of incorporating boundaries into the ocean waveguide.

2.4.3.3 The Point Source Field

To obtain the field produced by a point source at depth $z = z_s$, we use the Hankel transform of the wavenumber kernel,

$$\psi(k_r, z) = \begin{cases} -S_\omega \left[g_{\omega,1}(k_r, z, z_s) + H_{\omega,1}(k_r, z) \right], & z < 0 \\ -S_\omega \, H_{\omega,2}(k_r, z), & z > 0, \end{cases} \tag{2.130}$$

with the homogeneous solution $H_{\omega,1}(k_r, z)$ given by (2.119) and (2.125), and with $H_{\omega,2}(k_r, z)$ given by (2.120) and (2.126). The free-field Green's function $g_{\omega,1}(k_r, z, z_s)$ is given by (2.105).

The total reflected field is now obtained by evaluating the wavenumber integral

$$\begin{aligned}\psi(r,z) &= \int_0^\infty A_1^-(k_r)\, \mathrm{e}^{-\mathrm{i}k_{z,1}z}\, J_0(k_r r)\, k_r\, \mathrm{d}k_r \\ &= \frac{1}{2}\int_{-\infty}^\infty A_1^-(k_r)\, \mathrm{e}^{-\mathrm{i}k_{z,1}z}\, H_0^{(1)}(k_r r)\, k_r\, \mathrm{d}k_r. \end{aligned} \tag{2.131}$$

In general, (2.131) must be evaluated numerically by one of the methods described in Chap. 4. However, an asymptotic evaluation can be obtained by the *method of stationary phase* for receivers in the farfield – see discussion associated with (2.161). Thus, for $k_r r \gg 1$ the Hankel function in (2.131) can be replaced by its large argument asymptotic form, (2.39). Insertion of (2.125), (2.127), (2.129) and (2.105) into (2.131) then yields

$$\psi(r,z) = \frac{S_\omega\, \mathrm{e}^{-\mathrm{i}\pi/4}}{4\pi\sqrt{2\pi r}} \int_{-\infty}^\infty |\mathcal{R}(k_r)|\, \frac{\sqrt{k_r}}{i k_{z,1}}\, \mathrm{e}^{-\mathrm{i}\left[\phi(k_r)+k_{z,1}(z+z_s)-k_r r\right]}\, \mathrm{d}k_r. \tag{2.132}$$

If the receiver is far away from the interface, i.e., $k_{z,1}(z + z_s) \gg 1$, the integral is dominated by the contributions from points where the phase term in the kernel is stationary, i.e.,

$$\frac{\partial}{\partial k_r}\Big[\phi(k_r) + k_{z,1}\,(z + z_s) - k_r r\Big] = 0, \tag{2.133}$$

or

$$\frac{\partial\phi(k_r)}{\partial k_r} - \frac{k_r\,(z + z_s)}{k_{z,1}} - r = 0. \tag{2.134}$$

Thus, for a particular receiver position (r, z), the solutions of (2.134) define the dominant plane-wave components of the field. A geometrical interpretation of this equation is obtained by introducing the grazing angle θ defined by $\cot\theta = k_r/k_{z,1}$,

$$r = \frac{\partial\phi(k_r)}{\partial k_r} - (z + z_s)\cot\theta. \tag{2.135}$$

As illustrated in Fig. 2.13, the solutions of (2.135) represent plane waves or *rays*, hitting the interface at grazing angle θ, and propagating along the interface a distance $\Delta = \partial\phi(k_r)/\partial k_r$ before being launched back toward the receiver, again at an angle θ with respect to the horizontal. It should be noted that the grazing angle θ is related to the horizontal wavenumber k_r through the relation $\cos\theta = k_r/k_1$, with the result that the *ray displacement* Δ is a function of θ. The ray displacement is therefore non-zero only for grazing angles where the phase of the reflection

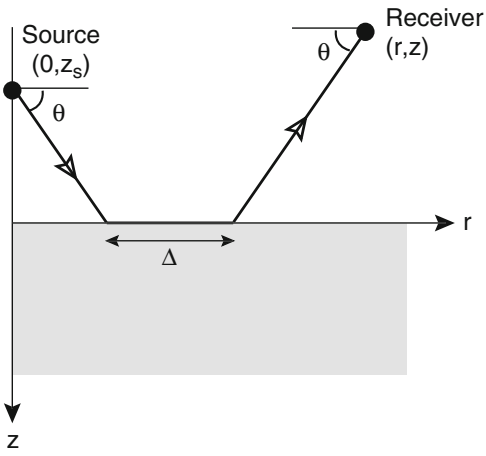

Fig. 2.13 Ray representation of reflection from a homogeneous halfspace

coefficient is varying. For the *hard-bottom* case shown in Fig. 2.10, there are two reflection regimes separated by the critical angle θ_c:

1. $\theta < \theta_c : \Delta = \partial\phi/\partial k_r > 0$,
2. $\theta > \theta_c : \Delta = \partial\phi/\partial k_r = 0$.

Thus, for ranges larger than the *critical range*, $r_c = -(z + z_s)\cot\theta_c$, there will be a non-vanishing ray displacement. For shorter ranges, there is no displacement and rays are reflected specularly. It can be shown that a stationary phase point always exists at the critical angle where the phase curve in Fig. 2.10 has infinite curvature. For ranges larger than critical, a ray path with grazing angle $\theta = \theta_c$ always exists, corresponding to the so-called *head wave*. Similar considerations for the *soft-bottom* case, Fig. 2.12, imply that here there is no ray displacement for any angle of incidence.

The physical explanation for the ray displacement is the existence of a evanescent field, propagating horizontally in the bottom for incident grazing angles smaller than critical, the so-called *lateral wave*. Although the evanescent spectrum is a mathematical abstraction for the infinite homogeneous medium, the ray displacement is an illustration of the fact that for propagation in inhomogeneous media, the evanescent spectrum has *physical significance* as well.

Since the phase of the reflection coefficient for the two-halfspace problem is frequency independent, the ray displacement is inversely proportional to frequency. Ray displacements are therefore usually ignored in high-frequency ray acoustics. However, for low and intermediate frequencies it is important to properly account for the ray displacement at the water–bottom interface. Even in cases where the bottom is ignored, a similar ray displacement must be accounted for at turning points in a refracting ocean. Thus, the $\pi/2$ phase shift introduced at turning points in WKB ray theory (Chap. 3), should be accompanied by the corresponding horizontal ray displacement in order to obtain an accurate representation of the acoustic field. Again, the effect is less significant at high frequencies, where accumulated errors become important only at long ranges.

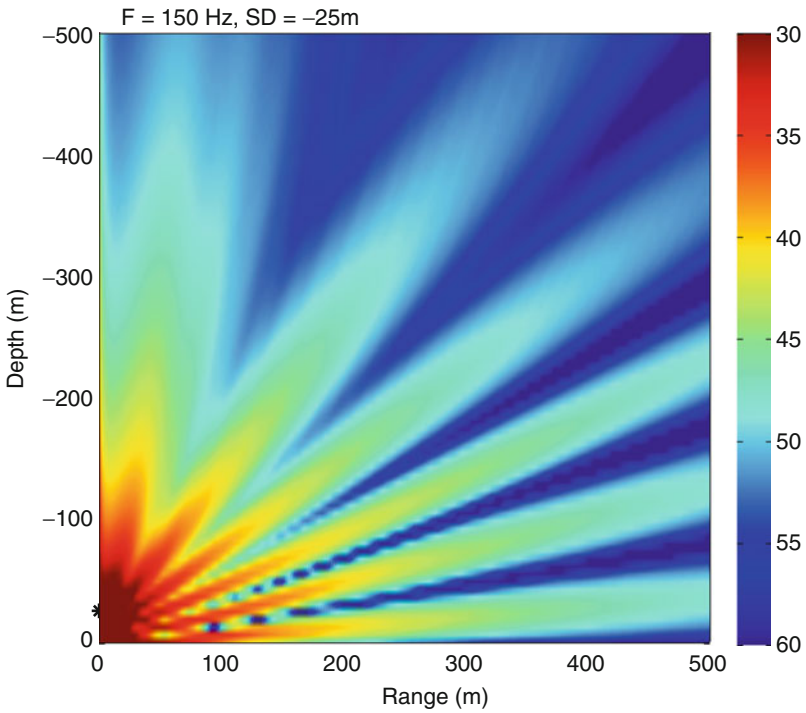

Fig. 2.14 Pressure contours for reflection from a homogeneous halfspace

A numerical evaluation of the wavenumber integral representation for the total field yields the solution shown in Fig. 2.14 in the form of pressure contours in decibels. Comparing to the similar contour plot of the field in a fluid halfspace with a free surface, Fig. 2.7b, we note that for low grazing angles, the interference patterns are very similar, with a vanishing field for grazing angles approaching horizontal. This is because the phase of the reflection coefficient (see Fig. 2.10) approaches 180° for low grazing angles, which is the phase shift introduced also by the free surface. This clearly illustrates that the common assumption of a hard bottom reflecting similarly to an infinitely rigid bottom is a misconception. On the contrary, hard bottoms reflect as a free surface for small grazing angles.

The reflectivity behavior of various bottom types is more clearly illustrated by displaying the angular spectra of the total fields 50 m above the bottom, as shown in Fig. 2.15. As expected, the rigid bottom (dotted curve) has a maximum in the horizontal direction whereas the pressure-release bottom (dashed curve) has vanishing amplitude. The spectrum for the penetrable hard bottom (solid curve) is very similar to that of the pressure-release bottom for small grazing angles. On the other hand, for grazing angles larger than critical (33.5°), the reflectivity of the penetrable bottom is similar to that of the rigid bottom, except for the decrease in amplitude caused by the loss of energy to the transmitted wave.

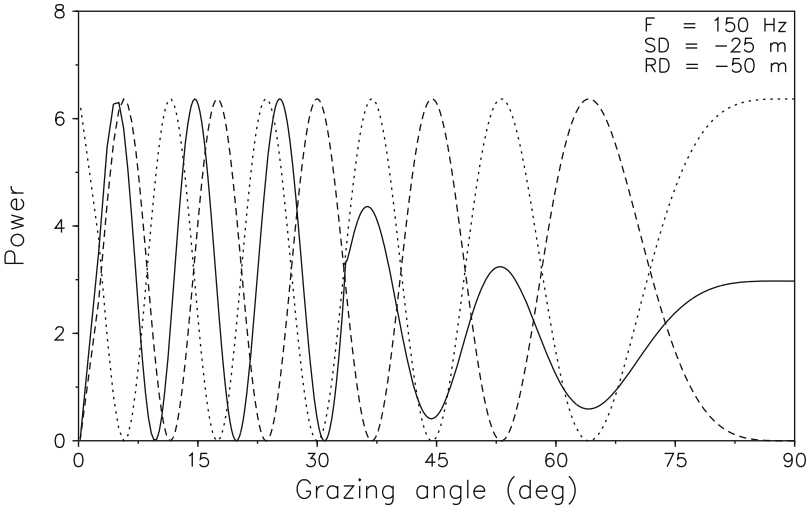

Fig. 2.15 Angular spectrum for reflection from a homogeneous halfspace. *Solid curve*: Penetrable bottom. *Dashed curve*: Pressure release bottom. *Dotted curve*: Rigid bottom

2.4.4 Ideal Fluid Waveguide

Up to this point we have dealt with the sea surface and sea bottom interactions as separate processes. However, the general ocean-acoustic propagation scenario involves interaction with both boundaries.

The simplest model of this ocean waveguide is a range-independent, isovelocity water column with perfectly reflecting boundaries as shown in Fig. 2.16. Both the sea surface and the seafloor are taken to be pressure-release boundaries. As discussed in the previous section, this choice for the seafloor boundary condition is a reasonable approximation, since a penetrable seafloor at low grazing angles reflects similarly to a free surface. Moreover, long-range propagation is dominated by small propagation angles since high-angle energy is rapidly attenuated due to bottom loss.

Although the environmental model in Fig. 2.16 is a strongly over-simplified model of the real ocean, it is well-suited for illustrating some of the basic waveguide phenomena associated with ocean acoustic propagation.

As in the case of the simpler halfspace problems, we can obtain a solution to the waveguide problem using the superposition principle. The field produced by a point source at $(0, z_s)$ in the absence of boundaries is given by

$$\psi(r,z) = -S_\omega \frac{\mathrm{e}^{\mathrm{i}kR}}{4\pi R}. \tag{2.136}$$

Next, we need to add a solution to the homogeneous Helmholtz equation to satisfy the boundary conditions of vanishing pressure at the surface and bottom of the

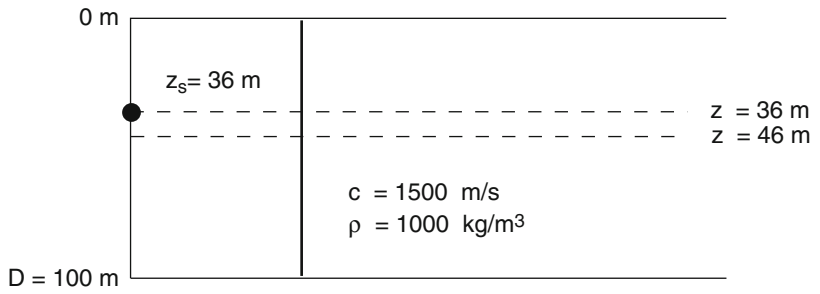

Fig. 2.16 Idealized ocean waveguide model with pressure-release surface and bottom

waveguide. One method is to use the *image* or *mirror* method derived earlier from Green's theorem. However, this method is not easily generalized to more complex environments such as the Pekeris waveguide described in the next section. Alternatively, we use the integral transform technique, which is more general. The *image* method, however, has significant virtue in terms of physical understanding, and we shall therefore describe both solution approaches here.

2.4.4.1 Image Method

As described in Sect. 2.4.2 for the homogeneous fluid halfspace, the image method superimposes the free-field solution with the fields produced by the image sources. In the halfspace case, only a single image source was necessary to satisfy the boundary conditions. In the waveguide problem, sound will be multiply reflected between the two boundaries, requiring an infinite number of image sources to be included. Figure 2.17 shows a schematic representation of the contributions from the physical source at depth z_s and the first three image sources, leading to the first 4 terms in the expression for the total field,

$$\psi(r,z) \simeq -\frac{S_\omega}{4\pi}\left[\frac{e^{ikR_{01}}}{R_{01}} - \frac{e^{ikR_{02}}}{R_{02}} - \frac{e^{ikR_{03}}}{R_{03}} + \frac{e^{ikR_{04}}}{R_{04}}\right], \tag{2.137}$$

where the negative signs correspond to an odd number of reflections and the positive signs correspond to an even number of reflections. The remaining terms are obtained by successive imaging of these sources to yield the *ray expansion* for the total field,

$$\psi(r,z) = -\frac{S_\omega}{4\pi}\sum_{m=0}^{\infty}\left[\frac{e^{ikR_{m1}}}{R_{m1}} - \frac{e^{ikR_{m2}}}{R_{m2}} - \frac{e^{ikR_{m3}}}{R_{m3}} + \frac{e^{ikR_{m4}}}{R_{m4}}\right] \tag{2.138}$$

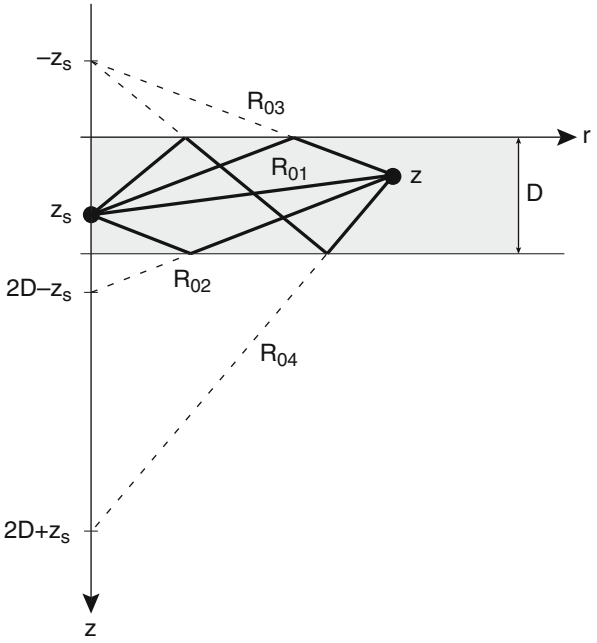

Fig. 2.17 Superposition of free-field solution and first three image source solutions for an ideal waveguide

with

$$
\begin{aligned}
R_{mn} &= \sqrt{r^2 + z_{mn}^2}, \\
z_{m1} &= 2Dm - z_s + z, \\
z_{m2} &= 2D(m+1) - z_s - z, \\
z_{m3} &= 2Dm + z_s + z, \\
z_{m4} &= 2D(m+1) + z_s - z
\end{aligned}
$$

and D being the vertical depth of the duct.

The most important feature of the image approach is the direct association between individual terms in the ray expansion and a particular multiple arrival. However, it should be remembered that it is a steady-state solution, and the individual arrivals may only be identified in the time-domain solution, and here the frequency and bandwidth of the source signal plays an important role. Thus, only short, high frequency pulses can be individually identified as true images of the source signal.

To illustrate this important point, we substitute the time-domain Green's function of (2.55) into the above image solution to get the waveguide impulse response,

$$g_t(r,z) = \frac{1}{4\pi}\sum_{m=0}^{\infty}\left[\frac{\delta(R_{m1}/c-t)}{R_{m1}} - \frac{\delta(R_{m2}/c-t)}{R_{m2}} - \frac{\delta(R_{m3}/c-t)}{R_{m3}} + \frac{\delta(R_{m4}/c-t)}{R_{m4}}\right]. \tag{2.139}$$

The terms in the sum now represent a series of sharp impulses. For example, the first four terms, as per Fig. 2.17, represent direct, bottom bounce, surface bounce and bottom-surface bounce arrivals. One may convolve the results in (2.139) with a source function or filter these results within a specified bandwidth in order to obtain the pulse structure that indicates whether the arrivals are actually separated in time (see Sect. 8.3.1).

At lower frequencies the multiples will interfere in the time domain, and the received field will therefore be a distorted pulse. Here, an interpretation in terms of *normal modes* is more convenient. In general, the advantage of the source image approach and other ray approaches in terms of physical interpretation is most pronounced for high-frequency, transient propagation problems.

2.4.4.2 Integral Transform Solution

Since the ideal waveguide is a simple example of a horizontally stratified medium, we can use the integral transform approach. The total field has the integral representation

$$\psi(r,z) = \int_0^{\infty} \psi(k_r,z)\, J_0(k_r r)\, k_r\, \mathrm{d}k_r \tag{2.140}$$

with the kernel being a superposition of the depth-dependent Green's function and homogeneous solutions to the depth-separated wave equation,

$$\psi(k_r,z) = -S_\omega\Big[g_\omega(k_r,z,z_s) + H_\omega(k_r,z)\Big]. \tag{2.141}$$

The free-field Green's function is given by (2.105) and the homogeneous solution by (2.98),

$$g_\omega(k_r,z,z_s) = -\frac{\mathrm{e}^{\mathrm{i}k_z|z-z_s|}}{4\pi\mathrm{i}k_z}, \tag{2.142}$$

$$H_\omega(k_r,z) = A^+(k_r)\,\mathrm{e}^{\mathrm{i}k_z z} + A^-(k_r)\,\mathrm{e}^{-\mathrm{i}k_z z}. \tag{2.143}$$

The amplitudes of the homogeneous solutions are now determined from the boundary conditions. At both boundaries, $z = 0$ and $z = D$, the pressure must vanish, requiring the displacement potential to vanish as well,

$$A^+(k_r) + A^-(k_r) = \frac{\mathrm{e}^{\mathrm{i}k_z z_s}}{4\pi\mathrm{i}k_z}, \tag{2.144}$$

$$A^+(k_r)\,\mathrm{e}^{\mathrm{i}k_z D} + A^-(k_r)\,\mathrm{e}^{-\mathrm{i}k_z D} = \frac{\mathrm{e}^{\mathrm{i}k_z(D-z_s)}}{4\pi\mathrm{i}k_z}. \tag{2.145}$$

These equations are now solved for the amplitudes $A^{\pm}(k_r)$ of the homogeneous solution and superimposed onto the free-field solution to obtain,

$$\psi(k_r, z) = -\frac{S_\omega}{4\pi} \begin{cases} \dfrac{\sin k_z z \, \sin k_z (D - z_s)}{k_z \, \sin k_z D}, & z < z_s \\ \dfrac{\sin k_z z_s \, \sin k_z (D - z)}{k_z \, \sin k_z D}, & z > z_s. \end{cases} \tag{2.146}$$

This depth-dependent solution has poles for discrete values of the wavenumber given by

$$k_z D = m\pi, \qquad m = 1, 2 \ldots, \tag{2.147}$$

or, in terms of the horizontal wavenumber $k_r = \sqrt{k^2 - k_z^2}$,

$$k_r = \sqrt{k^2 - \left(\frac{m\pi}{D}\right)^2}, \qquad m = 1, 2 \ldots \tag{2.148}$$

Equation (2.148) defines an infinite set of k_r-values, for which the solution has singularities, or poles, some of which may be real and the rest purely imaginary, as indicated in Fig. 2.18. The presence of the poles for real values of k_r is important for the evaluation of the wavenumber integral, (2.140), which by definition is performed along the real wavenumber axis. Using Cauchy's theorem we can deform the contour of integration into the complex plane to avoid the poles. Here, the *radiation condition* at $r \to \infty$ determines whether the contour should pass above or below the poles on the real axis. We first use the relation between the Bessel and

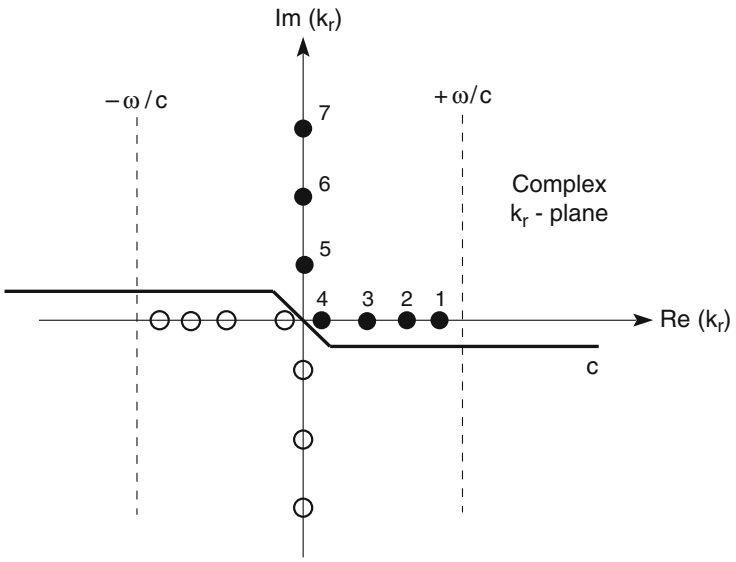

Fig. 2.18 Singularities of the depth-dependent Green's function for an ideal waveguide

Hankel functions to change the integral into one containing only the Hankel function $H_0^{(1)}(k_r r)$ representing outgoing waves at infinity,

$$\psi(r,z) = \frac{1}{2}\int_{-\infty}^{\infty} \psi(k_r,z)\, H_0^{(1)}(k_r r)\, k_r \, \mathrm{d}k_r. \tag{2.149}$$

Due to the asymptotic behavior of the Hankel function, (2.39), we can close the integration contour in the upper imaginary halfplane, replacing the integral by the sum of the residues for the poles enclosed. To satisfy the radiation condition, only poles corresponding to outgoing and decaying waves should be enclosed by the contour. It is easily verified that the poles to be included are those on the positive real and imaginary axes, i.e., the filled circles in Fig. 2.18. Hence, the contour for evaluation of (2.149) should pass above the poles on the negative real axis and below the ones on the positive real axis as shown in Fig. 2.18. In principal, there are three different ways of evaluating the integral:

1. Asymptotic evaluation of the wavenumber integral by the method of stationary phase, which yields an expansion in terms of *eigenrays*, i.e., a series of rays connecting the source and receiver, including all reflected multiples. For the ideal waveguide, the terms in the stationary phase expansion are similar to the terms in (2.138) obtained by the *image method*. However, the stationary phase terms approximate the exact spherical wave representation by farfield plane waves. For horizontally stratified media, the stationary phase evaluation of the wavenumber integral is equivalent to the *ray tracing* approach described in Chap. 3.
2. Direct evaluation of the integral in (2.149) using numerical quadrature. This is the approach taken in the *wavenumber integration* techniques described in Chap. 4. This method is applicable to the present waveguide problem as well as to the earlier reflection and transmission problems.
3. Evaluation of the field as a sum of the residues for the poles enclosed by the integration contour described above. This is basically the approach taken in the *normal mode* methods described in Chap. 5. This method is applicable only to propagation problems which are dominated by the pole contributions.

2.4.4.3 Normal Modes

The wavenumber integration approach is the most general since it is not dependent on the pole contributions being dominant. However, for the ideal waveguide an exact solution is obtained as an infinite sum of residues, and this solution is therefore the most convenient for this problem. In addition, each term in the sum has a distinct physical interpretation, as will be clear shortly. By simple algebra, the sum of the residues is obtained from (2.146) as,

$$\psi(r,z) = -\frac{\mathrm{i}S_\omega}{2D}\sum_{m=1}^{\infty} \sin(k_{zm}z)\sin(k_{zm}z_s)\, H_0^{(1)}(k_{rm}r) \tag{2.150}$$

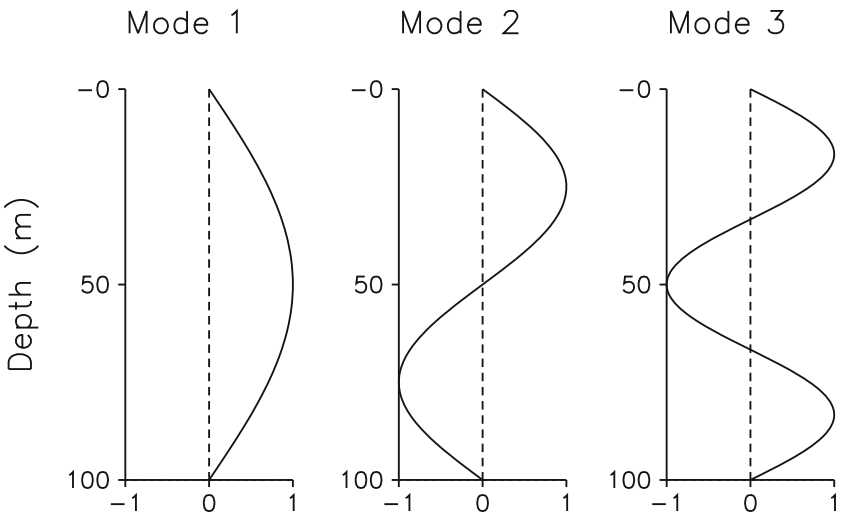

Fig. 2.19 Depth dependence of the first 3 normal modes in ideal waveguide at 20 Hz

with the vertical and horizontal wavenumbers given by (2.147) and (2.148), respectively. Equation (2.150) is the *normal-mode expansion* of the field in the waveguide. Each term in the expansion has a simple trigonometric depth dependence of the form $\sin(k_{zm}z)$, as shown in Fig. 2.19.

In the normal-mode solution, the symmetry between source and receiver is evident. Therefore, if source and receiver are interchanged, the field remains the same, in accordance with the *reciprocity theorem* of linear acoustics. Further, it is clear that the magnitude of a particular mode, the *modal excitation*, is proportional to the amplitude of that particular mode at the source depth.

The horizontal dependence is determined by the horizontal wavenumber k_{rm}. There are naturally two groups of normal modes to be considered. The first group is the one for which k_{rm} is real. It is clear from the asymptotic form of the Hankel function, (2.39), that these modes are propagating horizontally away from the source. Similarly, it is easily verified from (2.39) that the modes with positive imaginary wavenumber are exponentially decaying in range, with a more rapid decay for larger absolute values of the wavenumber. The normal modes are therefore often categorized as follows:

$$\begin{aligned} &\textit{Propagating modes}: \quad k_{rm} \text{ real} && m < \frac{kD}{\pi}, \\ &\textit{Evanescent modes}: \quad k_{rm} \text{ imaginary} && m > \frac{kD}{\pi}. \end{aligned}$$

Here, it is important to emphasize the difference between the *evanescent modes* and the *evanescent spectrum* described earlier. The terms *radiating* and *evanescent* spectra refer to the *depth* behavior of the kernel in the spectral integral, the evaluation of which leads to the spatial representation of the field. In contrast, the modal sum is

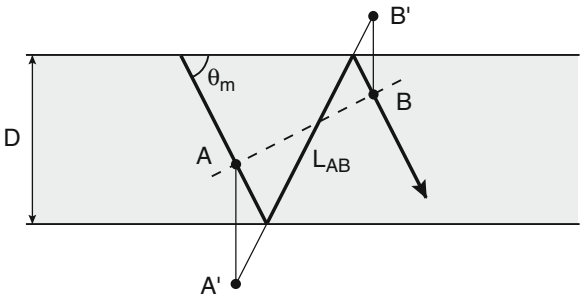

Fig. 2.20 Geometrical interpretation of a normal mode

a result of the spectral integral being evaluated through contour integration, and the modal sum therefore directly represents the spatial distribution of the field, with the terms *propagating* and *evanescent* modes representing the field behavior in *range*. Consequently, there is no direct correspondence between the *evanescent* spectrum and the *evanescent* modes. In fact, since the spectral integral is evaluated along the real wavenumber axis, all the components in the kernel are *propagating* in range.

A normal mode is a superposition of up- and downgoing plane waves of equal amplitude and vertical wavenumber k_{zm}, as is clear from the relation

$$\sin(k_{zm}z) = \frac{\mathrm{e}^{\mathrm{i}k_{zm}z} - \mathrm{e}^{-\mathrm{i}k_{zm}z}}{2\mathrm{i}}. \tag{2.151}$$

Both of these waves are propagating at grazing angles $\theta_m = \arctan(k_{zm}/k_{rm})$, where k_{rm} is the horizontal wavenumber. The ray path of such a plane wave in the waveguide is shown in Fig. 2.20. The dashed line shows the common wavefront for the wave passing through points A and B. The distance traveled between point A and B is

$$L_{\mathrm{AB}} = \frac{2D}{\sin\theta_m} - \frac{2D}{\tan\theta_m}\cos\theta_m = 2D\sin\theta_m. \tag{2.152}$$

Insertion of the relation $\sin\theta_m = k_{zm}/k$ together with (2.147) then yields,

$$L_{\mathrm{AB}} = \frac{2\pi m}{k} = m\lambda, \tag{2.153}$$

where λ is the acoustic wavelength. Therefore, the discrete wavenumbers of the normal modes are those for which the multiple reflections of a plane wave are in phase at any point in the waveguide, which, in turn, gives rise to a resonance. It should be stressed that the ray equivalence of the modes illustrated in Fig. 2.20 is *different* from the ray representation of the *image method* in Fig. 2.17. Therefore, although both expansions in (2.138) and (2.150) provide exact solutions to the ideal waveguide problem, the physical significance of the individual terms is entirely

different. The *ray expansion* is a superposition of the field produced by all image sources, whereas the *modal expansion* is a sum of resonances or *eigenfunctions* for the waveguide.

We have here derived the modal expansion by complex contour integration of the Hankel transform solution. Alternatively, we could have derived the result directly as an eigenfunction expansion as is often done in the numerical models based on the normal mode approach (see Chap. 5). However, the present derivation clearly illustrates the close relationship between the *wavenumber integration* and *normal mode* approaches. Secondly, the present approach directly yields the individual modal amplitudes in (2.150), whereas the eigenfunction expansion approach must use the orthogonality relation of the modes to determine the modal amplitudes. Finally, since the wavenumber integral provides an exact solution, the derivation by contour integration directly provides an indication of the approximations made when applying normal mode approaches to non-perfect waveguides where the modal expansion is not exact. This will be demonstrated in the next section dealing with the classical Pekeris waveguide problem.

2.4.4.4 Modal Dispersion

The number of propagating modes in a waveguide is dependent on frequency. Thus, it is clear from (2.148) that for $kD < \pi$, or $\omega < \pi c/D$, no propagating modes exist. On the other hand, at high frequencies there are many propagating modes. In addition, the modal wavenumbers relate to frequency in a nonlinear way, with the waveguide displaying strongly frequency-dependent propagation characteristics. The frequency dependence or *dispersion* of the normal modes is determined by inserting the definition of the medium wavenumber, $k = \omega/c$, into (2.148) and solving for ω,

$$\omega = c\sqrt{k_{rm}^2 + \left(\frac{m\pi}{D}\right)^2}. \tag{2.154}$$

This frequency–wavenumber relation for the modes is evident from Fig. 2.21, showing the so-called $f - k$ diagram in the form of contours of the depth-dependent Green's function for source and receiver at depths 14 and 86 m, respectively, in a 100-m deep ideal waveguide. The hatched area indicates the spectral domain, bounded by the line $f = \omega/2\pi = ck_r/2\pi$, where the field is evanescent. Equation (2.154) shows that mode number m only has real horizontal wavenumbers for frequencies above the *cutoff frequency* f_{0m} given by

$$f_{0m} = \frac{\omega_{0m}}{2\pi} = \frac{mc}{2D}, \tag{2.155}$$

which for the present environmental model (Fig. 2.16) translates into $f_{0m} = m \times 7.5$ Hz. These modal cutoff frequencies are evident also in Fig. 2.21 as regularly spaced high-intensity peaks along the frequency axis. At high frequencies, all modes asymptotically approach a propagation wavenumber which is equal to the medium wavenumber, $k_{rm} \to k = \omega/c$.

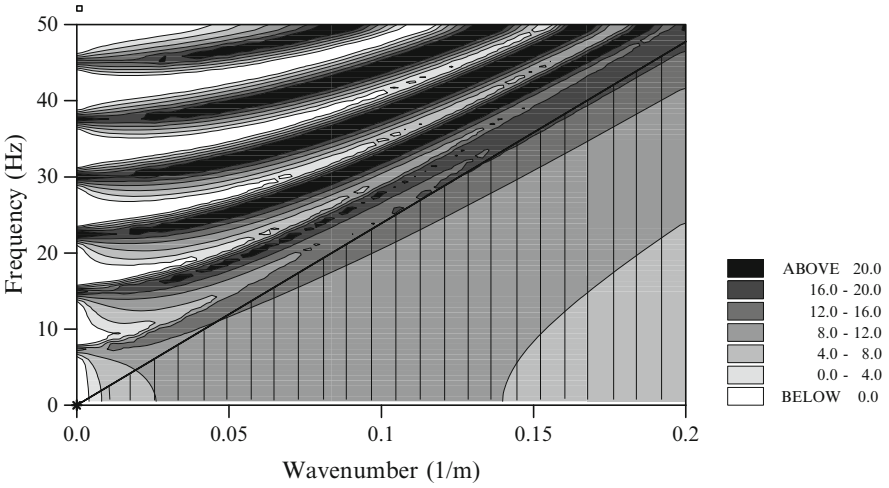

Fig. 2.21 $f - k$ diagram for a pressure-release waveguide of 100-m depth showing peaks corresponding to the first 6 propagating modes

The horizontal *phase velocity* of a mode is defined as

$$v_m = \frac{\omega}{k_{rm}}. \tag{2.156}$$

It is clear from Fig. 2.21 that the phase velocity is always larger than the medium velocity c, although it approaches c for increasing frequency. The phase velocity represents the horizontal velocity of a particular phase in the plane-wave representation of a mode, and it does not represent the speed of energy transport, which obviously must be less than or equal to the speed of sound. Thus, for steep propagation angles, the phase velocity approaches infinity, whereas horizontal propagation yields a phase velocity equal to the speed of sound. This, in turn, means that the plane waves interfering to produce a mode propagate nearly vertically when approaching the cutoff frequency, whereas the modal plane waves in the high-frequency limit propagate close to the horizontal.

To determine the energy transport velocity or *group velocity* of a particular mode, we need to transform the solution into the time domain since the concept of time has no meaning in the frequency domain. Assuming that we have a narrow-band source, the time dependence of the signal carried by mode number m is given by the inverse Fourier transform,

$$\psi(t) = \int_{\omega-\epsilon}^{\omega+\epsilon} \psi(\omega)\, \mathrm{e}^{-\mathrm{i}[\omega t - k_{rm}(\omega)\, r]}\, \mathrm{d}\omega. \tag{2.157}$$

For a small time increment dt the signal will propagate horizontally a distance $\mathrm{d}r = u_m\, \mathrm{d}t$. The phase change of each component in the integral is therefore ω

$\mathrm{d}t - k_{rm}(\omega)\,\mathrm{d}r$. For the signal to be unchanged over the time interval $\mathrm{d}t$ all components of the integral must stay in phase. This requires $\mathrm{d}\omega\,\mathrm{d}t - \mathrm{d}k_{rm}(\omega)\,\mathrm{d}r = 0$, or

$$u_m = \frac{\mathrm{d}r}{\mathrm{d}t} = \frac{\mathrm{d}\omega}{\mathrm{d}k_{rm}}. \tag{2.158}$$

Therefore, the signal carried by mode m will propagate with the horizontal speed u_m, which is the *group velocity*. It is found as the slope of the dispersion curves in Fig. 2.21.

Actually, for future reference, the group velocity can be obtained by the method of stationary phase analogous to the mathematical arguments used to introduce (2.134). Assuming the typical case that $\psi(\omega)$ is a slowly changing function with respect to one oscillation of $f(\omega) \equiv \omega t - k_{rm}(\omega)r$ in (2.157), most of the contributions to the integral will cancel out except in the non-oscillating neighborhood for those values of ω for which $f(\omega)$ is stationary. Then, for

$$\begin{aligned} \omega &= \omega_0 + \epsilon, \\ f'(\omega_0) = 0 \quad &\rightarrow \quad \frac{r}{t} = \frac{\mathrm{d}\omega(k_{rm})}{\mathrm{d}k_{rm}} \equiv u_{rm}, \end{aligned} \tag{2.159}$$

we can write the phase of the exponential as

$$f(\omega) = f(\omega_0) + \frac{\epsilon^2}{2} f''(\omega_0) + \cdots. \tag{2.160}$$

The limits of the integral in (2.157) can be extended to $\pm\infty$ since the only contribution is from around ω_0; using (2.160), (2.157) becomes

$$\begin{aligned} \psi(t) &= \psi(\omega_0)\mathrm{e}^{-\mathrm{i}[\omega_0 t - k_{rm}(\omega_0)\,r]} \int_{-\infty}^{\infty} \mathrm{e}^{-(\mathrm{i}/2)\epsilon^2 f''(\omega_0)}\mathrm{d}\epsilon \\ &= \frac{\sqrt{\pi}\,\psi(\omega_0)}{\left|\frac{1}{2} f''(\omega_0)\right|^{1/2}} \mathrm{e}^{-\mathrm{i}[\omega_0 t - k_{rm}(\omega_0)\,r \pm \pi/4]}, \end{aligned} \tag{2.161}$$

where $f''(\omega_0)$ is evaluated from its definition and the $\pm$ refers to whether $f''(\omega_0)$ is negative or positive, respectively. The packet is now represented by a wave traveling at the group speed since the exponential above represents a wave satisfying the condition $f'(\omega_0)$ as per (2.159). That is, since $x/t = u_{rm}$, a particular value of (ω, k) found at (x_1, t_1) will be found at other space–time locations such that $x_1/t_1 = x_2/t_2$. Thus, we say that the energy associated with a particular frequency group will travel at the group speed u_{rm}.

The phase and group velocities versus frequency for the first 3 modes in the ideal waveguide are shown in Fig. 2.22. As required, the group velocity is always less than the speed of sound (1500 m/s), although approaching it at high frequencies. This is consistent with the above observation that at high frequencies the normal

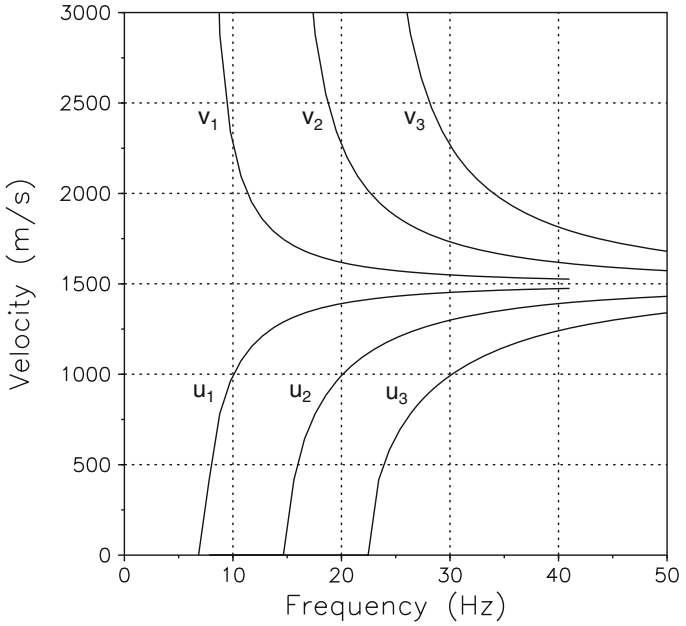

Fig. 2.22 Frequency dependence of phase and group velocities for the first 3 propagating modes in an ideal waveguide

modes are produced by interference of plane waves propagating almost horizontally. Similarly, when approaching cutoff, the plane waves propagate more vertically, and consequently the group velocity approaches zero.

2.4.4.5 The Waveguide Field

When two or more modes are propagating through the waveguide they will interfere. To illustrate this, consider two modes with horizontal wavenumbers k_{rm} and k_{rn} and amplitudes $A_m(z)$ and $A_n(z)$, propagating far away from the source. Using (2.150) together with the asymptotic expression for the Hankel function, (2.39), the field of time dependence $\exp(-\mathrm{i}\omega t)$ is then found to have a range-dependent amplitude at depth z given by

$$\begin{aligned} |\psi(r,z)| &\simeq r^{-1/2}\left|A_m\,\mathrm{e}^{\mathrm{i}k_{rm}r}+A_n\,\mathrm{e}^{\mathrm{i}k_{rn}r}\right| \\ &= r^{-1/2}\sqrt{A_m^2+A_n^2+2A_mA_n\cos\left[r\,(k_{rm}-k_{rn})\right]}. \end{aligned} \tag{2.162}$$

In addition to the cylindrical spreading loss $r^{-1/2}$, the amplitude will oscillate with the period

$$L=\frac{2\pi}{k_{rm}-k_{rn}}, \tag{2.163}$$

which is the *modal interference length*. The magnitude of the oscillations depends on the amplitudes of the two modes at depth z. Thus, if the two amplitudes are equal ($A_m = A_n$), then the amplitude of the total field will vanish at ranges separated by the interference length L. If the amplitudes are different, the field never vanishes, but it shows an oscillatory pattern in range. Since the depth dependence is different for the two modes, also the modal interference pattern is depth dependent.

To illustrate the modal interference, we compute the field produced by a 20-Hz point source in a 100-m deep isospeed (1500 m/s) ocean environment with pressure-release surface and bottom. At 20 Hz, the number of propagating modes M is determined from the inequality

$$M < \frac{kD}{\pi} = \frac{2fD}{c} = 2.6667. \tag{2.164}$$

Therefore, two propagating modes will exist at 20 Hz, with the shapes given in Fig. 2.19. By placing the source at 36 m depth the two modes will be almost equally excited.

Figure 2.23a displays the magnitude of the depth-dependent solution, (2.146), versus horizontal wavenumber along a complex contour passing slightly below the real wavenumber axis as shown in Fig. 2.18. The solid curve shows the magnitude at depth 36 m, i.e., the same depth as the source, and the dashed curve shows the magnitude at 46 m depth. The two peaks correspond to the two modes of this problem, mode 1 with a wavenumber of $0.076\,\mathrm{m}^{-1}$, and mode 2 with a wavenumber of $0.055\,\mathrm{m}^{-1}$. At 36 m depth the modes are of almost equal amplitude, whereas mode 1 dominates at 46 m depths. The modal interference length is found from (2.163) to be $L \simeq 300$ m, which is confirmed by the plot of the transmission loss versus range for the two depths, shown in Fig. 2.23b. Here, the change in interference strength with depth is evident as well.

Mode 1 is symmetric and mode 2 antisymmetric with respect to mid-depth as seen in Fig. 2.19. Therefore, the minima and maxima in the modal interference pattern will switch range position in the lower part of the waveguide. This is shown explicitly in Fig. 2.24, which displays transmission loss contours versus depth and range.

It should be emphasized that the solutions shown here are steady-state solutions of time dependence $\exp(-\mathrm{i}\omega t)$, which means an unlimited duration of the source signal. For time-limited signals – even narrow-band CW signals – the different group velocities will separate the modes in the time domain at long ranges, as discussed in detail in Chap. 8. At a point in the waveguide where the steady-state solution predicts a vanishing field, the received field may consist of two identical CW pulses separated in time by $\Delta t = \pi(1 + 2\ell)/\omega$, with ℓ being an integer, yielding a vanishing Fourier component at frequency ω. This illustrates that care must be taken when analyzing experimental data of limited time duration with steady-state modeling techniques.

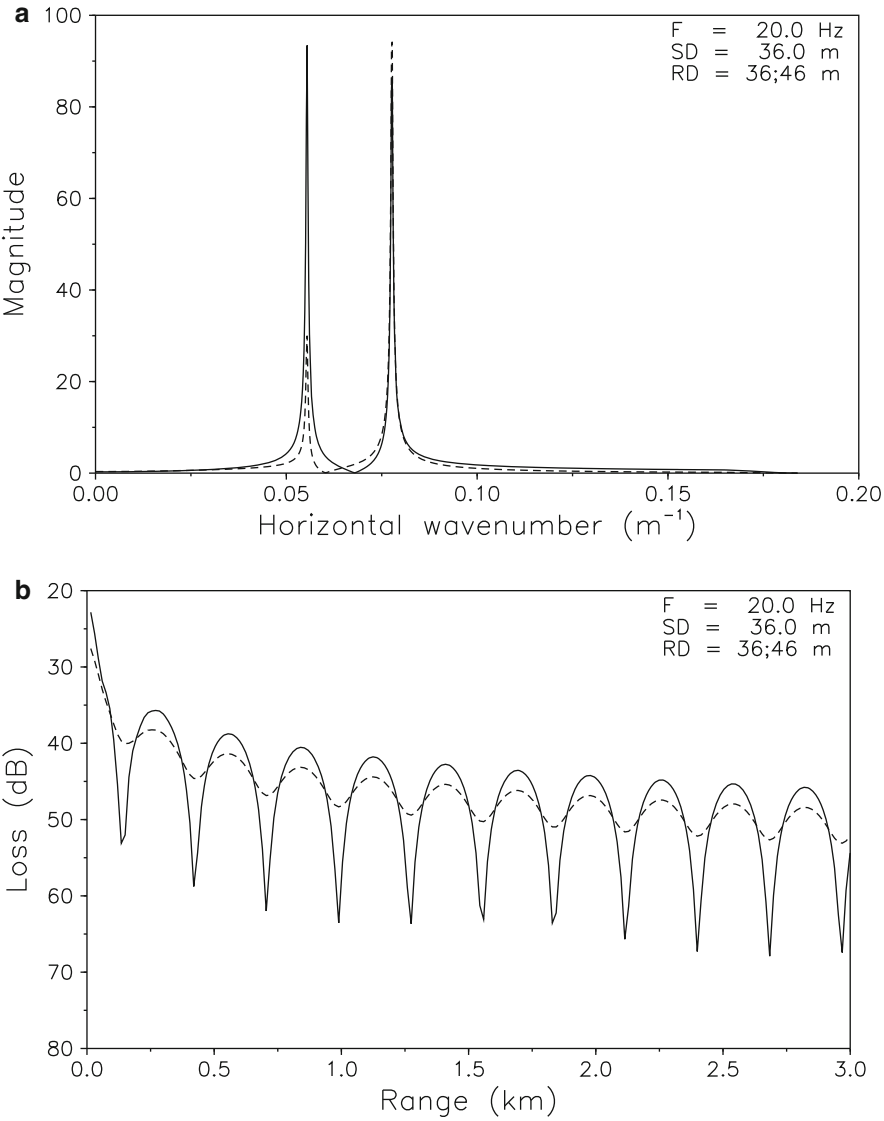

Fig. 2.23 Acoustic field in an ideal waveguide of *thickness* 100 m for 20 Hz point source at 36 m depth. (**a**) Magnitude of the depth-dependent Green's function. (**b**) Transmission loss. *Solid curve*: Receiver depth 36 m. *Dashed curve*: Receiver depth 46 m

2.4.4.6 Relationship Between Image and Modal Solutions

It is of interest to examine the relationship between the image solution and the modal solution [8]. Intuitively, it is clear, for example, that the Lloyd mirror field is easily described by using very few images whereas the field very far away from the

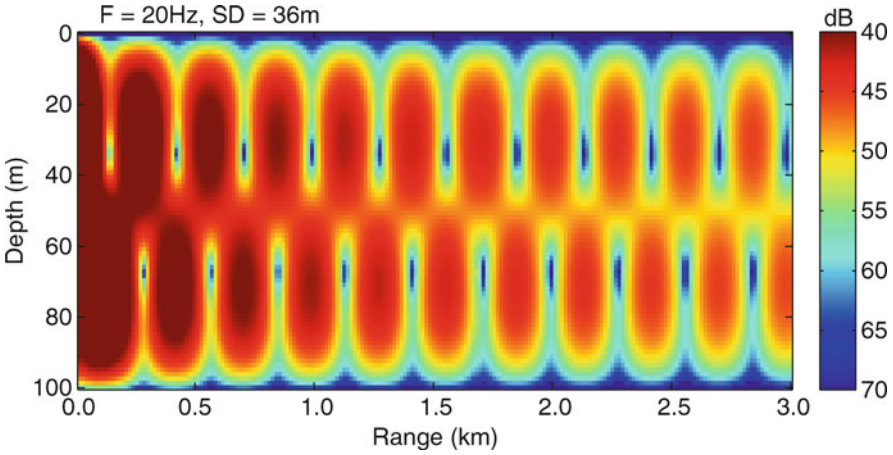

Fig. 2.24 Contours of transmission loss vs. depth and range for 20 Hz point source at 36 m depth in an ideal waveguide of *thickness* 100 m

source in a waveguide would require a very large number of images as per (2.205). On the other hand, the description of the field near the source would require including the continuous spectrum, which, from Fig. 2.29a, we see involves a larger portion of the total wavenumber interval than the discrete part. This latter consideration implies that we must include a large sum of wavenumber components (that can be approximated by a large number of discrete modes of a much thicker waveguide). On the other hand, this near-field case can be treated by only a few images representing a direct path and a few bounces off either boundary with subsequent image contributions diminishing because higher angles have higher loss.

The above tradeoffs between images and modes leads us to the idea that the number of images and modal components have an inverse relationship similar to Fourier conjugate variables (e.g., the larger the relevant frequency interval, the shorter the pulse or time-domain interval). For simplicity, we seek the relationship between modal and image solutions of the ideal waveguide and therefore start with (2.150),

$$\psi = -\frac{\mathrm{i}S_\omega}{4D}\sum_{n=1}^{\infty}\sin(k_{zn}z)\sin(k_{zn}z_s)\,H_0^{(1)}(k_{rn}r), \tag{2.165}$$

where $k_{zn} = n\pi/D \equiv 2n\pi/d$ with the latter definition of $d \equiv 2D$ being made for future convenience. Next, we employ the Poisson sum formula [12] (p. 483),

$$\sum_{m=-\infty}^{\infty} f(dm) = \frac{\sqrt{2\pi}}{d}\sum_{n=-\infty}^{\infty} F\left(\frac{2\pi}{d}n\right), \tag{2.166}$$

where we also use the Fourier transform convention in [12] ,

$$F(x) = \frac{1}{\sqrt{2\pi}}\int_{-\infty}^{\infty} f(y)\,\mathrm{e}^{\mathrm{i}xy}\mathrm{d}y. \tag{2.167}$$

We, therefore, will be substituting (2.150) for F, which is even in n with the $n = 0$ term vanishing, and where k_{rn} is given by (2.147) and (2.148). Therefore, each term is proportional to

$$\begin{aligned} F &= -\frac{\mathrm{i}S_\omega}{4D}\sin(k_{zn}z)\sin(k_{zn}z_s)\,H_0^{(1)}(k_{rn}r) \\ &= -\frac{\mathrm{i}S_\omega}{8D}\left\{\cos\left[k_{zn}(z-z_s)\right]-\cos\left[k_{zn}(z+z_s)\right]\right\}H_0^{(1)}(k_{rn}r). \end{aligned} \tag{2.168}$$

For the Poisson formula, these terms are all of the form

$$F_x = \pm\frac{\mathrm{i}S_\omega}{8D}\cos\left[k_{zn}(z\pm z_s)\right]\,H_0^{(1)}(k_{rn}r) \equiv \pm\frac{\mathrm{i}S_\omega}{4d}\cos(a_\pm x)H_0^{(1)}\left(r\sqrt{k^2-x^2}\right), \tag{2.169}$$

where $x \equiv 2n\pi/d$, $d = 2D$, and $a_\pm = (z \pm z_s)$ and the $\pm$'s operations are realized together. The Poisson sum formula requires the Fourier transform over the even function $F(x)$ and further, that it vanishes for $n, x = 0$. Therefore, we only require the cosine transform of F and the sum starting from $n = 1$. We can therefore rewrite the expression for the Poisson sum in the convenient form,

$$\frac{1}{2}f(0) + \sum_{m=1}^{\infty} f(dm) = \frac{\sqrt{2\pi}}{d}\sum_{n=1}^{\infty}\left[\frac{-\mathrm{i}S_\omega}{4\sqrt{2\pi}}\hat{F}\left(\frac{2\pi}{d}n\right)\right], \tag{2.170}$$

where we now can use cosine transforms and where,

$$\hat{F} = \cos(a_+x)H_0^{(1)}(r\sqrt{k^2-x^2}) - \cos(a_-x)H_0^{(1)}\left(r\sqrt{k^2-x^2}\right). \tag{2.171}$$

We then have for terms of the form $f_\pm = f_+ - f_-$,

$$\begin{aligned} f_\pm(y) &= \pm\sqrt{\frac{2}{\pi}}\frac{\mathrm{i}S_\omega}{4\sqrt{2\pi}}\int_0^\infty \cos(xy)\cos(a_\pm x)H_0^{(1)}\left(r\sqrt{k^2-x^2}\right)\mathrm{d}x \\ &= \frac{-\mathrm{i}S_\omega}{4\pi}\int_0^\infty\left\{\cos\left[x(y+a_\pm)\right]+\cos\left[x(y-a_\pm)\right]\right\}H_0^{(1)}\left(r\sqrt{k^2-x^2}\right)\mathrm{d}x \\ &\equiv \pm\frac{S_\omega}{4\pi}\left[f(y+a_\pm)+f(y-a_\pm)\right], \end{aligned} \tag{2.172}$$

where $y = \mathrm{d}m = 2Dm$. The integrals in all the terms can be evaluated using

$$\int_0^\infty \cos(xy)H_0^{(1)}(r\sqrt{k^2-x^2})\,\mathrm{d}x = -\frac{\mathrm{i}\mathrm{e}^{\mathrm{i}kR}}{R}, \quad R = \sqrt{r^2+y^2}, \tag{2.173}$$

so that four terms are represented by,

$$f_{\pm}(y \pm a_{\pm}) = \pm \frac{-S_{\omega}}{4\pi} \frac{\mathrm{e}^{\mathrm{i}kR_{\pm a}}}{R_{\pm a}}, \quad R_{\pm a} = \sqrt{r^2 + (y \pm a_{\pm})^2}, \tag{2.174}$$

where we note that, for a given m, we have

$$R_{\pm a} = \begin{cases} \sqrt{r^2 + (2mD + z + z_s)^2}, \\ \sqrt{r^2 + (2mD + z - z_s)^2}, \\ \sqrt{r^2 + (2mD - z_s - z)^2}, \\ \sqrt{r^2 + (2mD - z + z_s)^2}. \end{cases} \tag{2.175}$$

We can rearrange the ordering of the *lhs* of (2.170) to be precisely equivalent to (2.138) since the quantities in the parentheses are a renumbered representation of the image depths listed below (2.138). For example, in (2.175) there are only two distinct terms for $m = 0$ corresponding to $\sqrt{r^2 + (z \pm z_s)^2}$, which, by our convention are associated with $\pm$ signs in front of each $f_{\pm}$ term (note the factor $\frac{1}{2}$ on the *lhs* of (2.170). These two terms precisely correspond to the first and third terms of (2.138) for $m = 0$. The second and fourth terms of $m = 0$ terms in (2.138) correspond to the third and fourth terms of $m = 1$ in (2.175). Using all the $m = 0$ and the third and fourth $m = 1$ terms of (2.170) we therefore obtain the four $m = 0$ terms in (2.138). Subsequent terms in this equation are obtained from the Poisson sum by similarly combining appropriate $m, m + 1$ terms.

We have here shown that the modal sum is equivalent to the image sum and that they are Fourier transforms of each other in which the indices are the corresponding Fourier conjugate independent variables. It is important to note that in this isovelocity ideal waveguide, the image solution can be thought of as a ray representation of the total field that propagates from a point source. This is not at all the same as the geometrical interpretation or ray–mode analogy as depicted in Fig. 2.20. The latter refers to a homogeneous (source independent) solution of the waveguide whereas an image or mode solution corresponds to a particular solution for a specific source.

2.4.5 *The Pekeris Waveguide*

For the next level of complexity in modeling the ocean acoustic environment, we introduce the *Pekeris waveguide* shown in Fig. 2.25 [3]. Here, the bottom is more realistically represented by an infinite fluid halfspace, allowing for energy to be transmitted across the water–bottom interface and thereby introducing an additional loss mechanism to the waveguide propagation. As above, it is assumed that surface

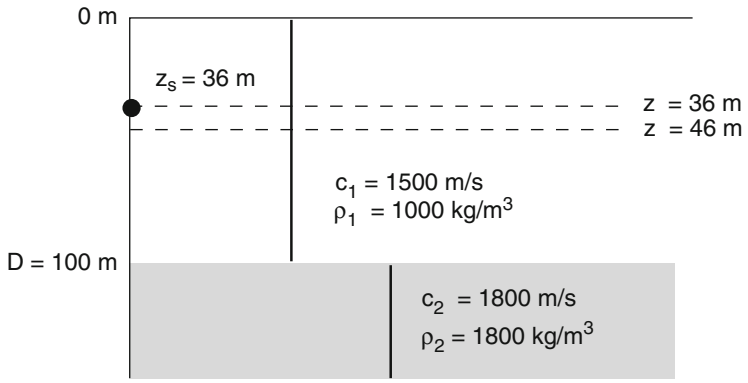

Fig. 2.25 Pekeris waveguide with pressure-release surface and penetrable fluid bottom

and bottom are plane and parallel such that we can use the integral transform solution technique. The sound speeds are denoted c_1 and c_2 for the water and bottom, respectively, and the corresponding densities are ρ_1 and ρ_2.

The source of strength S_ω and time dependence $\exp(-i\omega t)$ is assumed to be at depth z_s in the water column. Therefore, the kernel of the Hankel transform is,

$$\psi_1(k_r, z) = S_\omega \frac{\mathrm{e}^{\mathrm{i}k_{z,1}|z-z_s|}}{4\pi \mathrm{i}k_{z,1}} + A_1^+(k_r)\,\mathrm{e}^{\mathrm{i}k_{z,1}z} + A_1^-(k_r)\,\mathrm{e}^{-\mathrm{i}k_{z,1}z} \tag{2.176}$$

with $k_{z,1} = (k_1^2 - k_r^2)^{1/2}$, where $k_1 = \omega/c_1$ is the water wavenumber at frequency ω. In the bottom the upward propagating component must vanish due to the boundary condition at infinity, yielding

$$\psi_2(k_r, z) = A_2^+(k_r)\,\mathrm{e}^{\mathrm{i}k_{z,2}(z-D)}, \tag{2.177}$$

where the vertical wavenumber must be defined as follows in order to satisfy the radiation condition for $z \to \infty$,

$$k_{z,2} = \begin{cases} \sqrt{k_2^2 - k_r^2}, & |k_r| < k_2 \\ i\sqrt{k_r^2 - k_2^2}, & |k_r| > k_2, \end{cases} \tag{2.178}$$

with $k_2 = \omega/c_2$. We now have three unknown amplitudes of the homogeneous solutions to be determined from the boundary conditions.

The first boundary condition is that of *vanishing pressure* at the sea surface, requiring

$$A_1^+(k_r) + A_1^-(k_r) = S_\omega \frac{i\,\mathrm{e}^{\mathrm{i}k_{z,1}z_s}}{4\pi k_{z,1}}. \tag{2.179}$$

The remaining two boundary conditions are related to the field at the water–bottom interface. They are identical to the boundary conditions used to determine the plane-wave reflection coefficient, i.e., continuity of particle displacement, (2.122), and pressure, (2.124), across the interface. We obtain for continuity of *bottom particle displacement*,

$$k_{z,1}\,\mathrm{e}^{\mathrm{i}k_{z,1}D}\,A_1^+(k_r) - k_{z,1}\,\mathrm{e}^{-\mathrm{i}k_{z,1}D}\,A_1^-(k_r) - k_{z,2}\,A_2^+(k_r) = k_{z,1}\,S_\omega\,\frac{\mathrm{i}\mathrm{e}^{\mathrm{i}k_{z,1}(D-z_s)}}{4\pi k_{z,1}} \tag{2.180}$$

and for continuity of *bottom pressure*,

$$\rho_1\,\mathrm{e}^{\mathrm{i}k_{z,1}D}\,A_1^+(k_r) + \rho_1\,\mathrm{e}^{-\mathrm{i}k_{z,1}D}\,A_1^-(k_r) - \rho_2\,A_2^+(k_r) = \rho_1 S_\omega\,\frac{i\,\mathrm{e}^{\mathrm{i}k_{z,1}(D-z_s)}}{4\pi k_{z,1}}. \tag{2.181}$$

Equations (2.179), (2.180) and (2.181) combine into the following matrix equation for the amplitudes of the homogeneous solutions,

$$\begin{bmatrix} 1 & 1 & 0 \\ k_{z,1}\,\mathrm{e}^{\mathrm{i}k_{z,1}D} & -k_{z,1}\,\mathrm{e}^{-\mathrm{i}k_{z,1}D} & -k_{z,2} \\ \rho_1\,\mathrm{e}^{\mathrm{i}k_{z,1}D} & \rho_1\,\mathrm{e}^{-\mathrm{i}k_{z,1}D} & -\rho_2 \end{bmatrix} \begin{Bmatrix} A_1^+ \\ A_1^- \\ A_2^+ \end{Bmatrix} = \frac{\mathrm{i}S_\omega}{4\pi k_{z,1}} \begin{Bmatrix} \mathrm{e}^{\mathrm{i}k_{z,1}z_s} \\ k_{z,1}\,\mathrm{e}^{\mathrm{i}k_{z,1}(D-z_s)} \\ \rho_1\,\mathrm{e}^{\mathrm{i}k_{z,1}(D-z_s)} \end{Bmatrix}. \tag{2.182}$$

This system of equations with only three unknowns can obviously be solved analytically to yield a closed-form expression for the integration kernel in (2.176). However, in the general multi-layered case the number of equations scales approximately linearly with the number of layers, and the solution will have to be performed numerically, using one of the approaches described later in Chap. 4. On the other hand, the simplicity of the system of equations in (2.182) is convenient for demonstrating the non-triviality of obtaining stable numerical solutions.

Thus, if the coefficients in (2.182) are coded up directly, and the system is solved using a standard equation solver, numerical instability will occur in the evanescent regime $|k_r| > k_1$ where the exponentials in the first and second column become exponentially growing and decaying, respectively. Once the difference in order of magnitude between the columns exceeds the arithmetic precision of the computer (15 digits in double precision), the system of equations becomes ill-conditioned because the two equations involving the exponentials become linearly dependent numerically. The solution to this numerical stability problem will be discussed extensively in Chap. 4, but is easily demonstrated for this simple example. Thus, unconditional stability is achieved by factoring out the growing exponential $\mathrm{e}^{\mathrm{i}k_{z,1}D}$ from the first column, instead including it in the unknown complex amplitude $A_1^+(k_r)$. This is achieved simply by using the seabed instead of the sea surface

as arbitrary origin for the exponential function representing the "upgoing" wave in (2.176),

$$\psi_1(k_r, z) = S_\omega \frac{\mathrm{e}^{\mathrm{i}k_{z,1}|z-z_s|}}{4\pi \mathrm{i}k_{z,1}} + A_1^+(k_r)\,\mathrm{e}^{-\mathrm{i}k_{z,1}(D-z)} + A_1^-(k_r)\,\mathrm{e}^{-\mathrm{i}k_{z,1}z}, \quad 0 \le z \le D. \tag{2.183}$$

Repeating the procedure above, the reader can easily verify that this kernel representation leads to a system of equation of the form

$$\begin{bmatrix} \mathrm{e}^{-\mathrm{i}k_{z,1}D} & 1 & 0 \\ k_{z,1} & -k_{z,1}\,\mathrm{e}^{-\mathrm{i}k_{z,1}D} & -k_{z,2} \\ \rho_1 & \rho_1\,\mathrm{e}^{-\mathrm{i}k_{z,1}D} & -\rho_2 \end{bmatrix} \begin{Bmatrix} A_1^+ \\ A_1^- \\ A_2^+ \end{Bmatrix} = \frac{\mathrm{i}S_\omega}{4\pi k_{z,1}} \begin{Bmatrix} \mathrm{e}^{\mathrm{i}k_{z,1}z_s} \\ k_{z,1}\,\mathrm{e}^{\mathrm{i}k_{z,1}(D-z_s)} \\ \rho_1\,\mathrm{e}^{\mathrm{i}k_{z,1}(D-z_s)} \end{Bmatrix}, \tag{2.184}$$

where all terms with growing exponentials have been eliminated, resulting in a well-conditioned system which can be solved using a standard linear equation solver. It should be noted, though, that the solver, if based on Gaussian elimination, must apply pivoting to maintain stability if this system is applied directly in the above form (upper left coefficient will approach zero for large k_r). As will be discussed in Chap. 4, even this tool can be avoided, simply by choosing a different ordering of the unknowns, here interchanging the up- and downgoing terms in (2.183). The use of proper origins for the exponentials, and a specific ordering of the unknowns are the basic ingredients of the Direct Global Matrix method described in Sect. 4.3.1. This procedure ensures unconditional stability at absolutely no computational cost, even in the general multilayered case.

2.4.5.1 Normal Modes

The solution of (2.182) has poles for values of the horizontal wavenumber where the determinant of the coefficient matrix vanishes. The determinant is

$$\det(k_r) = -2\mathrm{i}\left[\rho_1 k_{z,2}\sin(k_{z,1}D) + \mathrm{i}\rho_2 k_{z,1}\cos(k_{z,1}D)\right] \tag{2.185}$$

leading to the following *characteristic equation* for the poles of the depth-dependent solution in the Pekeris waveguide,

$$\tan(k_{z,1}D) = -\frac{\mathrm{i}\rho_2 k_{z,1}}{\rho_1 k_{z,2}}. \tag{2.186}$$

Like the case for the ideal waveguide, the solutions to (2.186) for which k_r is real correspond to *normal modes* propagating without loss (other than geometrical spreading loss). It is easily shown that (2.186) has solutions with real k_r only in the interval

$$|k_2| < |k_r| < |k_1|. \tag{2.187}$$

Therefore, no modes exist with real propagation wavenumbers less than $k_2 = \omega/c_2$. There is a simple physical explanation for this. For the small wavenumbers, the grazing angle of the plane waves constituting a mode would be above critical, with the field in the bottom being propagating in the vertical direction and therefore leaking energy out of the duct and into the bottom. A lossless mode can therefore not exist at these wavenumbers. Equation (2.186) may still have complex roots corresponding to modes decaying in amplitude with range. These solutions are called *leaky* or *virtual modes*.

As for the ideal waveguide, the inverse Hankel transform, (2.149), must be evaluated along the real wavenumber axis, passing below the poles on the positive axis and above the poles on the negative axis. Again, we can either evaluate the integral along such a contour, which is the *wavenumber integration* approach, or we can evaluate the integral by contour integration, closing the contour in the upper imaginary halfplane, the *normal mode* approach.

Here, however, the contour integration is not as simple as in the ideal waveguide case. This is due to the multi-valuedness of the square root function in the complex plane. Thus, for a complex variable $z = \eta\, \mathrm{e}^{\mathrm{i}(\theta+2\pi n)}$ we have

$$\sqrt{z} = \sqrt{\eta}\, \mathrm{e}^{\mathrm{i}(\theta/2+n\pi)} = \pm\sqrt{\eta}\, \mathrm{e}^{\mathrm{i}\theta/2}, \qquad 0 \le \theta < 2\pi. \tag{2.188}$$

When choosing a particular definition – or *Riemann sheet* – for the square root as in (2.178), a discontinuity is introduced for the argument $\theta = [0, 2\pi]$, defining a *branch cut* for the square root. In (2.188) the branch cut was chosen to be along the real positive axis for the argument z, i.e., $\theta = [0, 2\pi]$, but any value of θ could be chosen for the branch cut. Depending on the form of the integration kernel, this discontinuity of the square root may introduce a discontinuity in the kernel. The closing of the integration contour requires that the integration kernel be analytic, and the contour must therefore not cross any discontinuities of the kernel. It is essential in the contour integration approach that the kernel discontinuities introduced by the branch cuts for the square root be properly defined.

The kernel for the total field is obtained by adding the free-field source contribution to the solutions of (2.182). Here, it turns out that the kernel is continuous at branch cuts for the vertical wavenumber $k_{z,1}$, but discontinuous at branch cuts for $k_{z,2}$. It is a general characteristic of integral transform solutions for layered problems that branch cuts exist for the upper and lower halfspaces, but never for the intermediate layers. This is clear from the form of the homogeneous solution, where a change of sign in the vertical wavenumber just switches the two terms, whereas a change of sign in the halfspace wavenumbers obviously affects the solution due to the fact that one term has been removed through the radiation condition.

The branch cuts for $k_{z,2}$ must originate at the points $k_r = \pm k_2$, but can otherwise be chosen arbitrarily as long as they do not cross the real wavenumber axis along which the original integral is to be evaluated. A convenient choice is the EJP branch cut, named after Ewing, Jardetzky and Press [4], shown in Fig. 2.26. It is defined such that the vertical wavenumber $k_{z,2} = (k_2^2 - k_r^2)^{1/2}$ is real along the branch cut, which covers the interval $[-k_2, k_2]$ on the real k_r axis and the entire imaginary

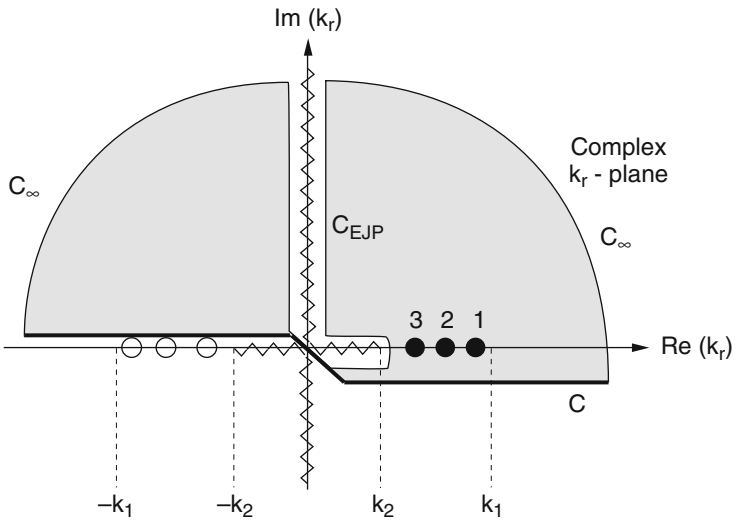

Fig. 2.26 Complex wavenumber plane with EJP branch cut, poles and integration contour

axis. The EJP branch cut has the feature of yielding physically meaningful solutions in the bottom for all complex values of the wavenumber. Furthermore, it can be shown that no poles exist except for the ones on the real axis. With the choice of the vertical wavenumber definition given in (2.178), the Hankel transform, (2.149), must be evaluated along a contour passing below the branch cut on the positive real axis and above the branch cut on the negative real axis, as shown in Fig. 2.26.

We can now close the integration contour in the upper halfplane, replacing the original integral along the real axis with a sum of residues corresponding to the normal modes with real propagation wavenumbers, and a *branch line integral* along a contour C enclosing the *branch point* $k_r = k_2$. The branch line integral represents the contributions from spectral components radiating into the bottom $(0 < k_r < k_2)$, and from spectral components being evanescent in range. Therefore, the significance of the branch line integral diminishes with increasing range. The normal-mode approaches described in Chap. 5 often neglect the branch line contribution, thus yielding solutions which are not valid at short ranges.

The approximate modal solution for the Pekeris waveguide is similar in form to the modal sum for the ideal waveguide, (2.150), and given by

$$\psi(r,z) \simeq -\frac{\mathrm{i}S_\omega}{2D}\sum_{m=1}^{M} a_m(k_{rm})\sin(k_{zm}z)\sin(k_{zm}z_s)\,H_0^{(1)}(k_{rm}r), \qquad (2.189)$$

where the modal wavenumbers k_{rm} are now solutions of the transcendental equation (2.186). The modal excitation is denoted $a_m(k_{rm})$, while k_{zm} is the vertical wavenumber in the water for mode m, $k_{zm} = k_{z,1} = (k_1^2 - k_{rm}^2)^{1/2}$. As shown in Chap. 5, the modal excitation $a_m(k_{rm})$ is a function of frequency.

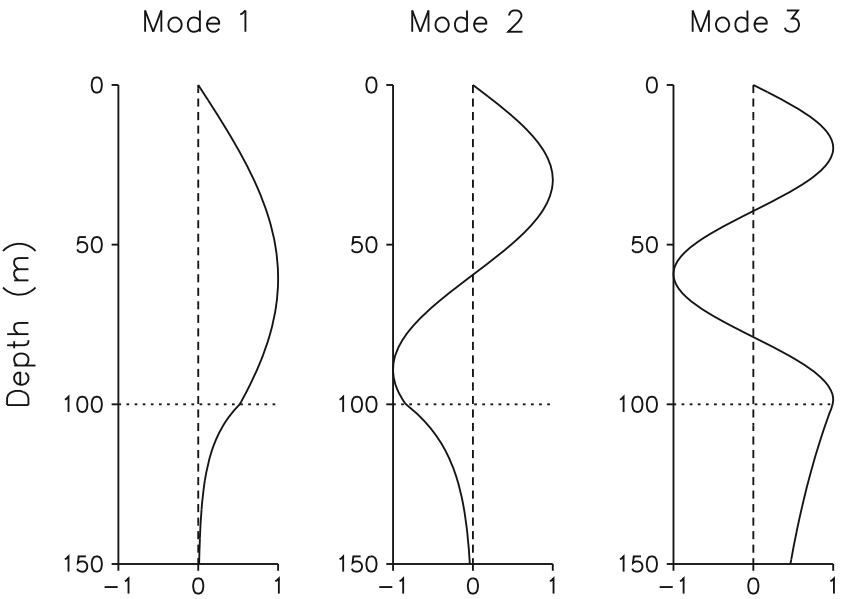

Fig. 2.27 Depth dependence of acoustic pressure for the 3 normal modes in the Pekeris waveguide at 35 Hz

Each mode has a non-vanishing field in the bottom of the form given in (2.177), i.e., exponentially decaying in depth for $k_{rm} > k_2$. This is illustrated in Fig. 2.27 where the modal shapes at 35 Hz are shown in both the water column and the bottom for the environment given in Fig. 2.25. Note that the higher modes have smaller absolute values of the vertical wavenumber in the bottom and hence a longer evanescent tail. As explained earlier, the lower-order modes are very similar in shape to those of the ideal pressure-release waveguide, with a low amplitude near the bottom. On the other hand, the higher-order modes approach the shape expected for the ideal waveguide with a rigid bottom, for which the boundary condition is $\partial\psi/\partial z = 0$, leading to a high mode amplitude near the bottom.

2.4.5.2 Modal Dispersion

The modal expansion in (2.189) is truncated to the M modes with real propagation wavenumbers. As was the case for the ideal waveguide, M increases with increasing frequency. When the frequency is lowered, the propagation wavenumber of a particular mode decreases according to the modal *dispersion* defined by the characteristic equation (2.186). When the modal wavenumber reaches the limit $k_{rm} = k_2$, the associated pole leaves the real axis, and although this complex mode still influences the field, it is said to be cut off. The radial cutoff frequency ω_{0m} for mode

m is determined from (2.186) by inserting $k_{rm} = k_2 = \omega_{0m}/c_2$, i.e., $k_{z,2} = 0$, yielding

$$k_{zm} D = \omega_{0m} D \sqrt{c_1^{-2} - c_2^{-2}} = \frac{\pi}{2} + (m-1)\,\pi, \qquad m = 1, 2, \cdots, \tag{2.190}$$

which leads to the following expression for the cutoff frequency for mode number m,

$$f_{0m} = \frac{\omega_{0m}}{2\pi} = \frac{(m-0.5)\,c_1 c_2}{2D\sqrt{c_2^2 - c_1^2}}. \qquad m = 1, 2, \cdots \tag{2.191}$$

For increasing frequency, the wavenumber for a given mode approaches the water wavenumber k_1 corresponding to horizontally propagating plane waves. The characteristic equation yields,

$$k_{zm} D \to m\pi \qquad \text{for} \qquad \omega \to \infty, \tag{2.192}$$

which is exactly the characteristic equation for the ideal waveguide. Therefore, as frequency increases, the modes of the Pekeris waveguide become more and more similar to those of the ideal waveguide described earlier. This asymptotic behavior of the modal dispersion is evident from Fig. 2.28a showing the $f - k$ diagram in the form of contours of the depth-dependent Green's function for source and receiver at 14 and 86 m depth, respectively. The triangle in the lower right part of the figure bounded by the line $f = \omega/2\pi = c_1 k_r/2\pi$, represents the spectral regime where the field is evanescent in the water column. On the other hand, the triangle in the upper left part bounded by the line $f = \omega/2\pi = c_2 k_r/2\pi$, represents the *continuous spectrum* where the field is radiating into the bottom. Therefore, the relatively narrow, hatched part of the diagram represents the *discrete spectrum*. It is clear from Fig. 2.28a that for the Pekeris waveguide the cut off of the normal modes is a gradual process, with the modes having significant amplitudes well into the continuous spectrum. The continuous spectrum can, therefore, contribute significantly to the acoustic field as will be illustrated by an example in the next section.

Figure 2.28b displays the phase and group velocities for the first 3 modes versus frequency, as determined by the expressions $v_m = \omega/k_{rm}$ and $u_m = d\omega/dk_{rm}$, respectively. At high frequencies the phase and group velocities both approach the water sound speed (1500 m/s), whereas at cutoff, both velocities approach the bottom sound speed (1800 m/s). While the phase velocity is monotonically decreasing with frequency, the group velocity has a minimum at a certain frequency, which in time-domain solutions give rise to the so-called *Airy phase* forming the tail of a transient modal arrival.

If, instead of the EJP branch cut, we choose the one used by Pekeris [3], poles will appear for complex wavenumbers close to the real and imaginary axes corresponding to *leaky* or *virtual modes*. Although this branch cut does not totally eliminate the branch line contribution, the inclusion of the virtual modes close to the real axis provides a better approximation to the full solution than that obtained by excluding the EJP branch line contribution. This will be discussed in more detail in Chap. 5.

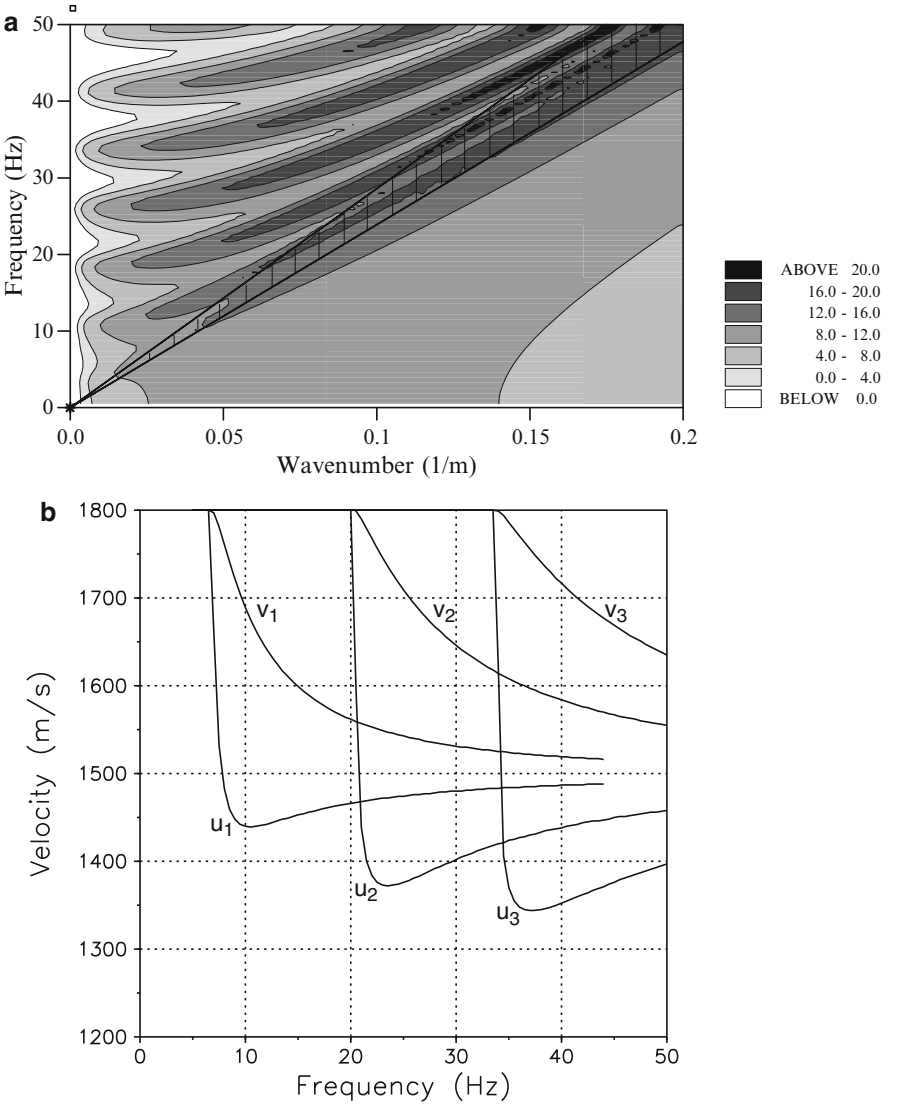

Fig. 2.28 Dispersion of modes in the Pekeris waveguide. (**a**) $f-k$ diagram in the form of contours of the depth-dependent Green's function. (**b**) Phase and group velocities vs. frequency for the first 3 modes

2.4.5.3 The Waveguide Field

The presence of the branch line contribution makes the *modal* solution approximate, and we will therefore proceed with the *wavenumber integration* approach. It is

clear from Fig. 2.26 that the positive wavenumber axis is divided into three different spectral domains:

- $0 < k_r < k_2$: The *continuous spectrum* where waves are radiating into the bottom, thus leaking energy away from the waveguide. Consequently, no lossless modes can exist in this spectral domain. On the other hand this part of the spectrum reflects the presence of leaky modes.
- $k_2 < k_r < k_1$: The *discrete spectrum* where the field is propagating vertically in the water and is exponentially decaying in the bottom. This part of the spectrum contains the discrete poles corresponding to lossless modes.
- $k_1 < k_r$: The *evanescent spectrum* where wave components in both water and bottom are exponentially decaying in the vertical. For the Pekeris waveguide no poles exist in this domain. However, for elastic bottoms the seismic interface waves pertain to this spectral domain.

To illustrate the significance of the different spectral domains, we consider a numerical example for the Pekeris waveguide given in Fig. 2.25. Except for the penetrable bottom with sound speed $c_2 = 1800\,\text{m/s}$ and density $\rho_2 = 1800\,\text{kg/m}^3$, all other parameters are identical to those considered earlier for the ideal pressure-release waveguide.

Figure 2.29a shows the Hankel transform kernel along the same contour used in Fig. 2.23a for the ideal waveguide. The solid curve shows the kernel for a receiver depth of 36 m and the dashed curve for a receiver depth of 46 m. The different spectral regimes are separated by vertical dotted lines at $k_r = k_1,\ k_2$. There is one sharp peak in the discrete spectrum corresponding to the first propagating mode. The second peak at $k_r = 0.068\,\text{m}^{-1}$ is part of the continuous spectrum, indicating the presence of a leaky mode close to the real axis. The width of the peak is related to the distance of the pole from the real axis, which is directly related to the modal damping versus range. In the present case, the leaky mode is very close to the real axis, and the associated modal damping is small. The modal wavenumbers are also affected by the presence of the bottom, with the second mode in particular moving to a higher horizontal wavenumber, and therefore lower vertical wavenumber compared to the ideal waveguide case. Therefore, the modal excitation is changed as well. The resultant transmission loss is shown in Fig. 2.29b. Since the propagating and the leaky modes are closer in terms of wavenumber, the modal interference length is longer than in the ideal waveguide case. The fact that one of the modes is attenuated with range due to leakage reduces the modal interference with range, and the field will ultimately be dominated by the lossless mode.

This example clearly illustrates the limitation of the traditional normal-mode approach. Thus, if the EJP branch line integral or the leaky modes for the Pekeris branch cut are ignored, only the propagating mode would be included, thus totally eliminating the modal interference, and providing accurate results only at very long ranges. The inclusion of the leaky modes in the solution is most important for cases with few propagating modes, e.g., in low-frequency shallow-water acoustics.

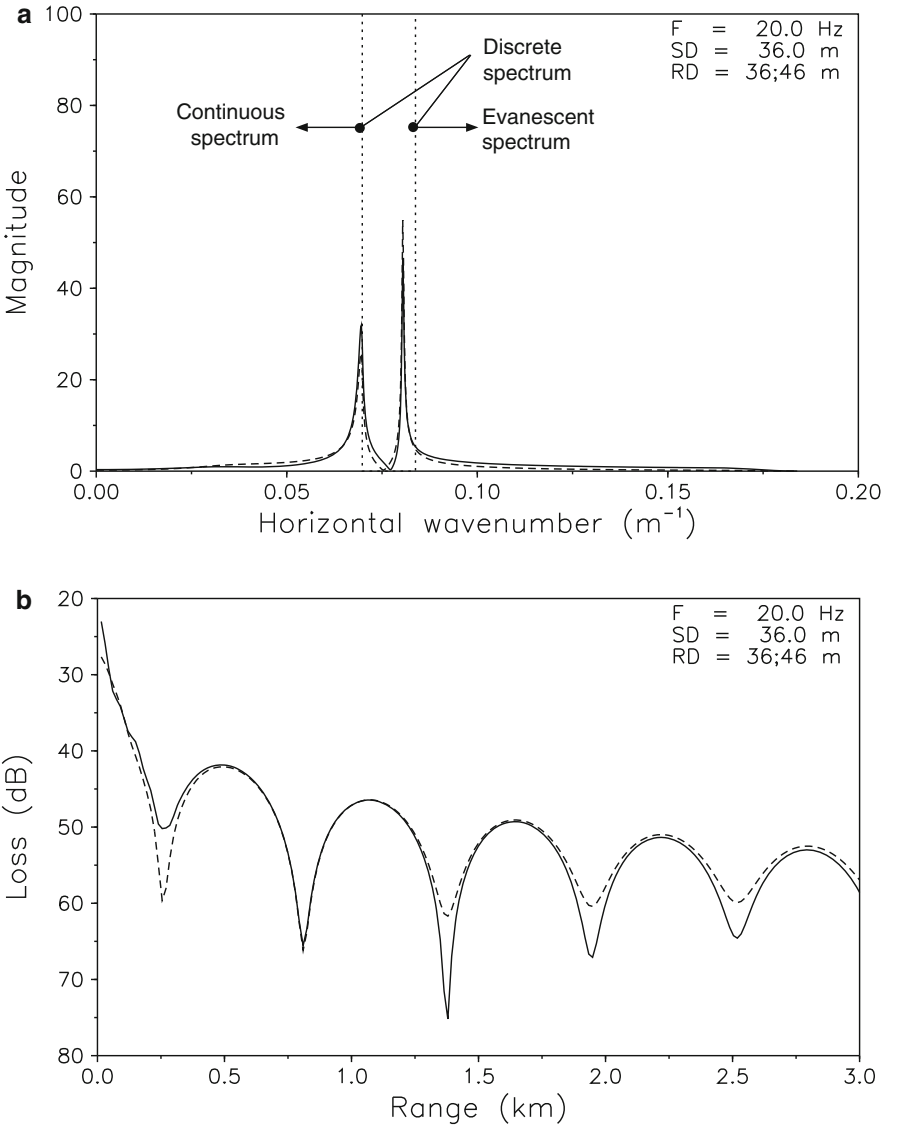

Fig. 2.29 Acoustic field in a 100-m deep Pekeris waveguide for 20 Hz point source at 36 m. (**a**) Magnitude of depth-dependent Green's function. (**b**) Transmission loss. *Solid curve*: Receiver depth 36 m. *Dashed curve*: Receiver depth 46 m

2.4.5.4 Reciprocity

The Pekeris waveguide and other stratified environmental models are characterized by discrete changes in density at the interfaces, with the displacement potential consequently being discontinuous. Therefore, the simple wave equation is not valid

at the interface itself, and the continuity of pressure and particle displacement across the interface is handled through the boundary conditions. As a consequence, the Green's function, although symmetric within each constant-density layer, is not symmetric across the interfaces. However, the acoustic field must still satisfy the *reciprocity principle* of linear acoustics, which is formally derived in Appendix 1. This is easily confirmed by modifying the discrete changes in density and sound speed at the interface to a gradual transition over a small region ϵ. Then the transmission loss pressure for a source at $\mathbf{r}_s$ is governed by the pressure wave equation (2.83), or for a field of time dependence $\exp(-\mathrm{i}\omega t)$,

$$\rho \nabla \cdot \left[\frac{1}{\rho} \nabla P(\mathbf{r}, \mathbf{r}_s) \right] + k^2 P(\mathbf{r}, \mathbf{r}_s) = -4\pi \, \delta(\mathbf{r} - \mathbf{r}_s). \tag{2.193}$$

As described in Appendix 1, the solutions to (2.193) satisfy the reciprocity relation,

$$\rho(\mathbf{r}_s) \, P(\mathbf{r}, \mathbf{r}_s) = \rho(\mathbf{r}) \, P(\mathbf{r}_s, \mathbf{r}). \tag{2.194}$$

Now, by letting the transition region ϵ approach zero, the solution will converge toward the solution for the original problem with discontinuous density and sound speed, and the transmission loss in the Pekeris waveguide and other stratified fluid media must therefore satisfy the reciprocity relation in (2.194) as well.

For the elastic stratifications treated in Chap. 4, the field must also satisfy certain reciprocity relations, specifically the *elastodynamic reciprocity theorem* ([13], Sect. 1.13). This classical reciprocity principle, which forms the basis for many engineering approaches such as the *principle of virtual work*, states that *for two independent forcing systems, the work carried out by the external forcing of one system on the response of the second system, is equal to the work carried out by the external forcing of the second one on the response of the first system*. We will here demonstrate that for fluid media this principle of reciprocity is consistent with (2.194).

For fluid media, the external forces are represented by the volume injection of the source, and the response is represented by the acoustic pressure [14]. Using the source definitions of Sect. 2.3.2, consider a simple point source of strength S_ω at a point $\mathbf{r}_1$ in an acoustic medium with density ρ_1 and sound speed c_1. By definition this source creates a volume injection of $S_\omega \, \delta(\mathbf{r} - \mathbf{r}_1)$. At a receiver $\mathbf{r}_2$ in a medium with density ρ_2 and sound speed c_2 this source will produce a displacement potential $\psi(\mathbf{r}_2)$ with associated pressure,

$$p(\mathbf{r}_2) = \rho_2 \omega^2 \psi(\mathbf{r}_2). \tag{2.195}$$

A point source of strength S'_ω placed at $\mathbf{r}_2$ will similarly correspond to a forcing, or volume injection, of $S'_\omega \, \delta(\mathbf{r} - \mathbf{r}_2)$, and produce a pressure at $\mathbf{r}_1$ given by

$$p'(\mathbf{r}_1) = \rho_1 \omega^2 \psi'(\mathbf{r}_1). \tag{2.196}$$

Now, the classical reciprocity principle states,

$$\int_{\mathrm{V}} S_\omega\, \delta(\mathbf{r}-\mathbf{r}_1)\, p'(\mathbf{r})\, \mathrm{d}V = \int_{\mathrm{V}} S'_\omega\, \delta(\mathbf{r}-\mathbf{r}_2)\, p(\mathbf{r})\, \mathrm{d}V, \tag{2.197}$$

or

$$S_\omega\, p'(\mathbf{r}_1) = S'_\omega\, p(\mathbf{r}_2). \tag{2.198}$$

This is the reciprocity principle for *pressure*. As described in Sect. 2.3.5, in order for the field solutions to directly represent transmission loss, the source strengths must be $S_\omega = 4\pi/(\rho_1\omega^2)$ and $S'_\omega = 4\pi/(\rho_2\omega^2)$. Insertion of these into (2.198) directly yields the reciprocity relation for *transmission loss pressure* in (2.194).

By inserting the relations between potential and pressure into (2.198), we obtain the *reciprocity relation* for the *displacement potentials*,

$$\rho_1 S_\omega \psi'(\mathbf{r}_1) = \rho_2 S'_\omega \psi(\mathbf{r}_2). \tag{2.199}$$

2.4.5.5 Attenuation

Up to this point, we have considered acoustic environments consisting of ideal fluid media. However, in the real ocean, sound waves are attenuated due to dissipation of energy into heat. The attenuation in sea water is very low at low and intermediate frequencies, and acoustic signals may propagate for thousands of kilometers without significant attenuation except for geometrical spreading loss. However, ocean sediments are characterized by high energy loss due to internal friction. Therefore, in environments with significant bottom interaction, such as shallow-water ducts similar to the Pekeris waveguide, bottom attenuation becomes a significant loss factor also for waterborne energy. Hence, in these cases it is crucial for a realistic modeling of the propagation characteristics that bottom attenuation be taken into account. The integral transform technique used for solving the Pekeris problem is easily modified to incorporate this effect.

Assume a plane harmonic wave of angular frequency ω propagating in a homogeneous medium along the positive x-axis of a Cartesian coordinate system. In the absence of attenuation, such a wave has the form

$$\psi(x,t) = A\, \mathrm{e}^{-\mathrm{i}(\omega t - kx)}, \tag{2.200}$$

where k is the medium wavenumber and A is the amplitude. In the ideal fluid, k is real and the plane wave has constant amplitude for all ranges x. However, in reality the wave amplitude will decrease with range, and for media behaving in a linear fashion, e.g., linearly viscoelastic media, this attenuation must be exponential in range, and the plane-wave solution therefore takes the form

$$\psi(x,t) = A\, \mathrm{e}^{-\mathrm{i}(\omega t - kx) - \alpha x}, \qquad \alpha > 0. \tag{2.201}$$

Defining $\alpha = k\delta$, (2.201) can be rewritten as

$$\psi(x,t) = A\,\mathrm{e}^{-\mathrm{i}[\omega t - k(1+i\delta)x]}, \tag{2.202}$$

which is a solution to the Helmholtz equation (2.31) with complex wavenumber,

$$\widetilde{k} = k(1 + \mathrm{i}\delta). \tag{2.203}$$

In isotropic media, the same will be the case for plane, attenuated waves in any spatial direction, and since the integral transform solution is based on a plane-wave decomposition, it is obvious that a viscoelastic attenuation can be accounted for by simply letting the medium wavenumbers be complex. All the waveguide solutions described above are, therefore, directly applicable to problems involving viscoelastic media.

The attenuation factor δ is called the *loss tangent*. However, in underwater acoustics it is more common to express the attenuation in dB/λ, where λ is the wavelength,

$$\alpha = -20\log\left|\frac{\psi(x+\lambda,t)}{\psi(x,t)}\right| = -20\log\left[\mathrm{e}^{-\delta k\lambda}\right] = 40\pi\,\delta\log e \simeq 54.58\,\delta. \tag{2.204}$$

The attenuation in sediments is typically of the order 0.1–1.0 dB/λ (see Sect. 1.6) with the corresponding loss tangents of order 0.002–0.02. Even with the imaginary part of the wavenumber being that small, the attenuation in range can be significant. Thus, Fig. 2.30 shows the transmission loss versus range at 46 m depth for

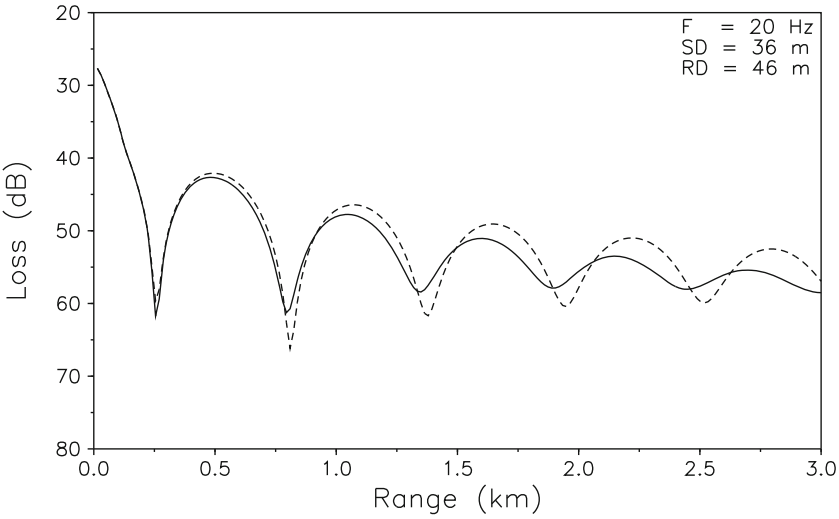

Fig. 2.30 Transmission loss vs. range in a Pekeris waveguide with water depth 100 m. *Solid curve*: 1.0 dB/λ sediment attenuation. *Dashed curve*: lossless

the Pekeris waveguide example. The solid curve is for a bottom loss of 1.0 dB/λ, whereas the dashed curve is the lossless result, identical to the dashed curve in Fig. 2.29b.

There are three differences worth commenting on. Firstly, the transmission loss increases more rapidly with range for the lossy bottom. Secondly, the modal interference length is slightly different in the two cases, and finally the modal interference pattern is disappearing more rapidly with range for the lossy bottom.

Whereas the first difference is expected due to energy loss in the sediment, the two latter points are less obvious. However, they are quite easily explained by analyzing the behavior of the modal poles when attenuation is introduced. In that case, the branch point $k_r = k_2$ in Fig. 2.26 moves slightly off the real axis and into the positive imaginary wavenumber plane. The same is the case for the solutions to the characteristic equation (2.186), with the imaginary part of the wavenumber representing the attenuation in range for the corresponding mode. Also, the real part of the modal wavenumber will change slightly. The effect is stronger the closer the modal wavenumber is to the branch point $k_r = k_2$. Therefore, both the imaginary and the real part of the propagation wavenumber will change more for the higher-order modes than for the lower-order modes. As a result the higher-order modes show more range attenuation than the lower-order modes. In physical terms, this is consistent with the observation that the higher-order modes have longer evanescent tails in the bottom and therefore are more sensitive to changes in bottom parameters.

In the present example, the second mode is leaky and therefore not in the discrete spectrum. However, it is very close to the branch point, thus undergoing bigger changes in terms of both propagation wavenumber and attenuation than the first, discrete mode. The result is a change in the modal interference length as well as a more rapid range decay of the field produced by the second mode, leading to a decaying interference pattern.

The field solutions shown in Fig. 2.30 are computed by wavenumber integration, for which the attenuation is actually an advantage due to the fact that the modal singularities are removed from the real integration axis. However, this example again stresses the care that must be exercised when devising approximate numerical schemes. Thus, as described in Chap. 5, most normal-mode approaches determine the real modal wavenumbers for the lossless case and add the modal attenuation in a perturbational sense. These methods will therefore not predict the change in interference pattern caused by changes in the real part of the propagation wavenumber. In propagation problems with small attenuation and many modes, the error is insignificant, but in extreme cases with high attenuation and few modes, such as the present example, the effect on the interference pattern may be important at long ranges.

2.4.5.6 General Waveguide Image Solution

The Pekeris waveguide has a bottom whose reflection coefficient is given by (1.56). In general, if we let the reflection coefficient of the upper and lower boundaries of

the waveguide be given as $\mathcal{R}_1$ and $\mathcal{R}_2$ evaluated at the appropriate angle associated with each image term, respectively, then the generalized form of (2.138) (from [8]) is

$$\psi(r,z) = \frac{S_\omega}{4\pi} \sum_{m=0}^{\infty} (\mathcal{R}_1\mathcal{R}_2)^m \left[\frac{e^{ikR_{m1}}}{R_{m1}} + \mathcal{R}_1 \frac{e^{ikR_{m2}}}{R_{m2}} + \mathcal{R}_2 \frac{e^{ikR_{m3}}}{R_{m3}} + \mathcal{R}_1\mathcal{R}_2 \frac{e^{ikR_{m4}}}{R_{m4}} \right], \tag{2.205}$$

where we note that $\mathcal{R}_1 = -1$ for the pressure-release surface.

2.4.6 *Waveguide Invariants*

We have been mainly concerned with narrow-band or single-frequency propagation such as the two-mode case shown in Fig. 2.30. It turns out, as shown in Fig. 2.31, that the interference pattern at a slightly shifted frequency for the same propagation conditions has the same structure but with the maxima and minima slightly shifted as indicated by the lines through the maxima. This shift in the structure of the interference pattern as a function of frequency and range is a robust feature of waveguide propagation and is described by a scalar parameter referred to as the waveguide invariant [15, 16]. The same formalism associated with this invariant is also descriptive of the shift in the interference pattern with range and some environmental parameters instead of frequency [17–19]. The waveguide property of maintaining a robust interference pattern under an assortment of conditions is a consequence, as we show below, of an important invariant relationship between the change in group speed with respect to change in phase speed for a group of normal modes in the waveguide.

2.4.6.1 Frequency–Range Waveguide Invariant

We can obtain an expression for the trajectory in the frequency–range plane of the interference maxima (or minima) of the waveguide acoustic intensity I by simply differentiating the normal-mode expression for intensity $I(r,z,\omega) = \text{const.}$ with respect to frequency and range and setting this expression equal to zero,

$$\frac{\delta\omega}{\delta r} = -\frac{\partial I}{\partial r} \Big/ \frac{\partial I}{\partial \omega}. \tag{2.206}$$

Intensity is proportional to the mean square pressure, as per (2.162), and can be written in the form

$$I(r,z;\omega) \propto \sum_n B_n^2 + 2 \sum_{m \neq n} B_m B_n \cos[\Delta k_{mn}(\omega)\, r], \tag{2.207}$$

where $\Delta k_{mn} \equiv k_{rm} - k_{rn}$ are the interfering differences of pairs of horizontal modal wavenumbers and $B_{m,n} = r^{-1/2} A_{m,n}$ are the mode amplitudes of (2.162)

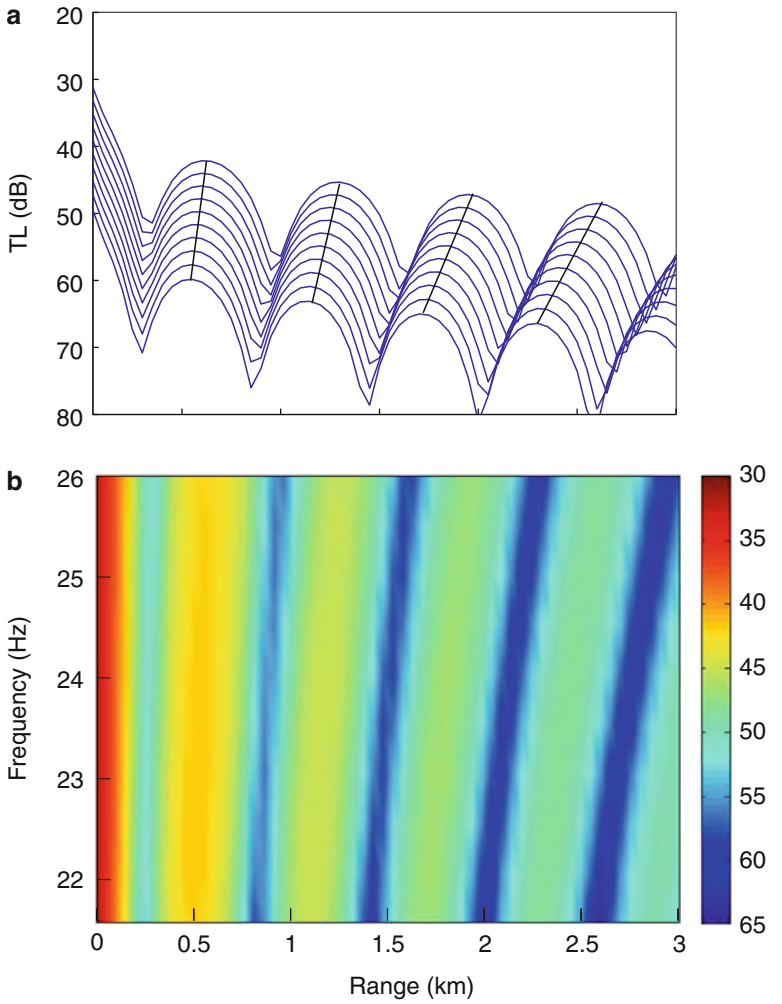

Fig. 2.31 Acoustic field in an ideal waveguide of *thickness* 100 m for 20 Hz point source at 36 m depth. (**a**) Transmission loss from 21.5 to 26.0 Hz with 2 dB offset between curves. (**b**) Contour plot of (**a**) without offsets and with TL as the z-axis. These intensity bands are often referred to as striations

and are weakly dependent on range at specific ranges. Differentiating with respect to ω and r and only retaining the dominant range terms, we obtain

$$\frac{\partial I}{\partial r} = -\sum_{m,n} B_n B_m (\Delta k_{mn}) \sin(\Delta k_{mn}\, r), \tag{2.208}$$

$$\frac{\partial I}{\partial \omega} = -r \sum_{m,n} B_n B_m \left(\frac{\partial \Delta k_{mn}}{\partial \omega} \right) \sin(\Delta k_{mn}\, r), \tag{2.209}$$

which we can immediately write as

$$\frac{\partial I}{\partial r} = -\omega \sum_{m,n} B_n B_m \left(\frac{1}{v_m} - \frac{1}{v_n} \right) \sin(\Delta k_{mn}\, r), \tag{2.210}$$

$$\frac{\partial I}{\partial \omega} = -r \sum_{m,n} B_n B_m \left(\frac{1}{u_m} - \frac{1}{u_n} \right) \sin(\Delta k_{mn}\, r), \tag{2.211}$$

where the phase and group velocities v_n and u_n are given by (2.156) and (2.158), respectively. Assuming a functional relationship between group and phase velocity, we can express individual phase and group velocities as a Taylor expansion around the average phase and group velocity v and u of a group of modes. Since (2.210) and (2.211) involve the inverse of phase and group velocity, which are defined as phase and group *slowness*, it is preferable to perform the expansion in terms of phase and group slowness ($1/v$ and $1/u$),

$$S_g^n = S_g + \frac{\mathrm{d}S_\mathrm{g}}{\mathrm{d}S_\mathrm{p}} \left(S_\mathrm{p}^n - S_\mathrm{p} \right), \tag{2.212}$$

where S_p^n and S_g^n are the phase and group slowness, respectively, of the nth mode. In addition, S without the superscript refers to the average phase and group slowness of the group of modes. Inserting the above expressions into (2.206) together with the definition of phase and group slowness (and taking S to be centered about the mth mode) gives

$$\frac{\delta r}{\delta \omega} = -\frac{r}{\omega} \frac{\mathrm{d}S_\mathrm{g}}{\mathrm{d}S_\mathrm{p}}. \tag{2.213}$$

We now define the "invariant" β such that,

$$\frac{1}{\beta} \equiv -\frac{\mathrm{d}S_\mathrm{g}}{\mathrm{d}S_\mathrm{p}} = -\left(\frac{v}{u} \right)^2 \frac{\mathrm{d}u}{\mathrm{d}v}, \tag{2.214}$$

so that we can rewrite (2.213) as

$$\frac{\delta \omega}{\delta r} = \beta \frac{\omega}{r} \tag{2.215}$$

or

$$\frac{\omega}{\omega_0} = \left(\frac{r}{r_0} \right)^\beta. \tag{2.216}$$

We now demonstrate that β is approximately constant for a group of modes. Return to the ideal waveguide as described by the geometry of Fig. 2.20 and note that $k_r \equiv \omega/v = k \cos\theta = (\omega/c)\cos\theta$, where we have suppressed the modal index. Therefore, we have for the phase velocity,

$$v = \frac{\omega}{k_r} = \frac{c}{\cos\theta}. \tag{2.217}$$

Using (2.158), together with the assumption that the depth (or angle) dependence of the group of modes we are considering is approximately frequency independent (e.g., k_{mz} for the ideal waveguide is not a function of frequency), the group velocity is given by $u = c\ \cos\theta$. We can then write the invariant for a simple waveguide as

$$\beta = \cos^2\theta. \tag{2.218}$$

Since typical shallow-water environments have bottom critical angles of less than 20°, we have that for most bottom-reflecting shallow-water environments, $\beta \approx 1$. We will further discuss values of β for various profiles in Chap. 5.

2.4.6.2 Generalized Waveguide Invariant

The previous procedure can be generalized [18] to include variations in environmental parameters instead of either range or frequency. For example, we may seek the constant intensity trajectory in the frequency–water depth plane, i.e., the change in the broadband frequency spectrum when the waveguide depth is changed. In that case, we would simply set the total intensity differential with respect to frequency and water depth equal to zero. Similarly, if we were interested in the spectral change with respect to some sound speed variation, we would set the total differential with respect to frequency and the parameter characterizing the sound speed (change) equal to zero. In both of the above cases, the partial of the intensity with respect to water depth or sound speed results in changing the cosine terms in (2.207) to a sine term. However, we now have to take derivatives of Δk_{mn} with respect to these parameters rather than the derivative with respect to range which just factored out the phase slowness terms.

To proceed with the generalization of the invariant formulation, we note from the derivation of (2.213), that the basic ingredient facilitating this derivation was that the coefficients of the $\sin(\Delta k_{mn}\, r)$ are constant and could be factored out of the summation. We showed this to be true by a Taylor expansion around a group of modes. This is actually a stationary phase [$\delta\Phi = \delta(\Delta k_{mn}\, r) = 0$] statement that the lines of constant intensity, which we refer to as striations, for a group of modes arise from the general condition of keeping the cosine term (and hence, its argument) in (2.207) constant. We can continue from (2.206) with the assumption that these terms are constant to obtain, after some straightforward algebra,

$$\frac{\delta r}{\delta \omega} = -\frac{r}{\omega}\left(\frac{\partial \Delta k_{mn}}{\partial \omega} \Big/ \frac{\Delta k_{mn}}{\omega}\right), \tag{2.219}$$

which, given the definitions of group and phase speed (and slowness), is identical to (2.213) and therefore, in analogy to (2.216), we have

$$\frac{\Delta k_{mn}}{(\Delta k_{mn})_0} = \left(\frac{\omega}{\omega_0}\right)^{-\frac{1}{\beta}}. \tag{2.220}$$

Equation (2.220) states how a wavenumber difference changes with frequency starting from a given wavenumber difference. Recall from (2.163) that the wavenumber difference yields the modal interference length so that we can rewrite (2.220) in terms of how a modal interference length L_0 evolves with frequency,

$$L = L_0 \left(\frac{\omega}{\omega_0} \right)^{\frac{1}{\beta}}. \tag{2.221}$$

Now, let η_q represent each of the waveguide parameters $q = r, \omega, D, c$, denoting range, frequency, water depth and sound speed, respectively, and define $\Phi \equiv \Delta k_{mn} r$. The general stationary phase condition is therefore

$$\delta\Phi = \sum_q \frac{\partial \Phi}{\partial \eta_q} \delta\eta_q. \tag{2.222}$$

Then, with $r \equiv \eta_r$, $\omega \equiv \eta_\omega$ and using the definition of Φ, we have

$$\left(\frac{\partial \Delta k_{mn}}{\Delta k_{mn}} \Big/ \frac{\partial \eta_h}{\eta_h} \right) \frac{\delta\eta_h}{\eta_h} + \left(\frac{\partial \Delta k_{mn}}{\Delta k_{mn}} \Big/ \frac{\partial \eta_c}{\eta_c} \right) \frac{\delta\eta_c}{\eta_c} + \left(\frac{\partial \Delta k_{mn}}{\Delta k_{mn}} \Big/ \frac{\partial \omega}{\omega} \right) \frac{\delta\omega}{\omega} + \frac{\delta r}{r} = 0, \tag{2.223}$$

which, of course, reduces to (2.219) when there is no variation in water depth or sound speed.

Now consider the variation in frequency when the water depth is changed, i.e., the shift of the power spectrum interference maxima and minima as a function of waveguide depth. We already know from (2.206) and (2.219) that the expression in the parentheses of the third term is $-1/\beta$. The expression in the first parentheses can be obtained from (2.148) where we also note from (2.192) that the Pekeris waveguide wavenumbers approach the ideal waveguide wavenumbers for high frequency. As a matter of fact, the eigenvalues of this general class of *Sturm–Liouville* problems go to the ideal waveguide wavenumbers for large m.

Taking $k_m = \sqrt{k^2 - m^2\pi^2/{\eta_h}^2}$, and noting that $k_m + k_n \approx 2k_m$, we get

$$\frac{\partial \Delta k_{mn}}{\partial \eta_h} = -\frac{2\Delta k_{mn}}{\eta_h} \tag{2.224}$$

so that, taken alone, the first and third terms of (2.223) reduce to

$$\frac{\delta\omega}{\delta\eta_h} = -2\beta \frac{\omega}{\eta_h}. \tag{2.225}$$

This last expression is equivalent to an expression in Weston et al. [17] in which they studied time–frequency interference patterns resulting from a shallow-water

tidal cycle and where they also experimentally confirmed the above factor of 2. Similarly, consider the second term of (2.223), recalling that $k = \omega/c$, we obtain

$$\frac{\partial \Delta k_{mn}}{\partial \eta_c} = \left(\frac{k^2}{k_m k_n}\right) \frac{\Delta k_{mn}}{\eta_c} \approx \frac{\Delta k_{mn}}{\eta_c}, \tag{2.226}$$

where the last relation comes from the expression in parenthesis being approximately unity for a mode group such that $m \approx n$ and for $kh \gg 1$. Considering variation in only the second and third terms of (2.223), we arrive at another invariant-like expression,

$$\frac{\delta \omega}{\delta \eta_c} = \beta \frac{\omega}{\eta_c}. \tag{2.227}$$

Hence, (2.215), (2.225), and (2.227) are "invariant" expressions for the ideal waveguide stating that the slope of the lines of constant intensity is an invariant for a specific mode group in a coordinate system of relative increments of ω and η_q. Though our derivation was specific for ideal waveguides and/or Pekeris waveguides with high mode numbers, the result is more general; the invariants can be numerically calculated for a much broader class of waveguides and also approximated analytically for an assortment of waveguides [16]. The generalized invariant equations can therefore be written as

$$\frac{\delta \omega}{\delta \eta_q} = \gamma_{\omega:q} \frac{\omega}{\eta_q}, \tag{2.228}$$

where q is either range r, water depth D or sound speed c and we have shown above that for an ideal waveguide γ is given by

$$\gamma_{\omega:r,D,c} \approx 1, -2, 1, \tag{2.229}$$

where the notation indicates that we are considering variations in the interference structure in which one of the coordinates is always ω. Therefore, (2.219), (2.224), and (2.226) can also be summarized as

$$\frac{\partial \Delta k_{mn}}{\partial \eta_q} = \frac{\gamma_{\omega:q}}{\beta} \frac{\Delta k_{mn}}{\eta_q}, \qquad q = r, D, c. \tag{2.230}$$

These invariant expressions are particularly useful for studying a single hydrophone (and therefore at a single range) observable such as the shift in a spectral (frequency vs. intensity) broadband interference pattern with respect to the variation in one of the q parameters. In terms of invariants of the pairwise coordinate systems, i.e., (r, ω), (D, ω), (c, ω), we can treat (2.223) as the result of a separation of variables yielding the three partial differential equations for $\Delta k_{mn}(D, \omega)$, $\Delta k_{mn}(c, \omega)$ and $\Delta k_{mn}(r, \omega)$ as summarized by (2.230). After some algebra, the product of the three separation of variable solutions is

$$\Delta k_{mn} = \alpha_{mn}\, \eta_D^{\gamma_{\omega:D}/\beta}\, \eta_c^{\gamma_{\omega:c}/\beta}\, \omega^{-1/\beta}, \tag{2.231}$$

where α_{mn} is a mode number dependent constant. Thus, for the ideal waveguide, we obtain

$$\Delta k_{mn} = \alpha_{mn} \frac{c}{\omega D^2} = \alpha_{mn} \frac{1}{kD^2}. \tag{2.232}$$

To check these results, we can just write out the expression for Δk_{mn} and take the limit of $kh \gg 1$ to obtain

$$\Delta k_{mn} \approx \frac{(n^2 - m^2)\pi^2}{2} \frac{1}{kD^2}, \tag{2.233}$$

which agrees with (2.232).

The results presented in this section were mostly for an ideal waveguide. For more complicated environments, we must use numerical methods to compute the relevant modal quantities. This is discussed in some detail in Sect. 5.14.

2.5 Deep-Ocean Waveguides

In the previous section, we discussed propagation in waveguides composed of homogeneous fluid layers. Such environmental models are rather simplistic but they are useful for illustrating the fundamental characteristics of ocean acoustic propagation. Real sound-speed profiles have depth dependence and consequently need to be represented by a combination of layering and variable sound speed within the layers.

In general, the ocean environment varies in all spatial coordinates as well as time, with the latter giving rise to temporal fluctuations. Although the fluctuations will usually be characterized by temporal scales long compared to the acoustic time scales, they may have significant effect on advanced, high-resolution signal processing schemes based on ensemble averaging of the acoustic field. The development of ocean acoustic models for determining the stochastic properties of the field is still in its infancy, and the temporal variability is generally addressed through Monte Carlo simulations with deterministic models.

In terms of the spatial variability, the scales play an important role as well. Thus, the variability on scales smaller than the wavelength are best incorporated in a stochastic sense, and in recent years a significant effort has gone into the modeling of ocean environments with small-scale stochastic variability such as interface roughness and volume inhomogeneities–important mechanisms for scattering and reverberation. However, the propagation models in widespread use do not include stochastic variability but only large scale variability of deterministic nature.

The complexity of the acoustic modeling depends on the nature of the spatial variability. Thus, the real ocean has variation in sound speed with depth as well as in the horizontal. In general, the two- and three-dimensional variation requires the use of one of the numerical models described in later chapters, such as three-dimensional ray tracing, adiabatic or coupled modes, or parabolic equation

approaches. However, the basic physics of deep-ocean-waveguide propagation can be addressed by simpler methods due to the fact that the spatial scales of the horizontal variability in most cases are much larger than the scales of the vertical variability. Therefore, a range independent environmental model for the deep ocean can provide a realistic prediction of the acoustic propagation. This is particularly true at Arctic latitudes where the atmospheric influence on the underwater acoustic environment is limited by the ice cover and where the strongly upward refracting sound-speed profile eliminates effects of bottom bathymetry on long-range propagation.

Realistic range independent environmental models for the deep ocean are shown in Fig. 1.1. The deep ocean waveguide cannot, in general, be represented by a homogeneous fluid layer. However, if the range-independent ocean waveguide is represented by an increasing number of homogeneous layers, a numerical solution based on the field representation for homogeneous layers will converge toward the correct solution. It turns out, however, that a satisfactory convergence requires the layers to be less than one quarter of a wavelength thick. Such a technique is therefore only computationally convenient for low-frequency propagation in moderate water depths.

In general, it is much more convenient to divide the deep ocean into a relatively few number of layers with depth-varying properties in a form that allows for an analytic solution to the wave equation within each layer. We therefore seek solutions to the Helmholtz equation for the range-independent ocean environment,

$$\left[\nabla^2 + k^2(z)\right] \psi(r,z) = S_\omega \, \frac{\delta(r)\,\delta(z-z_s)}{2\pi r}, \tag{2.234}$$

where the medium wavenumber $k(z)$ is now a function of depth. We can still solve this equation by separation of variables or by integral transforms to yield,

$$\psi(r,z) = \int_0^\infty \psi(k_r,z)\, J_0(k_r r)\, k_r \, \mathrm{d}k_r \tag{2.235}$$

with $\psi(k_r,z)$ satisfying the depth-separated wave equation,

$$\left[4\frac{\mathrm{d}^2}{\mathrm{d}z^2} + \left(k^2(z) - k_r^2\right)\right] \psi(k_r,z) = S_\omega \, \frac{\delta(z-z_s)}{2\pi}. \tag{2.236}$$

The use of the integral transform approach is dependent on the availability of solutions to (2.236). For certain variations of the medium wavenumber $k(z)$, exact solutions can be obtained. Alternatively, approximate solutions may be obtained. In the following we describe such exact and approximate solutions to (2.236).

2.5.1 Exact Solutions

The deep-ocean waveguide is generally represented by a series of layers, within which the depth-dependence of the field has an analytic representation. A few examples of sound speed interpolation functions for which this is possible are given

in [20]. However, the actual choice of interpolation function is not very critical since the profile is usually measured at discrete depths with a finite uncertainty. We, here, describe the solution for a medium with the *pseudo-linear* sound speed variation

$$c(z) = \sqrt{\frac{1}{az+b}}. \tag{2.237}$$

Such a medium has a linear variation of the square of the index of refraction, $n^2 = az + b$, and is therefore also referred to an n^2-linear acoustic medium. The expression for the sound speed in (2.237) obviously only has physical meaning for depths satisfying the inequality $az + b > 0$. For this sound speed variation, the homogeneous, depth-separated wave equation becomes,

$$\left[\frac{\mathrm{d}^2}{\mathrm{d}z^2} - \left[k_r^2 - \omega^2 (az+b)\right]\right] \psi(k_r, z) = 0. \tag{2.238}$$

By introducing the variable transformation,

$$\zeta = (\omega^2 a)^{-2/3} \left[k_r^2 - \omega^2 (az+b)\right] \tag{2.239}$$

the following wave equation is obtained,

$$\left[\frac{\mathrm{d}^2}{\mathrm{d}\zeta^2} - \zeta\right] \psi(\zeta) = 0. \tag{2.240}$$

This is a special form of the Bessel differential equation, with two independent solutions given by the Airy functions Ai (ζ) and Bi (ζ) [21]. Independent homogeneous solutions to (2.238) are therefore

$$\psi^+(k_r, z) = \mathrm{Ai}\left([\omega^2 a]^{-2/3}\left[k_r^2 - \omega^2 (az+b)\right]\right), \tag{2.241}$$

$$\psi^-(k_r, z) = \mathrm{Bi}\left([\omega^2 a]^{-2/3}\left[k_r^2 - \omega^2 (az+b)\right]\right). \tag{2.242}$$

The field produced by a point source at depth z_s in such a medium is determined by introducing a thin homogeneous layer of sound speed $c(z_s)$ and thickness ϵ around the source, see Fig. 2.32. In the limit $\epsilon \to 0$, the solution of this layered problem converges to the solution of the original problem.

In Fig. 2.32, the sound speed variation is shown for the case in which $a > 0$, i.e., $\lim_{z\to\infty} c(z) = 0$ and $\lim_{z\to -b/a} c(z) = \infty$. The argument ζ of the Airy functions, (2.239), therefore has the limits,

$$\lim_{z\to\infty} \zeta = -\infty, \tag{2.243}$$

$$\lim_{z\to -b/a} \zeta = +\infty. \tag{2.244}$$

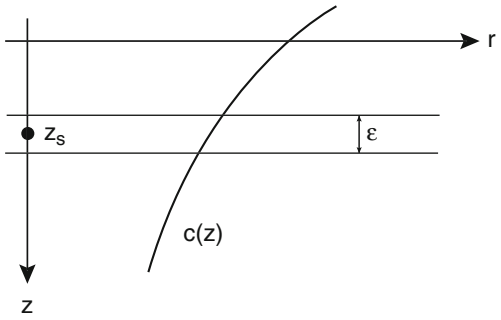

Fig. 2.32 Point source in n^2-linear fluid medium

Since no sources are present in the two halfspaces, the field is given by (2.241) and (2.242), respectively. However, the field must satisfy the radiation condition for $z\to\infty$ and the field must be limited for $z \to -b/a$. Since $\lim_{\zeta\to\infty} \mathrm{Bi}\,(\zeta) = \infty$ [21], the latter condition requires the depth dependence of the field in the upper halfspace to be of the form

$$\psi_1(k_r, z) = A_1^+ \,\mathrm{Ai}\,(\zeta). \tag{2.245}$$

Similarly, the radiation condition requires that only downgoing waves exist for $z\to\infty$. Because of the asymptotic behavior of the Airy functions for $\zeta \to -\infty$ [21], it is required that the field in the lower halfspace be of the form

$$\psi_3(k_r, z) = A_3^- \left[\mathrm{Ai}\,(\zeta) - \mathrm{i}\,\mathrm{Bi}\,(\zeta)\right]. \tag{2.246}$$

For the intermediate isovelocity layer, the depth-dependence of the field is directly given by (2.141), (2.142) and (2.143) as

$$\psi_2(k_r, z) = A_2^+ \,\mathrm{e}^{\mathrm{i}k_{z,2}\,z} + A_2^- \,\mathrm{e}^{-\mathrm{i}k_{z,2}\,z} + S_\omega \,\frac{\mathrm{e}^{\mathrm{i}k_{z,2}|z-z_s|}}{4\pi i k_{z,2}}. \tag{2.247}$$

The next step is to satisfy the boundary conditions of continuity of vertical displacement and pressure at the two interfaces at $z = z_s \pm \epsilon/2$. The expressions for the vertical displacement and pressure in terms of the displacement potential, (2.21) and (2.23), then leads to the following system of equations expressing the boundary conditions for $\epsilon \to 0$,

$$A_1^+ \left[-\left(\omega^2 a\right)^{1/3} \mathrm{Ai}'\,(\zeta_s)\right] - \mathrm{i}k_{z,2}\left(A_2^+ - A_2^-\right) = -\frac{S_\omega}{4\pi}, \tag{2.248}$$

$$-A_1^+ \,\mathrm{Ai}\,(\zeta_s) + \left(A_2^+ + A_2^-\right) = -\frac{S_\omega}{4\pi i k_{z,2}}, \tag{2.249}$$

$$i k_{z,2}\left(A_2^+ - A_2^-\right) - A_3^-\left(-\left(\omega^2 a\right)^{1/3}\left[\mathrm{Ai}'\,(\zeta_s) - \mathrm{i}\,\mathrm{Bi}'\,(\zeta_s)\right]\right) = -\frac{S_\omega}{4\pi}, \tag{2.250}$$

$$-\left(A_2^+ + A_2^-\right) + A_3^-\left[\mathrm{Ai}\,(\zeta_s) - \mathrm{i}\,\mathrm{Bi}\,(\zeta_s)\right] = \frac{S_\omega}{4\pi i k_{z,2}}. \tag{2.251}$$

Here, the primes denote differentiation with respect to the argument. All terms involving the coefficients A_2^+ and A_2^- are easily eliminated by pair-wise addition, and the resulting two equations give the following solutions,

$$A_1^+ = -\frac{S_\omega}{4\pi} \frac{2\,(\omega^2 a)^{-1/3}\,[\mathrm{Ai}\,(\zeta_s) - \mathrm{i}\,\mathrm{Bi}\,(\zeta_s)]}{\mathrm{Ai}\,'(\zeta_s)\,[\mathrm{Ai}\,(\zeta_s) - \mathrm{i}\,\mathrm{Bi}\,(\zeta_s)] - \mathrm{Ai}\,(\zeta_s)\,[\mathrm{Ai}\,'(\zeta_s) - \mathrm{i}\,\mathrm{Bi}\,'(\zeta_s)]}, \tag{2.252}$$

$$A_3^- = -\frac{S_\omega}{4\pi} \frac{2\,(\omega^2 a)^{-1/3}\mathrm{Ai}\,(\zeta_s)}{\mathrm{Ai}\,'(\zeta_s)\,[\mathrm{Ai}\,(\zeta_s) - \mathrm{i}\,\mathrm{Bi}\,(\zeta_s)] - \mathrm{Ai}\,(\zeta_s)\,[\mathrm{Ai}\,'(\zeta_s) - \mathrm{i}\,\mathrm{Bi}\,'(\zeta_s)]}. \tag{2.253}$$

The source field representations for the case where the sound speed increases with depth, i.e., $a < 0$, is directly determined by symmetry considerations. The choice of depth axis z is arbitrary, and we can therefore perform the variable transformation $z \to -z$. This will change the sign of a in (2.237), and, as can be observed from (2.239), ζ is then invariant to this transformation, and consequently the results above are still valid; they just have to be interchanged between the two halfspaces. The depth-dependent solution for a source in a n^2-linear fluid medium is therefore,

$$\psi(k_r, z) = -\frac{S_\omega}{4\pi} \times \begin{cases} \dfrac{2(\omega^2 a)^{-1/3}[\mathrm{Ai}\,(\zeta_s) - \mathrm{i}\,\mathrm{Bi}\,(\zeta_s)]\mathrm{Ai}\,(\zeta)}{\mathrm{Ai}\,'(\zeta_s)[\mathrm{Ai}\,(\zeta_s) - \mathrm{i}\,\mathrm{Bi}\,(\zeta_s)] - \mathrm{Ai}\,(\zeta_s)[\mathrm{Ai}\,'(\zeta_s) - \mathrm{i}\,\mathrm{Bi}\,'(\zeta_s)]}, & a(z - z_s) \le 0 \\ \dfrac{2(\omega^2 a)^{-1/3}\mathrm{Ai}\,(\zeta_s)[\mathrm{Ai}\,(\zeta) - \mathrm{i}\,\mathrm{Bi}\,(\zeta)]}{\mathrm{Ai}\,'(\zeta_s)[\mathrm{Ai}\,(\zeta_s) - \mathrm{i}\,\mathrm{Bi}\,(\zeta_s)] - \mathrm{Ai}\,(\zeta_s)[\mathrm{Ai}\,'(\zeta_s) - \mathrm{i}\,\mathrm{Bi}\,'(\zeta_s)]}, & a(z - z_s) \ge 0. \end{cases} \tag{2.254}$$

In the next section, we use the approximate WKB ray solution to explain the physical significance of the solution in (2.254). Furthermore, in Chap. 4 we show how these solutions are applied to solve wave propagation problems in the deep ocean by dividing the environment into a set of discrete layers with an n^2-linear sound speed variation, (2.237), in each layer.

2.5.2 WKB Solutions

The depth-separated wave equation (2.236) is an ordinary differential equation which, without the source term, has the form

$$\frac{\mathrm{d}^2\psi(z)}{\mathrm{d}z^2} + k_z^2(z)\,\psi(z) = 0, \tag{2.255}$$

where $k_z(z)$ is the depth-dependent vertical wavenumber. In the WKB approximation [7], we seek solutions to (2.255) in the form

$$\psi(z) = A(z)\,\mathrm{e}^{\mathrm{i}\phi(z)}, \tag{2.256}$$

where $A(z)$ and $\phi(z)$ are real functions of depth. For a homogeneous medium, solutions of this form are exact, with $A(z) = A$ and $\phi(z) = \pm k_z z$. However, for general variations of the wavenumber, only approximate solutions of this form can be obtained, and the relative accuracy depends on the actual sound-speed profile. Inserting (2.256) into (2.255) yields

$$\left[A''(z) + \left(k_z^2(z) - \left[\phi'(z)\right]^2\right) A(z)\right] + i\left[2A'(z)\,\phi'(z) + A(z)\,\phi''(z)\right] = 0. \tag{2.257}$$

This equation requires that both the real and the imaginary term vanish. If we assume that the amplitude of the solution varies slowly in depth, such that

$$\left|\frac{A''(z)}{k_z^2(z)\,A(z)}\right| \ll 1, \tag{2.258}$$

then the equation for the real part of (2.257) takes the form

$$\left[\phi'(z)\right]^2 = k_z^2(z) \tag{2.259}$$

with the solution

$$\phi(z) = \pm \int_{z_0}^{z} k_z(z)\,\mathrm{d}z, \tag{2.260}$$

where z_0 is an arbitrary constant. Inserting $\phi'(z) = \pm k_z(z)$ into the equation for the imaginary part then yields

$$2A'(z)\,k_z(z) + A(z)\,k_z'(z) = 0 \tag{2.261}$$

with the solution

$$A(z) = \frac{B}{\sqrt{k_z(z)}}, \tag{2.262}$$

where B is an arbitrary amplitude. Inserting these solutions into (2.256) then yields the *WKB approximation* to the depth-separated wave equation,

$$\psi(z) = \frac{B}{\sqrt{k_z(z)}}\,\mathrm{e}^{\pm \mathrm{i}\int_{z_0}^{z} k_z(z)\,\mathrm{d}z}. \tag{2.263}$$

In terms of physical significance, the WKB approximation is a representation in terms of local plane-wave solutions, propagating horizontally with wavenumber k_r and vertically with wavenumber $k_z(z)$. It is, therefore, a solution in terms of *rays* propagating at grazing angle $\theta(z) = \arctan\left[k_z(z)/k_r\right] = \arccos\left[k_r/k(z)\right]$, i.e., plane waves satisfying Snell's law. The two solutions in (2.263) are propagating downward and upward for the positive and negative exponents, respectively. The individual solutions therefore do not contain internal reflections, as an exact solution

must do. The condition given by (2.258) represents the contribution from internal reflections. By inserting the amplitude solution, (2.262), into (2.258), the WKB condition can be rewritten as

$$\left| \frac{1}{k_z^2(z)} \left(\frac{\mathrm{d}^2}{\mathrm{d}z^2} \ln k_z^2(z) - \left[\frac{\mathrm{d}}{\mathrm{d}z} \ln k_z(z) \right]^2 \right) \right| \ll 1. \tag{2.264}$$

If $k_z(z)$ is assumed to be locally linear, then this condition is equivalent to

$$\frac{1}{k_z(z)} \left| \frac{\mathrm{d}}{\mathrm{d}z} \ln k_z(z) \right| \ll 1, \tag{2.265}$$

which shows that the WKB approximation is valid if the variation in the vertical wavenumber is small over a vertical wavelength. The WKB ray solution is therefore a *high-frequency approximation*. However, even at high frequencies the approximation will break down at points where the vertical wavenumber vanishes. In other words, the internal reflection cannot be neglected when the grazing angle of the WKB rays approach horizontal, i.e., $k_r = k(z)$. The behavior of the WKB ray solution, therefore, needs special consideration for rays approaching such *turning points*.

In a downward refracting sound-speed profile (Fig. 2.33), we assume an upward propagating ray of horizontal wavenumber k_r, represented by the solution with the negative exponent in (2.263),

$$\psi^-(z) = \frac{B^-}{\sqrt{k_z(z)}} \, \mathrm{e}^{-\mathrm{i} \int_{z-}^{z} k_z(z)\, \mathrm{d}z}. \tag{2.266}$$

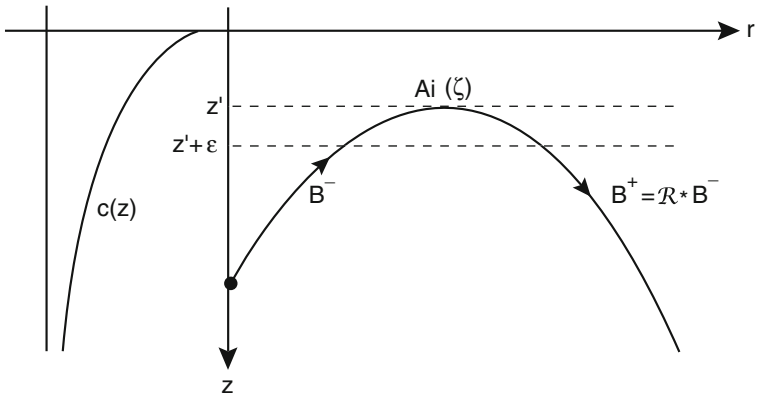

Fig. 2.33 Reflection of a WKB ray at a turning point

After passing through the turning point at depth z' this ray will be downward refracted and must be represented by the solution with the positive exponent in (2.263),

$$\psi^+(z) = \frac{B^+}{\sqrt{k_z(z)}} \, \mathrm{e}^{\,\mathrm{i} \int_{z^+}^{z} k_z(z)\,\mathrm{d}z}. \tag{2.267}$$

To determine the arbitrary constants B^+ and z^+ we can introduce an interface just below the turning point at depth $z' + \epsilon$, and represent the solution at and above the turning point by the exact solution $\mathrm{Ai}\,(\zeta)$, assuming the medium to have an n^2-linear sound speed variation locally. We can then determine the constants from the boundary conditions of continuity of pressure and displacement at depth $z' + \epsilon$. Since the amplitudes of the WKB solutions were assumed to be real, the phase of the downgoing ray is determined by the difference between z^+ and z^-. However, for simplicity we can choose these to be identical, $z^- = z^+$, and instead allow $B^\pm$ to be complex entities.

We now determine B^+ by solving a standard reflection problem, $B^+ = \mathcal{R}\, B^-$, with $\mathcal{R}$ being the reflection coefficient. Since energy must be conserved, the ray must be totally reflected, requiring $|B^+| = |B^-|$. By representing the Airy function in terms of Bessel functions, the solution of the reflection problem shows that in the high-frequency limit, the ray must have a $\pi/2$ phase shift [7], i.e.,

$$B^+ = B^- \mathrm{e}^{-\mathrm{i}\pi/2}\,. \tag{2.268}$$

An important feature of the WKB solution is its direct physical interpretation in terms of rays, and we can therefore use it to address the physical significance of the exact solution in (2.254) for the n^2-linear medium. Assume that a plane wave, represented by a *ray*, of horizontal wavenumber k_r is launched upward from a source at depth $z_s > z' = a\,(k_r^2/\omega^2 - b)$, in a medium with $a > 0$, i.e., the sound speed is decreasing with depth. At the source the argument to the Airy function $\mathrm{Ai}\,(\zeta)$ is negative. At the depth z' the horizontal wavenumber is equal to the local medium wavenumber, $k_r = k(z')$, corresponding to a horizontally propagating plane wave, with the argument to the Airy function being $\zeta = 0$. Above this *turning point*, the field will decay rapidly for $z \to -b/a$. This evanescent field is only predicted by the exact Airy function solution, but not by the WKB ray solution. After reaching the turning point the ray will refract downward, superimposed with the upgoing component yielding a standing wave solution in the vertical above the source, represented by the Airy function $\mathrm{Ai}\,(\zeta)$. Below the source the ray as well as the exact depth solution must propagate downward to infinity, a behavior represented by the linear combination of the Airy functions $\mathrm{Ai}\,(\zeta) - \mathrm{i}\,\mathrm{Bi}\,(\zeta)$.

The difference between the WKB approximation and the exact solution is most dramatic at and beyond the turning point. However, when the turning points are close to the waveguide boundaries in terms of wavelengths, such that the reflection of the evanescent "tail" cannot be neglected, then the field elsewhere in the waveguide will be affected as well. These fundamental differences between the WKB ray approximation and exact solutions for the n^2-linear medium will be illustrated by numerical examples in Chap. 3.

The WKB approach is rarely used in *wavenumber integration* approaches. However, it has been used extensively in relation to *ray tracing* in range-independent environments as described in Chap. 3. In addition, the WKB approach provides a very simple means of determining approximations to the modal eigenvalues in the *normal mode* approach. As described earlier, the modal wavenumbers are those for which two ray multiples are in phase. We can therefore use the WKB approach to trace a ray upward from some depth z_s, through a turning point, incorporating the phase shift, or through a surface reflection. The downgoing ray is then traced similarly through the deep ocean turning point or the bottom reflection until it again reaches the depth z_s. If the up- and downgoing field components at this point are in phase, then the horizontal wavenumber is a modal wavenumber. The use of the WKB mode approximation is described in more detail in Chap. 5.

Appendix 1: Principle of Reciprocity

In deriving *Green's theorem* in Sect. 2.3.3, we had to assume that $G_\omega(\mathbf{r}, \mathbf{r_0})$ is symmetric in $\mathbf{r}$ and $\mathbf{r_0}$. In Sect. 2.3.2, we showed that the free-field Green's function $g_\omega(\mathbf{r}, \mathbf{r_0})$ is symmetric, but the same is not the case unconditionally for G_ω, in spite of the fact that the two functions satisfy the same differential equation. For example, if we choose the homogeneous solution as a plane wave, $H_\omega(\mathbf{r}) = \exp(\mathrm{i}\mathbf{k}\cdot\mathbf{r})$, then G_ω satisfies (2.60), but is clearly not symmetric.

The symmetry of the Green's function is a result of the general *principle of reciprocity* of linear acoustics, and in this appendix we shall derive this very important principle.

Let $G_\omega(\mathbf{r}, \mathbf{r}_1)$ and $G_\omega(\mathbf{r}, \mathbf{r}_2)$ be two pressure Green's functions satisfying the differential equations

$$\rho(\mathbf{r})\nabla\cdot\left[\rho^{-1}(\mathbf{r})\,\nabla G_\omega(\mathbf{r}, \mathbf{r}_1)\right] + k^2\, G_\omega(\mathbf{r}, \mathbf{r}_1) = -\delta(\mathbf{r}-\mathbf{r}_1), \tag{2.269}$$

$$\rho(\mathbf{r})\nabla\cdot\left[\rho^{-1}(\mathbf{r})\,\nabla G_\omega(\mathbf{r}, \mathbf{r}_2)\right] + k^2\, G_\omega(\mathbf{r}, \mathbf{r}_2) = -\delta(\mathbf{r}-\mathbf{r}_2). \tag{2.270}$$

Now, multiplying the first equation by $G_\omega(\mathbf{r}, \mathbf{r}_2)$ and the second by $G_\omega(\mathbf{r}, \mathbf{r}_1)$, and subtraction of the two, followed by integration over a volume V', yield

$$\begin{aligned}\frac{G_\omega(\mathbf{r}_1, \mathbf{r}_2)}{\rho(\mathbf{r}_1)} - \frac{G_\omega(\mathbf{r}_2, \mathbf{r}_1)}{\rho(\mathbf{r}_2)} = \int_{V'} \Big\{ & G_\omega(\mathbf{r}', \mathbf{r}_2)\,\nabla\cdot\left[\rho^{-1}(\mathbf{r}')\,\nabla G_\omega(\mathbf{r}', \mathbf{r}_1)\right] \\ & - G_\omega(\mathbf{r}', \mathbf{r}_1)\,\nabla\cdot\left[\rho^{-1}(\mathbf{r}')\,\nabla G_\omega(\mathbf{r}', \mathbf{r}_2)\right]\Big\}\,\mathrm{d}V'. \end{aligned} \tag{2.271}$$

Using integration by parts in the form of *Green's identity*,

$$\int_{\mathrm{V}} g\,\nabla\cdot\mathbf{f}\,\mathrm{d}V = -\int_{\mathrm{V}} (\nabla g)\cdot\mathbf{f}\,\mathrm{d}V + \oint_{\mathrm{S}} g\,\mathbf{f}\cdot\mathbf{n}\,\mathrm{d}S \tag{2.272}$$

with $\mathbf{f} = \rho^{-1}\nabla G_\omega$, we change the volume integral to a surface integral over the surface S' of the volume V',

$$\frac{G_\omega(\mathbf{r}_1,\mathbf{r}_2)}{\rho(\mathbf{r}_1)} - \frac{G_\omega(\mathbf{r}_2,\mathbf{r}_1)}{\rho(\mathbf{r}_2)} = \int_{S'} \left[G_\omega(\mathbf{r}',\mathbf{r}_2)\,\rho^{-1}(\mathbf{r}')\,\frac{\partial G_\omega(\mathbf{r}',\mathbf{r}_1)}{\partial \mathbf{n}} - G_\omega(\mathbf{r}',\mathbf{r}_1)\,\rho^{-1}(\mathbf{r}')\,\frac{\partial G_\omega(\mathbf{r}',\mathbf{r}_2)}{\partial \mathbf{n}} \right] \mathrm{d}S'. \tag{2.273}$$

Now it is clear that the Green's function satisfies the *reciprocity relation*

$$\rho(\mathbf{r}_2)\,G_\omega(\mathbf{r}_1,\mathbf{r}_2) = \rho(\mathbf{r}_1)\,G_\omega(\mathbf{r}_2,\mathbf{r}_1), \tag{2.274}$$

if there exists a boundary S' where G_ω satisfies boundary conditions of the form

$$\frac{\partial G_\omega(\mathbf{r}',\mathbf{r})}{\partial \mathbf{n}} - \eta(\mathbf{r}')G_\omega(\mathbf{r}',\mathbf{r}) = 0, \tag{2.275}$$

where $\eta(\mathbf{r}')$ is an arbitrary factor.

Boundary conditions of the form given in (2.275) are called *natural boundary conditions* and include as special cases both the *Dirichlet* boundary condition ($\eta(\mathbf{r}') = \infty$) and the *Neumann* boundary condition ($\eta(\mathbf{r}') = 0$). As shown in Sect. 2.3.3, the *radiation condition* in infinite media can also be expressed in this form. Other boundary conditions covered by (2.275) are *impedance conditions* with prescribed ratio between pressure and normal particle velocity.

Equation (2.275) is clearly a sufficient condition for reciprocity, but not a necessary one. However, all physically realistic environmental models will have natural boundary or radiation conditions. Thus, for example, the Pekeris waveguide has a Dirichlet boundary condition at the free surface, and radiation conditions at $(r, z) \to \infty$. On the other hand, the boundary conditions do not have to be *natural* on any surface S'. Thus in the Pekeris waveguide the boundary conditions at the seabed cannot be written in the form given in (2.275). The reason is that (2.275) represents only *local* boundary conditions, whereas the boundary conditions at the Pekeris waveguide seabed are *non-local*, involving the field propagating to a point on the boundary from everywhere else on the same boundary. However, the surface integral will still vanish along the seabed. This is easily verified by inserting the wavenumber integral representation for the Green's functions into the surface integral, interchanging the order of integration, and reformulating the boundary conditions for the *depth-dependent Green's function* at the seabed to an impedance condition using the radiation condition in the lower halfspace.

We will see in Chap. 7 that the natural boundary conditions play an important role in formulating the finite-element solution to the wave equation.

Problems

2.1. Sound propagating in a moving medium is governed by a so-called *convected wave equation*. Consider the case where the background flow velocity is uniform in the x-direction with velocity V.

a. Following the procedure in Sect. 2.1, derive the convected wave equation for sound in a one-dimensional environment with flow velocity V:

$$\left(1 - \frac{V^2}{c^2}\right) p_{xx} - \frac{2V}{c^2} p_{xt} - \frac{1}{c^2} p_{tt} = 0.$$

Note that setting $V = 0$ gives the usual wave equation.

b. Show that this equation can also be derived from the standard wave equation by changing to a moving coordinate system $(\xi, \tau) = (x + Vt, t)$.

c. What is the form of this equation in three dimensions?

2.2. Assume an acoustic source is designed as a small, spherical balloon of radius a, within which the pressure is oscillating with frequency f, with maximum pressure amplitude P.

a. Derive the expression for the acoustic pressure vs range.

b. Determine the expression for P which directly yields transmission loss, i.e., unit pressure at $r = 1$ m.

2.3. Derive *Green's theorem* for a fluid medium with variable density, where the wave equation is of the form given in (2.14).

2.4. Make a computer code for computing the magnitude and phase of the plane-wave reflection coefficient at an interface separating two fluid halfspaces.

a. As a test of your code reproduce the results of Figs. 2.10 and 2.11.

b. Discuss in physical terms the grazing angle dependence of the results.

c. Add a second fluid layer in the bottom and then add frequency as an independent variable to your computer program. Contour your reflection results as a function of angle and frequency. Discuss the resulting structure of the contoured output.

2.5. For an ideal waveguide bounded above by a pressure-release surface and below by an infinitely rigid wall, derive a ray expansion for the acoustic field.

2.6. Write a code evaluating the ray expansion in (2.138) for the pressure field in an ideal waveguide with pressure-release boundaries.

a. For a 100-m deep waveguide, compute the transmission loss for both source and receiver at depth 36 m, at every 100 m range out to 2 km. Compare your results to Fig. 2.23b.

b. Perform a convergence analysis for a few selected ranges and discuss the range dependence.

2.7. Show that (5.299) represents the sum of the residues of the wavenumber kernel in (2.146).

2.8. Consider an isovelocity waveguide of thickness D, bounded above and below by infinitely rigid walls.

a. Derive the characteristic equation for the horizontal wavenumber of the normal modes.
b. Sketch the vertical pressure distribution of the first few normal modes.
c. Derive the dispersion relation for the normal modes. Discuss the differences compared to the waveguide with pressure release boundaries.

2.9. Consider an environment similar to the Pekeris waveguide in Fig. 2.25, but with the bottom speed being changed to $c_2 = 1300\,\text{m/s}$.

a. Make a sketch of the complex wavenumber plane for this problem (similar to Fig. 2.26), indicating the integration contour and the EJP branch cuts.
b. Discuss the existence of normal modes in this case. If they exist, show their approximate positions.
c. Make a sketch of the branch cuts corresponding to the vertical wavenumber being purely imaginary, with the corresponding closed integration contour.

2.10. Consider a Pekeris waveguide with the speed of sound $c_1 = 1500\,\text{m/s}$ and density $\rho_1 = 1000\,\text{kg/m}^3$ in the water column, and with $c_2 = 1800\,\text{m/s}$ and $\rho_2 = 2000\,\text{kg/m}^3$ in the bottom. The water depth is 100 m. A line source at depth z_s is generating a plane acoustic field in the waveguide.

a. Defining the slowness of the mth normal mode as

$$p_m = \frac{k_{xm}}{\omega},$$

where k_{xm} is the horizontal wavenumber of the mode, state the upper and lower limit of p_m for modes propagating in the positive x-direction.
b. For a source frequency exciting 3 modes, make a sketch of the mode functions for pressure and for the particle velocity potential. Discuss the differences.
c. Derive the expression for the vertical wavelength of the modes.
d. Using the results from questions (a) and (c), state the lower limit for the vertical wavelength of a mode at angular frequency ω.
e. Use the result from (d) to determine how many modes you have at frequency $f = 30\,\text{Hz}$.

2.11. In (2.189), $a_m(k_{rm})$ represents a waveguide-specific modal excitation function.

a. Derive the expression for $a_m(k_{rm})$ for the Pekeris waveguide.
b. Show that the modal excitation function has its maximum at the Airy phase frequency, i.e., the frequency where the mode has its minimum group velocity.

c. Compute and plot vs frequency the magnitude of the excitation function for the first 3 modes in the Pekeris waveguide in Fig. 2.25. Discuss the results.

2.12. A storm has created a 1 m thick surface layer with a uniform distribution of small air bubbles. The fraction of the volume occupied by the bubbles is 10^{-3}.

a. What assumption(s) do you have to make to treat the bubble layer as a homogeneous acoustic medium?
b. Under these assumptions, find the numerical values of the sound speed c and density ρ of the bubble layer. The sound speed of water and air are $c_w = 1500\,\text{m/s}$ and $c_a = 340\,\text{m/s}$, respectively, and the corresponding densities are $\rho_w = 1000\,\text{kg/m}^3$ and $\rho_a = 1.2\,\text{kg/m}^3$.
c. Show that the characteristic equation for normal modes in the bubble layer is

$$\cot(k_z h) = -\frac{\alpha_w}{k_z}\frac{\rho}{\rho_w},$$

where h is the thickness of the bubble layer, and

$$\alpha_w = \sqrt{k_r^2 - \left(\frac{\omega}{c_w}\right)^2},$$

$$k_z = \sqrt{\left(\frac{\omega}{c}\right)^2 - k_r^2}.$$

d. Discuss the physical significance of α_w and k_z.
e. What is the value of the cutoff frequency below which no normal modes can exist in the bubble layer?

2.13. In seismics, volume attenuation is often expressed in terms of the *quality factor*, defined as the ratio between the real and the imaginary part of the bulk modulus, i.e., $Q = K'/K''$ for $K = K' - iK''$. For small attenuations, ($Q \gg 1$), derive the relation between Q and the loss tangent δ, and the loss factor α in dB per wavelength.

2.14. Consider the reflection of plane waves from a bottom with the sound speed profile

$$c(z) = \begin{cases} (az+b)^{-1}, & 0 < z < 100\,\text{m}, \\ 1600\,\text{m/s}, & z \geq 100\,\text{m}. \end{cases}$$

The sound speed is continuous at the seabed ($z = 0$) and at $z = 100\,\text{m}$, and the speed of sound in the water column ($z < 0$) is 1500 m/s.

a. Determine the constants a and b.
b. What is the critical grazing angle for waves incident from the water column?

c. Use the WKB approximation to derive expressions for the magnitude and phase of the reflection coefficient. Derive the result for grazing angles smaller and larger than critical. *Hint:*

$$\int \sqrt{\alpha + \beta x^2}\mathrm{d}x = \frac{1}{2}\left[x\sqrt{\alpha + \beta x^2} + \frac{\alpha}{\sqrt{\beta}}\log\left(x\sqrt{\beta} + \sqrt{\alpha + \beta x^2}\right)\right].$$

d. For a frequency of 100 Hz, compute the phase of the reflection coefficient at grazing angles of incidence $30°, 40°, 50°, 60°, 70°, 80°$, and make a sketch of the result.

2.15. Using the procedure to derive generalized invariants, derive the corresponding invariant quantities in which range can be taken as the independent variable. In particular, show that

$$\gamma_{r:\omega,D,c} = 1, -2, 1.$$

Next, show that the ideal waveguide trajectory of constant-intensity interference maxima along a horizontal array (with elements at r) for a changing sound speed c would be described by

$$\frac{\delta c}{\delta r} = \frac{c}{r}.$$

References

1. P.G. Bergmann, The wave equation in a medium with a variable index of refraction. J. Acoust. Soc. Am. **17**, 329–333 (1946)
2. L.M. Brekhovskikh, O.A. Godin, *Acoustics of Layered Media II* (Springer, Berlin, 1992)
3. C.L. Pekeris, Theory of propagation of explosive sound in shallow water. Geol. Soc. Am. Mem. **27** (1948)
4. W.M. Ewing, W.S. Jardetzky, F. Press, *Elastic Waves in Layered Media* (McGraw-Hill, New York, 1957)
5. C.B. Officer, *Introduction to the Theory of Sound Transmission* (McGraw-Hill, New York, 1958)
6. P.M. Morse, K.U. Ingard, *Theoretical Acoustics* (McGraw-Hill, New York, 1968)
7. I. Tolstoy, C.S. Clay, *Ocean Acoustics: Theory and Experiment in Underwater Sound* (American Institute of Physics, New York, 1987)
8. L.M. Brekhovskikh, O.A. Godin, *Acoustics of Layered Media I* (Springer, Berlin, 1990)
9. G.V. Frisk, *Ocean and Seabed Acoustics: A Theory of Wave Propagation* (Prentice-Hall, Englewood Cliffs, NJ, 1994)
10. W. Munk, P. Worcester, C. Wunsch, *Ocean Acoustic Tomography* (Cambridge University Press, New York, 1995)
11. H. Medwin, C.S. Clay, *Fundamentals of Acoustical Oceanography* (Academic Press, San Diego, 1997)
12. P.M. Morse, H. Feshbach, *Methods of Mathematical Physics, Part I* (McGraw-Hill, New York, 1953)
13. J. Miklowitz, *The Theory of Elastic Waves and Waveguides* (North-Holland, New York, 1984)
14. J.W.S. Rayleigh, *The Theory of Sound, Vol. I* (Dover, New York, 1945)
15. S.D. Chuprov, Interference structure of a sound field in a layered ocean. in *Ocean Acoustics, Current State*, ed. by L.M. Brekhovskikh, I.B. Andreevoi (Nauka, Moscow, 1982), pp. 71–91

16. L.M. Brekhovskikh, Yu. Lysanov, *Fundamentals of Ocean Acoustics*, 3rd edn. (Springer, Berlin, 2003)
17. D.E. Weston, A.A. Horrigan, S.J.L. Thomas, R. Revie, Studies in sound transmission fluctuations in shallow water. Philos. Trans. R. Soc. London, Ser. A (1969)
18. G.A. Grachev, Theory of acoustic field invariants in layered waveguides. Acoust. Phys. **39**, 67–71 (1993)
19. W.A. Kuperman, G.L. D'Spain (eds.), *Ocean Acoustic Interference Phenomena and Signal Processing* (AIP, New York, 2002).
20. F.R. DiNapoli, R.L. Deavenport, Theoretical and numerical Green's function solution in a plane layered medium. J. Acoust. Soc. Am. **67**, 92–105 (1980)
21. M. Abramowitz, I.A. Stegun, *Handbook of Mathematical Functions* (Dover, New York, 1965)

http://www.springer.com/978-1-4419-8677-1

Computational Ocean Acoustics

Jensen, F.B.; Kuperman, W.A.; Porter, M.B.; Schmidt, H.

2011, XVIII, 794 p., Hardcover
ISBN: 978-1-4419-8677-1